Optical and Infrared Masers

16th Semi-Annual Status Report

for period

October 1, 1970 to March 31, 1971

to

National Aeronautics and Space Administration

Washington, D. C. 20546

NASA Research Grant NGL 22-009-012

M.I.T. Project DSR 76148

from

Department of Physics

MASSACHUSETTS INSTITUTE OF TECHNOLOGY

Cambridge, Massachusetts 02139

Issue Date: May 21, 1971

Optical and Infrared Masers

16th Semi-Annual Status Report

for period

October 1, 1970 to March 31, 1971

to

National Aeronautics and Space Administration

Washington, D. C. 20546

NASA Research Grant NGL 22-009-012

M.I.T. Project DSR 76148

from

Department of Physics

MASSACHUSETTS INSTITUTE OF TECHNOLOGY

Cambridge, Massachusetts 02139

Issue Date: May 21, 1971

Table of Contents

Introduction and Summary

This report summarizes progress for the period of October 1, 1970 to March 31, 1971 performed under NASA Grant NGL 22-009-012, "Optical and Infrared Masers". Seven topics are summarized in the areas of high resolution studies of atoms and molecules, molecular excitation and relaxation mechanisms, short pulse experiments, and laser harmonic frequency mixing. Four appendices containing more detailed discussions are also included.

I. Application of Laser Induced Line Narrowing Techniques to Measurement of Hyperfine Structure of Ne^{21}.

The laser-induced line narrowing technique has been used to measure hyperfine structure in Ne^{21}. This technique, which utilizes laser-induced changes in the atomic state velocity distribution, permits the resolution of structure which is normally obscured by Doppler broadening. Measurements of the narrowed spectral lines have yielded values for the isotope shifts of Ne^{20}, Ne^{21}, and Ne^{22} at 1.15μ and 6096Å and hyperfine constants of Ne^{21}, which lead to an accurate value of the Ne^{21} quadrupole moment. These measurements are described in detail in Appendix A.

II. Excitation and Relaxation Mechanisms in the HF Laser

Molecular Relaxation Studies in HF Gas

Work has begun on assembling the necessary experimental apparatus for investigating vibrational and rotational relaxation processes occurring in pure, gaseous HF and in mixtures of HF and other non-reactive gases. At present, a high vacuum, HF handling system has been designed and assembled. The system is constructed entirely of Kel-F and Teflon plastics. These materials are inert to chemical attack by HF, and, therefore, the formation of impurities via chemical reaction is prevented. The system includes two cold traps for use in further purifying HF by successive distillation. Purity of the condensed sample can be ascertained by electrical conductivity measurements. Finally, a capacitance manometer, for precision pressure measurements was designed and fabricated. The manometer design is similar to that of a standard capacitance manometer, except that only non-reactive teflon materials were used for the interior of the sensing head.

Near Infrared HF Laser

A systematic investigation of the high energy, high gain pulsed HF laser is in progress. Initial experiments with a transverse discharge (TEA) HF, DF laser are described in a paper published in Applied Physics Letters and included as Appendix B of this report. Briefly, the laser is capable of high power, high energy (> 50 m.j.) pulsed output in the attractive 3 and 4μ regions.

The laser device is simple and compact, and utilizes relatively nontoxic gases. However, its spatially non-uniform excitation scheme and its high gain make single transverse mode operation difficult. To overcome these difficulties a short narrow bore, high pressure, longitudinal discharge laser has been designed and operated. It is capable of pulse energies of several milli joules and peak powers of > 2kW. Preliminary experiments indicate its single mode behavior is superior to that of the transverse discharge laser. A comparison of the spectral characteristic of the two lasers is now in progress.

Long Wavelength HF Laser

A wide bore, longitudinal discharge HF laser, to be used in studying far infrared emission in HF, has been built and operated. Laser excitation is accomplished by electrically pulsing a flowing mixture of H_2 and a fluorinated gas species such as SF_6, Freon 14, or Freon 13. The device design is such that a wide range of laser operating conditions and gas mixtures can be investigated. In studying the laser output spectrum, a fore-prism-grating spectrograph combination has been found to be a convenient method of isolating near and far infrared laser lines.

Using this apparatus, we have observed intense, pure rotational lasing in all three of the above named fluorinated gases. Laser wavelength ranged from 9 to 15 μ; corresponding to rotational transitions from J=17 to J=30. Many of these laser wavelengths fall within the well-known 8 to 14 μ atmospheric window. Studies of the

variation in laser spectral properties with gas pressure and gas mixtures have begun. Initial results have already provided clues to the process leading to rotational population inversion.

III. Coherent Effects in Short Pulse Propagation

The study of fluorescence induced by short pulses of radiation in CO_2 has been concluded and the results submitted for publication (see Appendix C). It has been demonstrated that one can observe the coherent excitation of an optical level in this way, even in a very weakly absorbing transition, and extract values of the matrix element and relaxation times.

Present efforts in the area of short pulse propagation and coherent interaction have shifted to an investigation of adiabatic rapid passage.[1] This technique has long been used in magnetic resonance to invert a spin system and study relaxation processes. Previous works in our laboratory on Stark spectroscopy of NH_3 and NH_2D has uncovered a number of transitions which can be swept through resonance with a CO_2 or N_2O laser transition. Because of their large absorption coefficient and tunability, these transitions make excellent candidates for the study of adiabatic rapid passage. These experiments are of interest both from the point of view of studying the propagation of chirped laser pulses through an absorbing or amplifying medium, and for the study of relaxation processes.

The laser and Stark cell are functioning properly and adequate absorption signals have been observed to make an attempt at observation of adiabatic rapid passage feasible in the near future.

---

1. E. B. Treacy, Phys. Letters 27A, 421 (1968).

IV. Extension of Laser Harmonic Frequency Mixing Techniques.

Efforts at frequency measurement in the infrared are currently directed at establishing a high accuracy laser frequency multiplying chain. The objectives are to produce a precise determination of the speed of light, superheterodyne detection at infrared wavelengths, and an accurate frequency measurement of the saturation resonances in CO_2 with possible application as a frequency standard.

Based on the earlier work of Freed and Javan[1], considerable progress has been made (see VI below) in the observation of extremely narrow saturation resonances in CO_2. The sharp resonances show considerable promise as high accuracy frequency standards. The laser frequency multiplier chain will be used for high accuracy frequency measurements of those resonances.

A major obstacle to highly accurate frequency measurement with laser chains has been the difficulty of comparing several drifting laser frequencies to an absolute frequency standard. In 1968, Hocker, Small and Javan[2] demonstrated in a point contact mixer that microwave frequency sidebands may be added to a laser carrier frequency and that drift in the laser may be offset by electronically tuning the microwave source. Work is now proceeding toward construction of a laser frequency chain of electronically stabilized sidebands which can be frequency locked to a frequency standard of absolute calibration.

---

[1] C. Freed & A. Javan, App. Phys. Letts. 17, 53 (1970).
[2] Quarterly Progress Report, January 22, 1969.

Figure I shows the method of producing a 9.3μ stable frequency source which is phase-locked to a conventional frequency standard. A V-band microwave klystron, K_1, is phase-locked to the frequency standard through a commercially available frequency multiplier chain and phase-locked feedback loop, indicated as a lock box. The 12th harmonic of the klystron is produced in the point contact mixer and serves as a stable reference frequency close to the HCN laser frequency.

The HCN laser frequency and a second klystron, K_2, of any convenient frequency are also applied to the mixer resulting in the laser frequency plus and minus a sideband. The difference frequency between one of the sidebands and the stable reference is applied to a second lock box which electronically tunes K_2. At this point, K_2 exactly compensates for any drift in the laser, producing a stable sideband offset from the stable reference, but phase-locked to the frequency standard. The HCN laser and K_2 outputs are then applied to the next mixer and their 12th harmonics are used as a stable reference falling near the 28μ H_2O laser frequency.

In a similar manner, a chain of stable sidebands may be constructed extending to near optical frequencies. The upper frequency limit to such a chain is given by the frequency response of the mixer elements. Previous work of Sokoloff, Sanchez, Osgood and Javan[3] has demonstrated the response of the point

---

[3] D. Sokoloff, A. Sanchez, R. Osgood & A. Javan

contact diode mixers down to wavelengths near 5μ, which overlaps the response range of optical mixers employing bulk nonlinearities in solids.

Progress to date has seen the reconstruction of the HCN and H_2O lasers in order to improve their power output and stability. Current effort is proceeding toward optimizing the 9.3μ and 28μ mixing. In the next several months, a Cesium beam atomic frequency standard is expected to arrive on loan from the Electronic Components Laboratory of the United States Army, Electronics Command. The laser chain will be frequency locked to the Cesium standard.

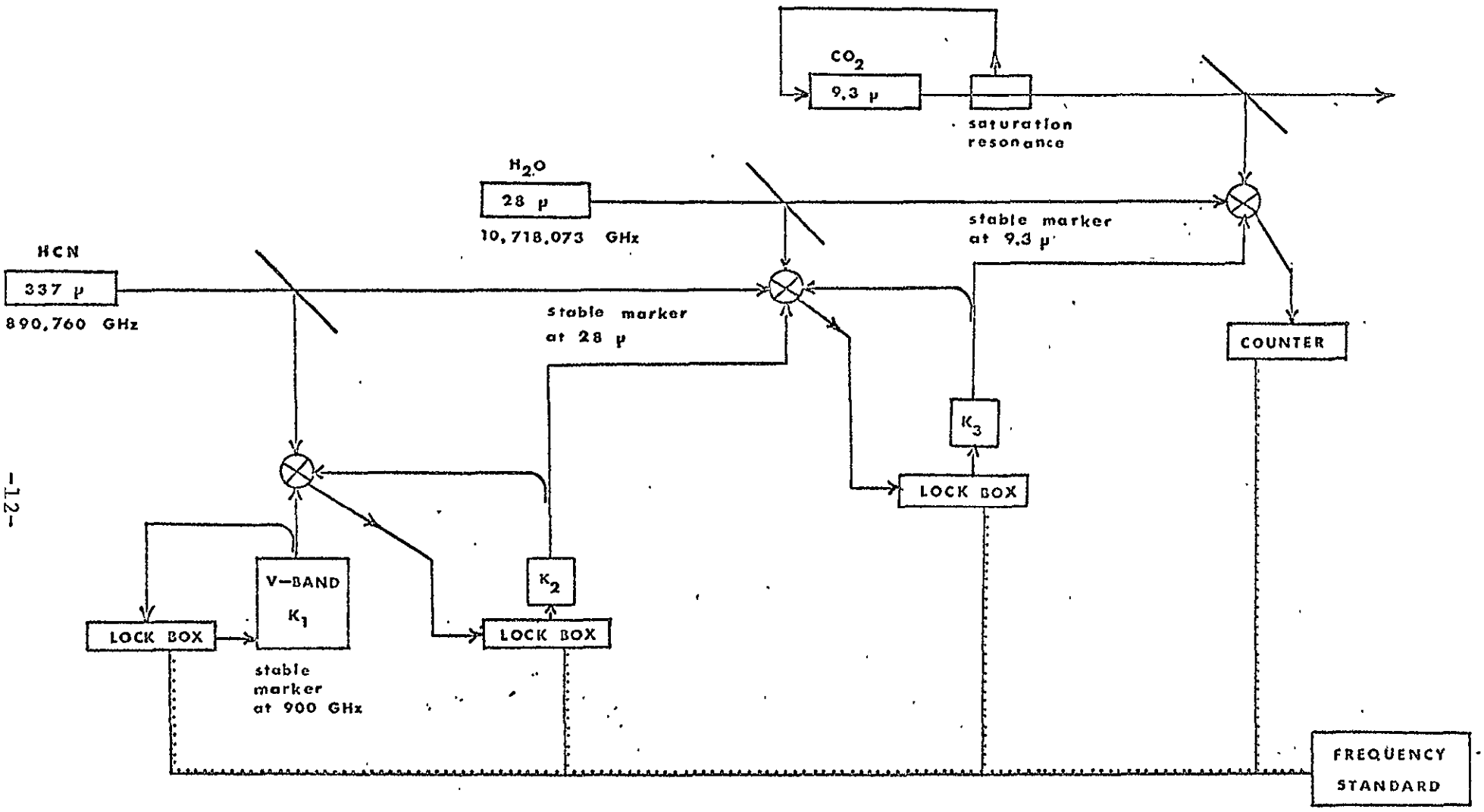

Figure 1. Block diagram of a phase locked laser frequency multiplier chain.

V. Unidirectional Laser Amplifier with a Built-in Isolator

As described in the last progress report, an attempt is being made to utilize the laser-induced line narrowing effect[1,2] to produce a unidirectional laser amplifier in a ring laser configuration. This laser would have the unique property of attenuating any feedback signal which was sent back into it, thereby providing isolation from its surroundings.

The N_2O pumping laser has been optimized to give more than 6 W of output. The laser stability has been checked and found to be satisfactory by looking at the inverted Lamb dip in NH_3, and measurements of absorption and saturation in NH_3 have been carried out. Detailed calculations of the gain in NH_3 and other systems are underway to determine the most suitable substance and operating conditions. A paper describing the operating principles of this device is in preparation.

VI. Molecular Studies Using Standing Wave Saturation Resonances

The study of the standing-wave saturation resonance in low pressure CO_2 is well underway. The effect, first observed by Freed and Javan,[1] is being studied in detail to determine the influence of collisions and intense laser fields on the detailed line shape. In the experiments being performed, the low pressure CO_2 absorption cell is placed outside the laser cavity and the CO_2 laser, which is spaced with 4 invar rods for rigidity and thermal stability, is mounted firmly on a half-ton steel rail to minimize vibration. To further minimize laser jitter we have found it necessary to run the laser under very slow flow conditions. This has been done without the loss of laser intensity as would have been the case with a sealed off laser. Data is being taken on several of the CO_2 laser lines to determine the pressure shifts and saturation parameters of each transition. The signal to noise obtainable by this technique for locking a laser to this narrow resonance is demonstrated in Figure 2.

---

1. C. Freed and A. Javan, Appl. Phys. Letters 17, 53 (1970).

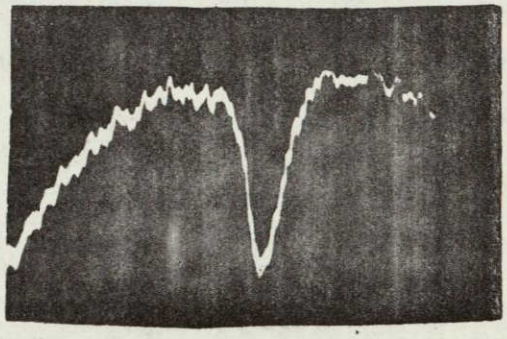

Fig. 2

Standing wave saturation resonance in CO_2 gas. Full width of resonance is ~ 1 MHz.

VII. Standing Wave Features of Laser Induced Line Narrowing Effects

A theoretical investigation has been carried out of the effect of an intense standing wave laser field on a coupled transition when the laser is tuned to the center of its atomic gain profile. The calculations predict a fine structure in the response of the coupled transition which should have important applications in high resolution spectroscopy and laser frequency stabilization. This work has been submitted for publication and is included as Appendix D.

APPENDIX A

HYPERFINE STRUCTURE OF EXCITED STATES AND QUADRUPOLE MOMENT OF Ne^{21} USING LASER INDUCED LINE NARROWING TECHNIQUES*

T. W. Ducas, M. S. Feld, L. W. Ryan, Jr., N. Skribanowitz and A. Javan

INTRODUCTION

Laser Induced Line Narrowing Spectroscopy[1] has been used to observe optical hyperfine structure in Ne^{21}. This technique represents an advance in several ways over other methods of investigating hyperfine and other closely-spaced structure in Doppler broadened systems. The best conventional optical spectrometers, even if not instrument-limited in resolution, are unable to resolve hyperfine transitions whose structure is buried within the Doppler profile. Atomic beam studies in rare gases eliminate the Doppler effect, but have been generally limited to metastable levels, the only states with hyperfine structure that have lifetimes sufficiently long for beam techniques. Furthermore, ordinary beam techniques are incapable of measuring isotope shifts.

In the present approach, an optical technique[2-5] is used in which the Doppler width is effectively eliminated by laser-induced velocity selection. Measurements of the narrowed spectral lines have yielded values for the isotope shifts of $Ne^{20,21,22}$ at 1.15μ and 6096Å, and hyperfine constants of Ne^{21}, which lead to an accurate value for the Ne^{21} quadrupole moment.

The level scheme under study (Fig. 1) consists of the hyperfine sublevels of the $2s_2$, $2p_4$, and $1s_4$ fine structure levels[6] of Ne^{21} (nuclear spin I = 3/2), which form the 1.15μ ($2s_2$ - $2p_4$) and 6096Å ($2p_4$ - $1s_4$) cascade transitions. The magnetic dipole and electric quadrupole hyperfine interactions split each fine structure level (angular momentum J) into a number of hyperfine components, of energy

$$W_F = W_J + A\frac{K}{2} + B\,\frac{3/4K(K+1) - I(I+1)J(J+1)}{2I(2I-1)J(2J-1)}\,, \qquad (1)$$

where $K = F(F+1) - I(I+1) - J(J+1)$

and F, the total angular momentum, can take on the values:

$F = I+J, I+J-1, \ldots, |I-J|$.

W_F is the total energy of the h.f. level, W_J is the energy of the fine structure level; A and B are the magnetic dipole and electric quadrupole interaction constants of level J, respectively.

LASER INDUCED LINE NARROWING EFFECT

A comprehensive treatment of the laser induced line narrowing effect is given in Ref. 1. The following simplified discussion will provide a sufficient background for an understanding of the present experiment. Let us consider a particular coupled three-level system in Ne^{21} consisting of a pair of hyperfine transitions, one at 6096Å and one at 1.15μ, which share a common level. If a 1.15μ traveling-wave laser field is incident upon a sample of Ne^{21}, the atoms over a narrow velocity range which are Doppler shifted into resonance with the applied field couple most strongly to it. This causes selective changes in the level populations over the narrow velocity range. These

changes have a Lorentzian lineshape centered about $v_z = (\Omega_L - \dot{\omega}_2/K_2)$ and the velocity range is $\Delta v_z \sim \gamma/K_2$ where Ω_L is the frequency of the 1.15μ hyperfine transition, k_2 the corresponding propagation constant and γ is the homogeneous linewidth of the laser transition.

This change in the velocity distribution manifests itself in a change of intensity with a Lorentzian lineshape (change signal) in the coupled 6096Å fluorescence over a narrow section of the Doppler profile emitted along the axis of propagation of the laser field. The peak of this spontaneous emission signal in the forward direction (i.e. parallel to the propagation vector of the laser field $\vec{k}_L$) occurs at $\Omega_F = \omega_1 + k_1 v_z$, and the backward (anti-parallel) change signal occurs at $\Omega_B = \omega_1 - k_1 v_z$; where ω_1 is the atomic center frequency of the coupled 6096Å transition.[7]

The locations of these change signals can be rewritten simply as:

$$\Omega_F = \omega_1 + [\Omega_L - \omega_2]\frac{\omega_1}{\omega_2} ; \tag{2a}$$

$$\Omega_B = \omega_1 - [\Omega_L - \omega_2]\frac{\omega_1}{\omega_2} . \tag{2b}$$

Thus the separation between change signals due to the pair (j,k) of closely spaced three-level systems is given by:

$$\Omega_F(j) - \Omega_F(k) = [\omega_1(j) - \omega_1(k)] - [\omega_2(j) - \omega_2(k)]\frac{\omega_1}{\omega_2}; \tag{3a}$$

$$\Omega_B(j) - \Omega_B(k) = [\omega_1(j) - \omega_1(k)] + [\omega_2(j) - \omega_2(k)]\frac{\omega_1}{\omega_2}. \tag{3b}$$

The hyperfine interactions in Ne^{21}, which produce 18 such three-

level systems, can be analyzed from Eqs. (3). Note that forward and backward patterns contain information on the h.f.s. of both 1.15μ and 6096Å transitions. Separate observation of forward and backward signals[5] provides two distinct patterns which must be fit by a single set of parameters. These parameters, the hyperfine A and B constants for each of the three levels, can be extracted from the separations between the features of the spectrum. The fact that the relative positions of the change signals are independent of laser tuning [Eq. (3)] greatly simplifies the analysis.

The complete theoretical expression describing the laser induced change signals is given in Table I.

EXPERIMENTAL ARRANGEMENT

The experimental set-up is shown in Fig. 1b. An intense single mode[8,9] 1.15μ He-Ne laser (see below) is locked to the resonance of a stable passive Fabry-Perot interferometer by standard methods. The laser output beam is focused into an external sample cell containing Ne^{21} at a low pressure (~0.1 torr). The 6096Å spontaneous emission from the sample cell, emitted in either the forward or backward[10] direction, is analyzed using a pressure-scanned Fabry-Perot interferometer with a free spectral range of 4090 MHz and a finesse of 40. The entire apparatus is shock-mounted to reduce vibration effects. Linear scanning is achieved with a system of capillary tubes (11) bleeding dry air into a cannister containing the interferometer. A chopper, placed between the laser and the sample cell, enables us to use a lock-in amplifier to subtract off the spontaneous emission background and improve the signal to noise ratio.

In this experiment it is essential to have the laser operate on a single mode, since each extra mode would produce an additional set of change signals. It is also important to maximize the power in this mode since the sizes of the change signals are essentially proportional to the laser field intensity. This is particularly critical in this experiment because the sample cell is outside the laser resonator. Neither short laser cavities nor conventional Michelson mode-selection techniques can satisfy the single mode power requirement. We have employed instead the following arrangement:[8,9]

Within the laser resonator (length 1.6 m) along with the He-Ne amplifier cell (total pressure ~2 torr) we have placed an absorber cell filled with neon at a low pressure (~0.2 torr). The cells are of comparable length and the small signal gain of the amplifier is several times as large as the loss of the absorber. While the linear gain of the system is dominated by the amplifier cell, the absorber, which saturates more readily, contributes appreciably to the saturation behavior. The result is that the system is driven into the strong coupling regime, where the modes compete heavily with one another. Thus, laser oscillation at one mode tends to suppress oscillation at other modes. The net result is a continuously tunable single mode output with an appreciable fraction of the full power of multimode operation. In our experiment we were able to convert over 50% of the multimode power (modes) into a single mode.

HYPERFINE THEORY

The electronic configurations of excited states in neon consist of a 2p hole coupled to an excited electron surrounding closed shells. The wave functions of the resulting fine structure energy levels, obtained from the f.s. energy splittings[12], may be expressed in terms of the admixture of the appropriate LS wave functions[13,14]. The A and B interaction constants which determine the hyperfine spectrum [Eq. (1)] may be obtained from these wave functions, the nuclear dipole moment μ, and the nuclear quadrupole moment Q[15]. The resulting expressions for the A's and B's of the three levels of interest contain the coefficients of the LS wave functions and the parameters: μ; Q; $\frac{1}{r^3}$ for the 2p hole; $\frac{1}{r^3}$ for the 3p electron; and the contact terms A_{3s} and A_{4s} for the 3s and 4s states of the excited electron.

In a previous experiment[16] Grosof, Buck, Lichten and Rabi measured the A and B constants of the $1s_5$ level of Ne^{21} to high (0.1%) accuracy. But since $\frac{1}{r^3}_{\text{2p hole}}$ can only be estimated to 10% accuracy, using the Fermi-Segre formula[15] and their measured value of $A(1s_5)$, their value of Q has this same uncertainty [$B(1s_5) \propto Q_{(2}\frac{1}{r^3}_{\text{2p hole}}$].

We make use of the measured[16] values of $A(1s_5)$ and $B(1s_5)$ and of the known[17] value of μ to reduce the number of parameters in our theoretical description by three: Q is expressed in terms of $B(1s_5)$ and $\frac{1}{r^3}_{\text{2p hole}}$; and A_{3s} may be expressed in terms of $A(1s_5)$ $\frac{1}{r^3}_{\text{2p hole}}$ (independent of the admixture of states for the $1s_5$ level). The remaining parameters are: $\frac{1}{r^3}_{\text{2p hole}}$; $\frac{1}{r^3}_{\text{3p electron}}$; and A_{4s}. The contribution of the 3p electron to the h.f.s. is negligible. Fur-

thermore, the error in our estimate of a_{4s} (from the Fermi-Segre formula) produces only a small uncertainty in $A(2s_2)$. Thus, the h.f. - interaction constants are sensitive only to the $\frac{1}{r^3}_{2p\ hole}$ parameter. In the following paragraphs we expand upon the preceding discussion and describe the particular calculations involved in obtaining expressions for the hyperfine constants.

In our analysis we use the wave functions of Vainshtein and Minaeva[14]:

$$
\begin{aligned}
|2s_2 &= -.660|^3P_1 + .752|^1P_1 , \\
|2p_4 &= .127|^3D_2 - .309|^1D_2 + .943|^3P_2 , \\
|1s_4 &= .964|^3P_1 + .266|^1P_1 ,
\end{aligned}
\tag{4}
$$

Where $^{2s+1}L_J$ are wave functions in the LS representation. These wave functions have been derived from the fine structure energy splittings[12], taking into account electrostatic, spin-orbit, spin-spin and spin-other-orbit interactions.

The LS matrix elements for the magnetic dipole and electric quadrupole interactions for the $p^5 3$ and $p^5 p^1$ configurations are given by Childs[18,19]. We use the non-relativistic limit for these matrix elements since relativistic corrections are negligible (<1% for low Z atoms such as neon) combining these with Eqs. (4) we get the following expressions for the A and B interaction constants for the three levels of concern:

$$
\begin{aligned}
A(2s_2) &= 1.352\ a_{2p\ hole} + .460\ a_{4s}, \\
B(2s_2) &= -.139\ b_{2p\ hole}; \\
A(2p_4) &= ..367\ a_{2p\ hole} + .403\ a_{3p}, \\
B(2p_4) &= .053\ b_{2p\ hole} - .219\ b_{3p};
\end{aligned}
\tag{5}
$$

$$A(1s_4) = .819\ a_{2p\ hole} + .051\ a_{3s},$$
$$B(1s_4) = .158\ b_{2p\ hole};$$

With

$$a_{np} = \frac{2\mu\mu_B}{I} \left\langle \frac{1}{r^3} \right\rangle_{np},$$
$$b_{np} = e^{2Q} \left\langle \frac{1}{r^3} \right\rangle_{np},$$

where μ_B is the Bohr magneton.

Now, if we employ the results of Grosof et al[16] for the $1s_5$ level of Ne^{21}:

$$A(1s_5) = -267.68 \pm .03 MHz$$
$$B(1s_5) = -111.55 \pm .10 MHz$$

and the fact that[18], independent of the LS coefficients of the $1s_5$ wave function:

$$A(1s_5) = 1/4\ a_{3s} + 2/5\ a_{2p\ hole}$$
$$B(1s_5) = -2/5\ b_{2p\ hole}$$

we can express our A and B constants in MHz in the following manner:

$$A(2s_2) = .460\ a_{4s} - 843.27\ R_h,$$
$$B(2s_2) = -38.786;$$

$$A(2p_4) = -228.78 R_h - 251.39 R_e,$$
$$B(2p_4) = 14.898 - 61.191\ R_e/R_h; \qquad (6)$$

$$A(1s_4) = -54.639 - 459.74 R_h,$$
$$B(1s_4)\ 43.940;$$

where

$$\left\langle \frac{1}{r^3} \right\rangle_{2p\ hole} = R_h \times 10^{26}\ cm^{-3},$$

$$\left\langle \frac{1}{r^3} \right\rangle_{3p\ electron} = R_e \times 10^{26}\ cm^{-3}.$$

Equation (6) provides quantitative expressions for the contributions of the different parameters to the A's and B's. Estimates of A_{4s} and R_e can be obtained from the fine structure energy levels using formulae in Kopfermann[15]. The uncertainties in these calculations are of the order of 10%, but the uncertainties they introduce into $A(2s_2)$, $A(2p_4)$ and $B(2p_4)$ are much smaller, on the order of 1%. This is so becuase R_e is less than 1% as large as R_h and, as will be seen below, the A_{4s} term in Eq.(6) contributes less than 10% to $A(2s_2)$.

The preceding discussion indicates that the single dominant influence in determining each hyperfine interaction constant is $\frac{1}{r^3}_{2p\ \text{hole}}$. Because of the sensitivity of our expressions to this parameter, we must provide for its variation with the state of the excited electron. Equations (5) and (6) can be modified in a straightforward way to include such effects. The B of each level is less than 10% of the corresponding A in magnitude, so that small changes in $1/r^3_{2p\ \text{hole}}$ have negligible influence on the h.f.s. through the B's. (This assertion is born out in our computer fits to the data.) But these modifications cannot be ignored in the A's. The A's from Eq. (6) are therefore written:

$$\begin{aligned} A(2s_2) &= .460\, a_{4s} - 843.27R_h\ (2s_2), \\ A(2p_4) &= -228.78R_h\ (2p_4) - 251.39R_e, \\ A(1s_4) &= -54.639 - 459.74R_h(1s_4). \end{aligned} \qquad (7)$$

DATA ANALYSIS AND THEORETICAL FIT

Figure shows typical experimental spectra taken with the Fabry-Perot interferometer, and the computer-generated fit for forward (Fig. 3a) and backward (Fig. 3b) runs. In each case the upper experimental trace shows the narrow change signals, and the lower trace shows the Doppler-broadened background observed without the lock-in amplifier. Note that the hyperfine structure is ordinarily completely masked by the Doppler widths.

The laser frequency, which was carefully monitored, was stable to about 2MHz over the course of a run (about one minute). This figure is considerably smaller than the linewidths of the observed change signals, which are of the order of 250 MHz (including a Fabry-perot width of ∿100 MHz). The largest change signals in Fig. 3 have intensities of about 0.5% of the intensity of the spontaneous emission background. It must be emphasized that the observed spectra are richer than ordinary 6096Å h.f. spectra in that our data contains information about both the laser transition and the coupled spontaneous emission transition. The markings on Fig. 3a denote the eight 3-level systems producing the observed change signals (the contribution of the remaining ten change signals being negligible). The two additional features in the forward and backward traces are due to the presence of Ne^{20} and Ne^{22} in the sample of $Ne^{21(20)}$.

A PDP-12 computer was used to display intensity patterns employing the expressions in Eq. (1) and (2) and in Table I. Trial values for the A's and B's were obtained from Eq. (6), using Fermi-Segre estimates for A_{4s} and $1/r^3_{3p}$ and an optimum value of $1/r^3_{2p\ hole}$. Only small deviations from these trial values were required to find the

hyperfine constants that provided the best fit to the data. These small deviations from the values generated from Eq. (6) can be associated with the theoretical considerations which led to Eq. (7), where a slightly different $1/r^3_{2p\ hole}$ characterizes each A.

The $\alpha(j)$'s and $\beta(j)$'s appearing in the intensity formula (Table I), which determine the relative intensities of the change signals, were calculated from the electric dipolematrix elements[13]. A convenient simplification is that the $\alpha(j)$'s and $\beta(j)$'s are independent of the admixture of the LS wave functions for a particular fine structure energy level (aside from a proportionality constant).

Sixty-six runs were analyzed in all: 41 forward and 25 backward. In analyzing the data we operated under the strict requirement, imposed by the theory of laser induced line narrowing, that the same set of A and B values has to fit both forward and backward experimental traces.

In several experimental runs, the laser frequency was intentionally shifted ∿100MHz. This alters the intensity pattern in prescribed ways (Table I), serving as a further check on our identification of the features.

The best fit to the data (Table II) provides values of : $R_h(1s_4) = .865 \pm .015$; $R_h(2p_4) = .948$; $R_h(2s_2) = .866$. The slightly larger error in the latter value is due to the uncertainty in estimating a_{4s}.

Combining $1/r^3_{2p\ hole}$ for the $1s_4$ level with $B(1s_5)$ from Ref. 18, we obtain an accurate value for the uncorrected nuclear quadrupole moment Q' for the $1s_4$ level of Ne^{21}. This is in good agreement with the value quoted in Ref. 18. Estimates of Q' for the other two levels

would be less accurate since our experiment is not very sensitive to the precise values of the corresponding B's. To establish the actual Q, the Sternheimer correctons would have to be taken into account.

We can also obtain a value for a_{3s}, the Fermi contact interaction constant, from Eq. (5) and our value of $1/r^3_{\text{2p hole}}$ for the $1s_4$ level. Note that this value if 15% smaller in magnitude than that calculated from the Fermi-Segre formula.

Our values of $1/r^3_{\text{2p hole}}$ for the $2s_2$ and $1s_4$ levels, which have the excited electron in an s-state, are within 1% of each other. The corresponding result for the $2p_4$ level is about 10% larger than these. The former two values are in close agreement with the semi-empirical value for the $1s_5$ level from Ref. 18.

It is interesting to compare these values with that for the neon ion ground state, in which the excited electron surrounding the 2p hole is removed. A calculation using restricted Hartree-Fock wave functions[21] gives a value for $1/r^3_{\text{.2p hole}}$ which is within 2% of our results for the $2s_2$ and $1s_4$ levels.

These conclusions are, of course, subject to the approximations made in deriving the A's of Eq. (7) and the B's of Eq. (6). One source of error is the uncertainty in the LS admixture coefficients of our wave functions [Eq. (4)]. These values are expected to be accurate for the $1s_4$ and $2s_2$ levels, but somewhat less certain for the $2p_4$ level. This is primarily due to the difficulties associated with properly including effects from spin-spin and spin-other-orbit interactions[22]. Note that the value of $A(2p_4)$ is particularly sensitive to small deviations in the admixture coefficients, since the $2p_4$ state is $\sim$89% a pure LS state.

The assumption of a single $1/r^3_{2p\ hole}$ characterizing each level ignores core polarization effects[23], which result from the spin-dependent distortion of the $(1s)^2\ (2s)^2$ core by the outer electrons. Taking this effect into account theoretically would necessitate for each level: the use of different values of $1/r^3_{2p\ hole}$ in the magnetic h.f.s. resulting from the orbital and spin moments of the electrons; a separate value of $1/r^3_{2p\ hole}$ associated with the quadrupole interaction; and would also add a small contact term to the expressions for the A's.

It should be possible to explore fully the details of the above considerations by studying the laser induced change signals produced at other transitions branching from the upper and lower levels of the 1.15μ and other neon laser lines.

We have also measured the $Ne^{20,21,22}$ isotope shifts at 1.15μ and 6096Å. Ne^{20} and Ne^{22} were introduced into the sample cell containing Ne^{21} to bring up the intensity of their change signals, thus facilitating their identification and measurement. The shifts for the 1.15μ and 6096Å transitions are extracted from the change signal spectra using Eq. (3) [and Eq. (1) in the case of Ne^{21}], and are summarized in Table III. The $Ne^{20,22}$ results are in excellent agreement with previously measured values[2,24,25]. Note in particular that the 1.15μ transition of Ne^{21} is shifted to a higher frequency than that of Ne^{22}. An analysis of the results is in progress and will be reported later.

CONCLUSION

We have demonstrated the applicability of laser induced line narrowing techniques in observing optical h.f.s. in a system whose features are ordinarily masked by Doppler broadening. These techniques can be applied in principle to measurements of closely-spaced structure of transitions coupled directly or indirectly through radiative cascade to either of the laser levels.

Although the change signals in this experiment are considerably narrower than the Doppler width, for many other systems they may be two or three orders of magnitude narrower still. The limits on the resolution are only determined by the homogeneous width of the lines and the resolution of the detection apparatus.

REFERENCES

(1) M.S. Feld and A. Javan, Phys. Rev. 177, 540 (1969). Other references may be found in this paper.

(2) R.H. Cordover, P. Bonczyk and A. Javan, Phys. Rev. Letters 18, 730 (1967).

(3) W.G. Schweitzer, M.M. Birkey and J.A. White, J. Opt. Sci. Am. 57, 1226 (1967).

(4) H.K. Holt, Phys. Rev. Letters, 20, 410 (1968).

(5) In previous experiments (Refs. 2-4), done within the laser resonator, the forward and backward signals appear together. This standing wave configuration makes the analysis of the complex spectra much more difficult than does a running wave experiment which separates forward and backward spectra.

(6) The Paschen designation of the levels is used. The corresponding configurations are:

$$2s_2 : 2p^5 \ (^2P_{1/2}^{\circ}) \ 4s \ (J=1)$$

$$2p_4 : 2p^5 \ (^2P_{1/2}^{\circ}) \ 3p \ (J=2)$$

$$1s_4 : 2p^5 \ (^2P_{3/2}^{\circ}) \ 3s \ (J=1)$$

For notation, see C.E. Moore, Atomic Energy Levels, National Bureau of Standards Circular No. 467 (U.S. Government Printing Office, Washington, D.C., 1949), Vol. 1.

(7) The linewidth of the change signal (full width at half-maximum) in the forward (backward) direction, is given by:

$$\gamma_{\substack{F \\ B}} = \gamma_1 + \left[\frac{\omega_1}{\omega_2}(\gamma_0+\gamma_2) \pm \gamma_0\right]$$

where γ_1 is the decay rate of level j. See Ref. 1 for details.

(8) P.H. Lee, P.B. Schoefer and W.B. Barker, Appl. Phys. Letters 13, 373 (1968); M.S. Feld, A. Javan and P.H. Lee, Appl. Phys. Letters 13, 424 (1968).

(9) I.M. Beterov and V.P. Chebotaev, Soviet Physics J.E.T.P. Letters 9, 127 (1969) [Ah. Eksp. Teor. Fiz. Pis. Red. 9, 216 (1969)].

(10) In the backward runs the 6096Å fluorescence is taken from the sample cell by means of a mirror placed near the entrance window at 45° (Fig. 1b). The laser beam enters the cell through a small hole in the mirror.

(11) D.H. Rank and J.N. Shearer, J. Opt. Sci. Am. 46, 463 (1956).

(12) The f.s. energy levels were obtained from C.E. Moore (Ref. 6) p. 77.

(13) E.V. Condon and G.H. Shortley, The Theory of Atomic Spectra (Cambridge, London, 1959).

(14) L.A. Bainshtein and L. A. Minaeva, Ah. Priklad, Spektrosk, (U.S.S.R.) 8, 244 (1968).

(15) H. Kopfermann, Nuclear Moments, (Academic Press, New York, 1958).

(16) G.M. Grosof, P. Buck, W. Lichten, and I.I. Rabi, Phys. Rev. Letters 1, 214 (1958).

(17) J.T. Latourrette, W.E. Quinn and N.F. Ramsey, Phys. Rev. 107, 1202 (1957).

(18) W.J. Childs, Phys. Rev. A 2, 316 (1970).

(19) Kopfermann (Ref. 15) gives expressions for sp and pp' magnetic dipole matrix elements, and sp electric quadrupole matrix elements. The latter formula, first given by Casimir [H. Casimir, Teylors Tweede Genootshap 11, 255 (1956)] is inconsistent with the matrix elements in Ref. 16, and appears to be in error. The "12" in the third term on the r.h.s. of Ref. 15, eq. 31.4, should be a "6". We wish to thank W.J. Childs for his helpful comments and for pointing this out.

(20) The isotopic mixture of the Ne^{21} sample used was:

87.9% Ne^{21}; 10.2% Ne^{20}; 1.9% Ne^{22}.

(21) H.F. Schaefer III and R.A. Klemm, Phys. Rev. A 1, 1063 (1970).

(22) Calculations of the LS admixture coefficients based on the f.s. energy splittings, including only spin-orbit and electrostatic interactions, are in excellent (0.1%) agreement with the values quoted in Ref. 14 [Eq.(4)] for the $1s_4$ and $2s_2$ levels. For the $2p_4$ level, there is a difference of $\sim$5% in the coefficient of the dominant $|{}^3P_2$ basis state.

(23) See for example: B.G. Wybourne, Spectroscopic Properties of Rare Earths, (Interscience Publishers), New York 1967.

(24) H. Nagaoka and T. Mishima, Inst. of Phys. and Chem. Research, Tokyo 13, 293 (1930).

(25) A. Szoke and A. Javan, Phys. Rev. Letters 10, 521 (1963).

where $\sum_j$ refers to the sum over all possible cascade transitions of the type $F \to F' \to F''$

$$|\alpha(j)|^2 = |\mu_x(F', M_F'; F'', M_F'')|^2 + |\mu_z(F', M_F'; F'', M_F'')|^2,$$

for observation of both polarizations of the 6096Å radiation together.

$$|\beta(j)|^2 = |\mu_z(F, M_F; F', M_F')|^2;$$

μ's are the hyperfine electric dipole matrix elements and can be obtained from tables in Ref. 13.

Note that the relative magnitudes of the $\alpha(j)$'s and $\beta(j)$'s are independent of the fine structure coupling of the levels.

Ω_1 is the frequency of the spontaneous emission at 6096Å.

Ω_{F_B} are defined in the text

Explicit expressions for the proportionality constants C_1 and C_2 are given in Ref. 1.

The line-widths of the change signals (full width at half-maximum) are:

$$\gamma_{F_B} = \gamma_1 + \left[\frac{\omega_1}{\omega_2}(\gamma_0+\gamma_2) \pm \gamma_0\right]$$

where γ_i is the decay rate of level i. For our case i=0,1,2 correspond to the $2p_4$, $1s_4$ and $2s_2$ levels respectively. See Ref. 1 for details.

TABLE I

Ne^{21} f.s. levels→	$1s_4$	$2p_4$	$2s_2$
Magnetic Dipole h.f. Interaction constant, A (MHz)	-452	-219	-756
Electric Quadrupole h.f. interaction constant, B (MHz)	+ 44	+ 15	- 39
R_h ($1/r^3$ 2p hole in 10^{26} cm^{-3})	.865±.015	.948	.866

Nuclear Quadrupole Moment:

$Q'(1s_4) = .0926 \pm .0016$ b* $\quad Q'(1s_5) = .093 \pm .010$ b**

Fermi Contact term for 3s electron:

$a_{3s} = -207$ MHz * $\quad a_{3s}$ (theoretical) $= -245$ MHz ***

$1/r^3$ 2p hole

$R_h(1s_4) = .865 \pm .015$* $\quad R_h(1s_5) = .86 \pm$

$R_h(Ne^+) = .84$

* Present work
** Ref. 16
*** Fermi-Segre Estimate
Semi-Empirical value derived from Ref. 16
Ref. 21

TABLE II

$\nu(Ne^{22}) - \nu(Ne^{20})$

	Present Work	Ref. 21	Ref. 23	Ref. 24
6096Å	1708	1706±30	1680±	———
1.15μ	261	257±8	———	261±3

$\nu(Ne^{22}) - \nu(Ne^{21})$

	Present Work
6096Å	1010
1.15μ	-186

TABLE III

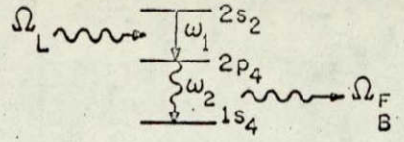

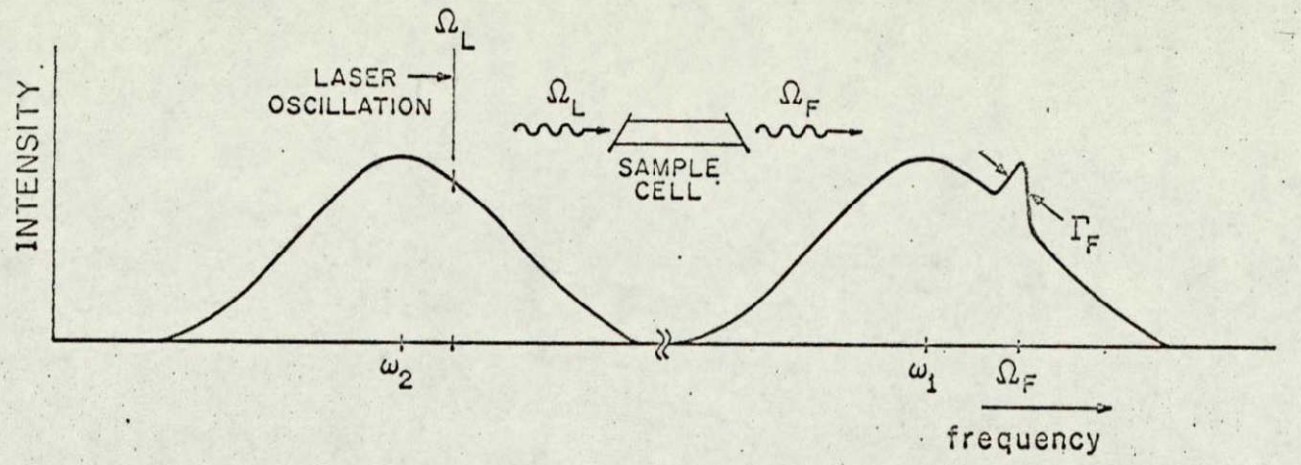

FORWARD CHANGE SIGNAL

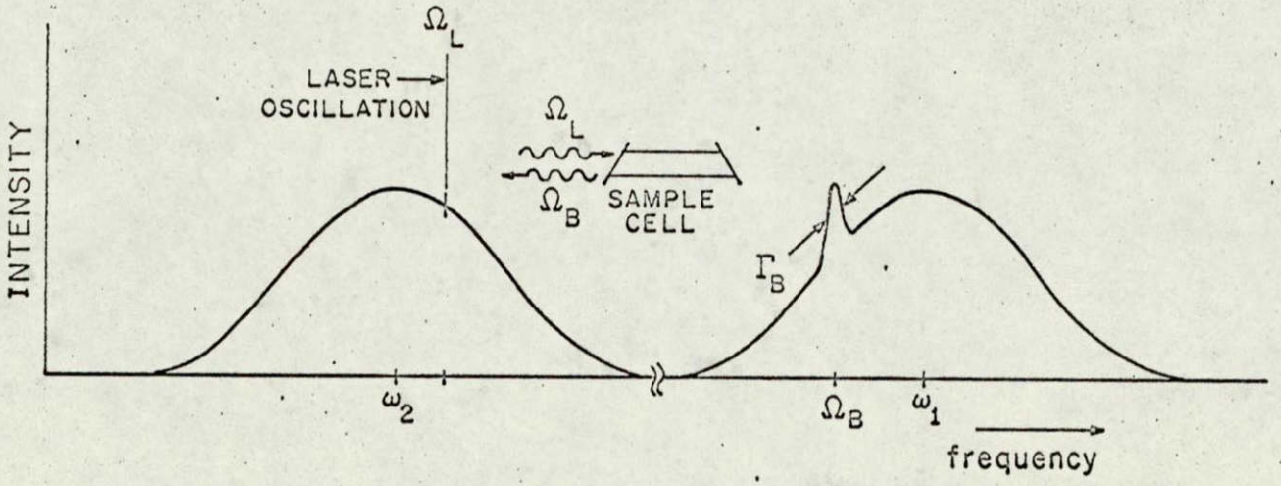

BACKWARD CHANGE SIGNAL

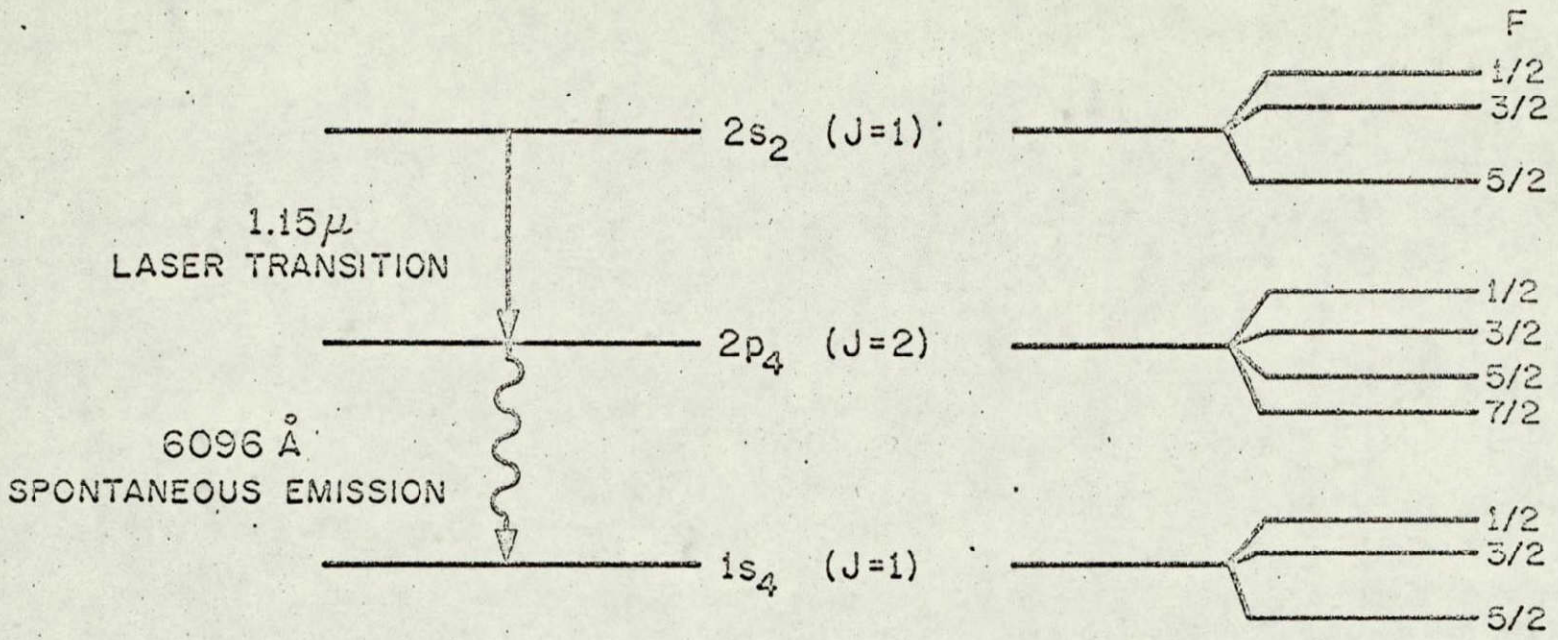

HYPERFINE SPLITTING ENERGIES ARE OF THE FORM:

$$\Delta W_{\substack{\text{Magnetic}\\\text{Dipole}}} = A \cdot \frac{K}{2}$$

$$\Delta W_{\substack{\text{Electric}\\\text{Quadrupole}}} = B \cdot \frac{3/4\, K(K+1) - I(I+1)J(J+1)}{2I(2I-1)J(2J-1)}$$

where $K = F(F+1) - J(J+1) - I(I+1)$

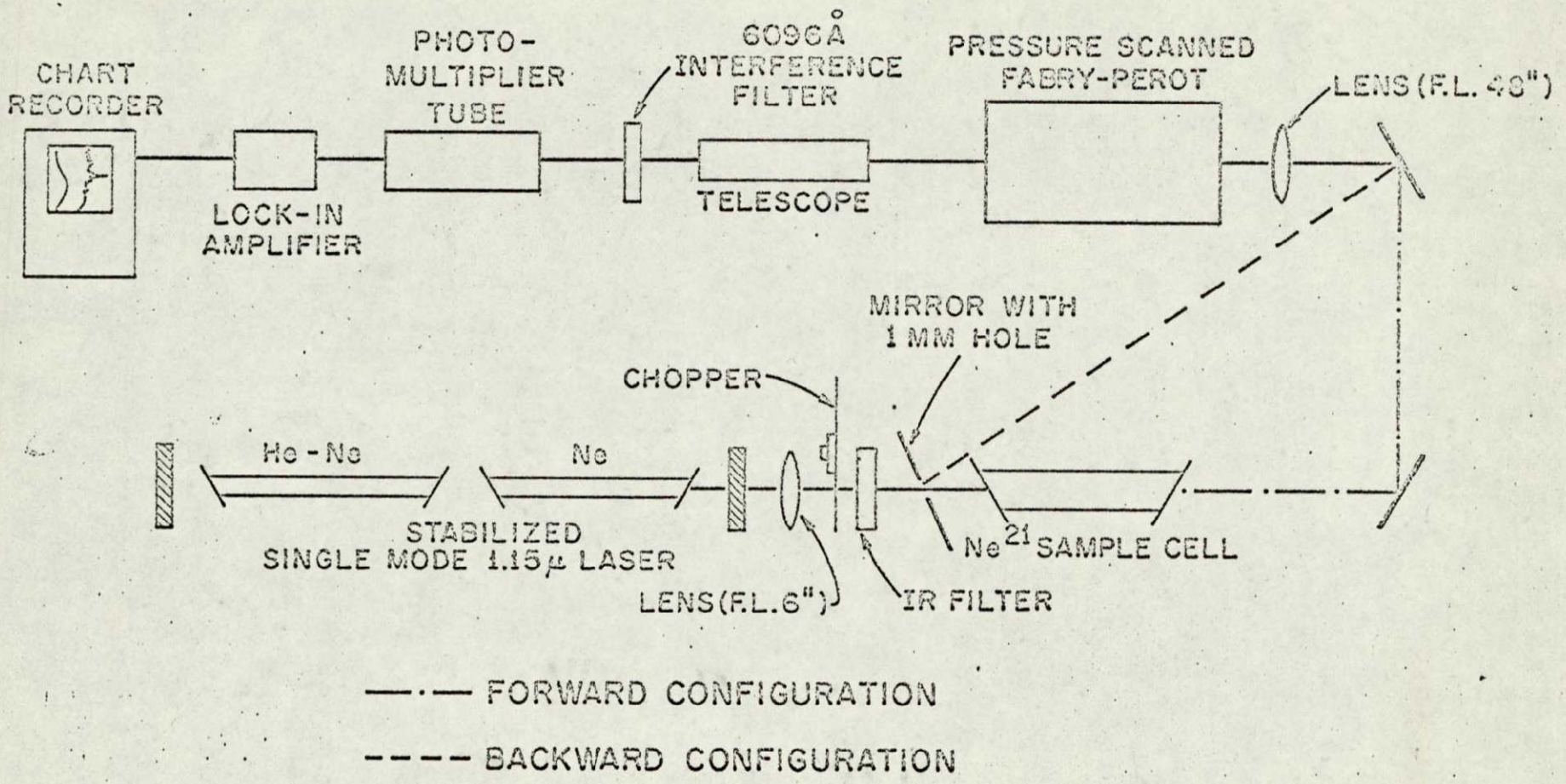
CHART RECORDER
LOCK-IN AMPLIFIER
PHOTO-MULTIPLIER TUBE
6096Å INTERFERENCE FILTER
TELESCOPE
PRESSURE SCANNED FABRY-PEROT
LENS (F.L. 48")
MIRROR WITH 1 MM HOLE
CHOPPER
He - Ne
Ne
STABILIZED SINGLE MODE 1.15μ LASER
LENS (F.L. 6")
IR FILTER
Ne 21 SAMPLE CELL
—·— FORWARD CONFIGURATION
- - - - BACKWARD CONFIGURATION

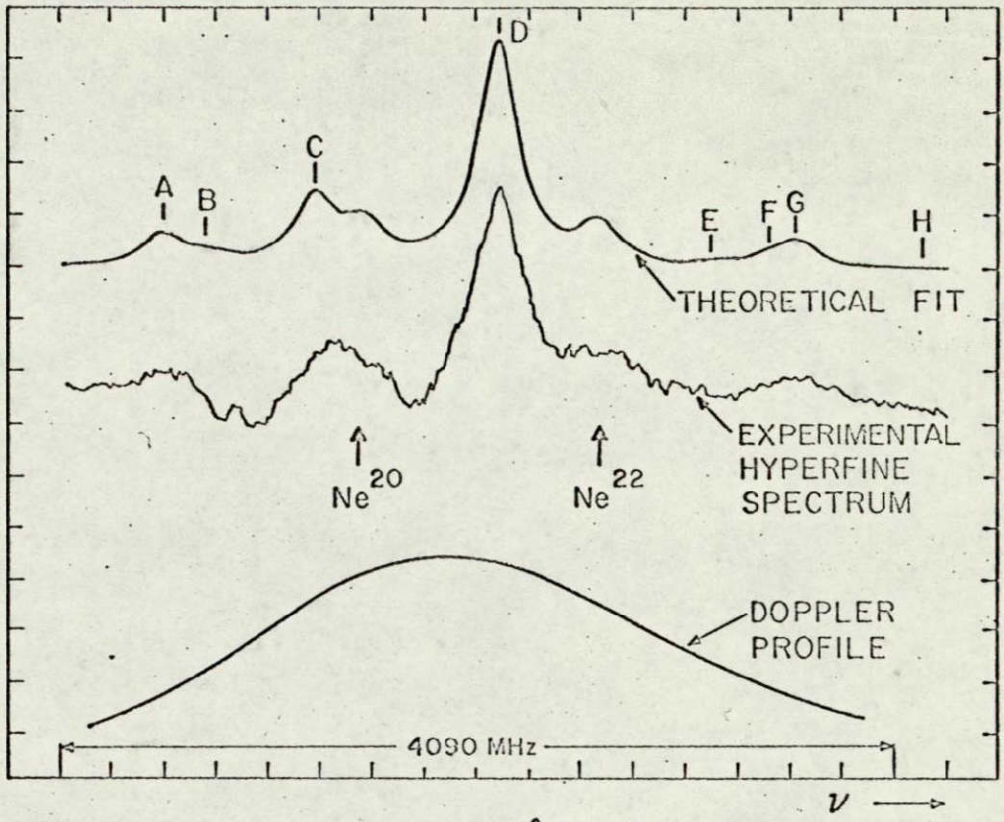

(a) Forward Traces of 6096 Å Spontaneous Emission

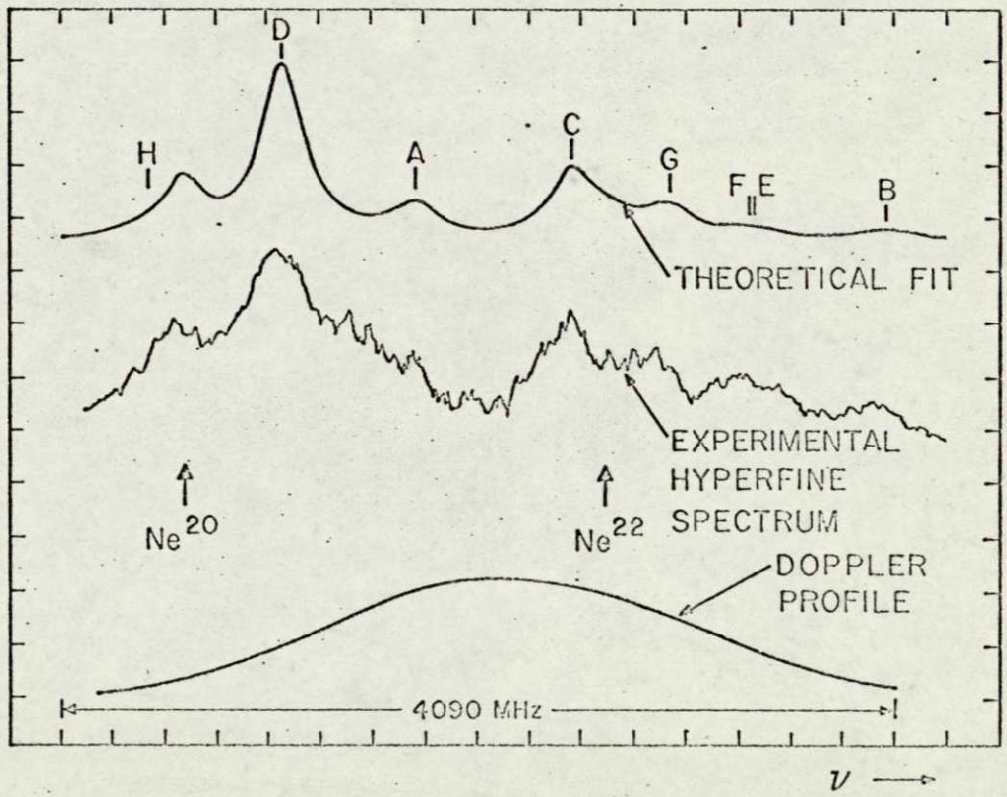

(b) Backward Traces of 6096 Å Spontaneous Emission

FIGURE CAPTIONS

Fig. 1 Hyperfine splitting of $1s_4$, $2p_4$ $2s_2$ levels in Ne^{21}.

Fig. 2 Experimental Arrangement. Note the different configurations for observing forward and backward 6096Å spontaneous emission.

Fig. 3 Comparison of experimental traces and theoretical fit. Note that the Doppler profiles for forward and backward traces completely mask the hyperfine structure. The change signals labeled are the eight most prominent, and are associated with three level cascade systems of the type $F \to F^1 \to F^{11}$. Denoting these systmes as ordered triplets, they are: A= (3/2, 3/2, 1/2); B= (3/2, 5/2, 5/2); C= (3/2, 3/2, 3/2); D= (5/2, 7/2, 5/2); E= (5/2, 5/2, 3/2); F= (1/2, 1/2, 1/2); G= (3/2, 5/2, 3/2); H= (5/2, 5/2, 5/2).

For these computer fits to the data γ_F=265 MHz and γ_B=225MHz. Of these widths ∿100MHz is instrumental. Also, the Doppler width $k_1 u$=2500MHz.

TABLE CAPTIONS

Table 1 Theoretical expression for intensity pattern of change signals.

Table 2 Experimental results for h.f. interaction constants and values for $1/r^3_{2p\ hole}$, Q', and a_{3s}.

Table 3 Observed isotope shifts at 6096Å and 1.15μ in $Ne^{20,21,22}$.

APPENDIX B. OBSERVATION OF INTENSE SUPERRADIANT EMISSION IN THE HIGH GAIN INFRARED TRANSITIONS OF HF AND DF MOLECULES

J. Goldhar, R. M. Osgood, Jr. and A. Javan.

ABSTRACT

Intense stimulated emission (superradiance) is obtained in several high gain transitions of HF and DF molecules. The narrowing of the linewidths of the high gain transitions are observed in detail. Pulsed energy and peak powers are comparable with those obtainable in a similar transverse CO_2 laser.

This letter reports the observations of intense stimulated emission (superradiance)in a number of high gain, rotational-vibrational transitions of HF and DF molecules in the 2.7μ and 3.8μ range of wave-length respectively.[1,2] The vibrationally excited molecules are produced with a transverse pulsed discharge in a flowing mixture of molecular hydrogen (or deuterium) and SF_6 gas, at relatively high pressure. The spectral distribution of the individual high gain transitions have been studied with a pneumatically tuned Fabry-perot interferometer. Each of the superradiant transitions is found to show considerable line-width narrowing due to substantial amplification of the traveling optical wave. In addition, it is found that in the presence of a regenerative optical feedback (i.e . with the device used as a laser with an optical resonator), the laser oscillation on each line occurs mainly in a single resonator mode. With regard to the obtainable peak power and the pulse energy, the performance of the system is competitive with that obtained at 10.6μ using a CO_2 laser excited by means of a similar transverse pulsed discharge.

In the experiment, the laser configuration consisted of a 50 cm long transverse discharge [3] with 101 equally spaced pin electrodes arranged in a row facing a long cylindrical brass, anode across a 2.5 cm gap. A 0.01 μF capacitor at high voltage is discharged across the tube through a 1000 ohm resistor in series with each pin. The discharge tube was terminated with CaF_2 Brewster windows. Gases were introduced into the system by means of standard needle valves and flow was maintained with a 10 CFM fore pump.

In the experiment, most of the detailed observations were made with the hydrogen gas. Typically, the partial pressure ratio of SF_6 to H_2 was 10:1. In this system, the vibrationally excited HF molecules are formed through chemical reaction [4] of the fluorine atoms, (which exist as a byproduct of the SF_6 dissociation), and the molecular hydrogen. As noted earlier, [2] this reaction is 31.7 kcal/mole exothermic for HF and DF, and hence capable of producing vibrationally excited HF up to the vibrational level v=3/(and up to v=4 in DF).

The distribution of infrared output radiation among the various rotation-vibration transitions in HF, is found to be dependent on the operating conditions such as flow rate, partial and total pressure, and applied voltage. If the device is operated as a laser with a regenerative optical feedback, at relatively low pressures of SF_6 and H_2 and low applied voltage, (below about 10k.v.), the output is distributed among several rotation-vibration transitions of each of the three v=3→2, 2→1 and 1→0 vibrational bands.[5] At the elevated pressures and for the applied voltages in the regions of about 15 kilovolts (or higher), the laser output spectrum tends to peak in the v=1→0 transition with P (4) the most energetic line. This behaviour indicates that at the elevated pressures and voltages, (where the HF population is appreciable), the HF molecules in the v→1 states decay rapidly to the v=1 state, causing a build-up of population in the v=1 state, which apparently decays at a slower rate.[6]

An important characteristic of this system is its capability of producing very high gains leading to intense stimulated

emission without regenerative optical feedback (superradiance). In analyzing the output spectrum of the superradiant device, it was most essential to guard against unwanted optical feedback introduced by small reflections or scattering from auxiliary optical components present in the path of the output beam. This was done by introducing heavily absorbing filters placed at an angle in the path of the output beam and appropriately misaligning the various components to prevent the feedback. Such precautions were particularly important when a folding mirror was placed at one end of the amplifier to obtain double pass amplification at the output. Fig. 1 shows the method used to monitor the presence of an unwanted optical feedback. A sample output was provided by placing a beam splitter on the amplifier axis near the folding mirror. When the light emanating from the output end of the amplifier was interrupted, the presence of any feedback exterior to the amplifier could then be detected as a signal appearing at the sampling output.

In the high pressure region (about 200 torr SF_6 and about 20 torr H_2), it was possible to obtain intense stimulated emission on the P(4), v=1→0 and P(3), v=2→1 transitions with the amplifier used in a single pass; the P(4), v=1→0 was generally found to be more intense.

A pneumatically scanned Fabry-Perot interferometer with a 8.26 cm mirror separation was used to analyze the spectral distribution of each high gain transition. In this system, the output of the interferometer was detected through a small pinhole with an infrared detector. The interferometric analysis of the spectral distribution in each superradiant transition showed a

full-width at half maximum below 110 MHz. The 110 MHz limit was instrumental, determined by the finesse of the Fabry-Perot. This result was obtained with the amplifier used in both the single and double pass configurations.

An additional noteworthy behaviour of the system is that under the superradiant conditions, it is possible to obtain stimulated emission with sufficient intensity to cause amplifier saturation even for a single pass amplifier. This was observed by noting that at the limit of highest gain, the double-pass amplifier output on the P(4), v=1→0 transition was only about 20 times larger than that obtained in the single pass. Furthermore, using the feedback monitor described above, the sampled signal of the double pass amplifier with no feedback was compared with that of the amplifier used as a laser with a complete regenerative feedback. The power level in the latter case was found to be only a few times higher than that of the double pass amplifier

Under the high pressure condition where the amplifier gain is near optimum, the spontaneous emission linewidth is essentially due to collision broadening. The exact magnitude of this broadening is not as yet known for the HF transitions. However, in the presence of about 200 torr SF_6 pressure, the spontaneous emission line width can be assumed to be at least about 3000 MHz. Accordingly, the observed 110 MHz line width limit corresponds to a line narrowing of 30 or greater. In the absence of saturation, this factor is known to be given by the square root of GL where G is magnitude of the gain per unit length and L is the amplification path length. However, it is important to guard against hasty application of this relationship in obtaining an accurate measure

of the amplifier gain in this system. For instance, it is probable that the presence of each pin electrode in the amplifying medium can cause appreciable scattering of the infrared emission to introduce sufficient feedback to cause additional narrowing of the line profile.[7] Furthermore, the saturation effect is also expected to play an appreciable effect on the line-shape.

The frequency spectrum of each oscillating line was also analyzed when the device was used as a laser with two aligned mirrors providing complete regenerative feedback. Interestingly, the frequency spectrum of each oscillating line, as averaged over a number of pulses, was found to be distributed within a frequency interval below about 70 MHz resolution limit of the Fabry-Perot[8]. In this case, a much broader spectrum is expected because of the possibility of the laser oscillating on several longitudinal modes of the laser resonator which was 118 cm long (corresponding to 130 MHz mode frequency spacing). The narrow line-width for each oscillating line was observed while the gas pressure and the applied voltage and hence the gain in the various transitions were varied over a wide range. (The lowest total gas pressure was somewhat less than 10 torr). While it is tempting to attribute this persistent behaviour to the high gain property of the medium, it is more likely that the effect originates from mode coupling in the presence of collision broadening. For a collision broadened line, the saturation effect decreases the gain uniformly over the whole line profile leading to mode competition . In general, however, complete single moding is not always expected for a collision broadened line due to the so called " spatial hole burning" effect. This effect occurs

in a region of space within the resonator where the crest of the standing wave for one mode falls near the node of another. This would allow coupling of both modes to the amplifying medium when the molecular mean free path is appreciably below one wavelength - a condition valid for a fully collision broadened line.

In our system, however, the spatial hole burning of this type may be smeared because of rapid density fluctuations and the acoustical waves caused by the high current discharge pulse[9]. This would inhibit multimoding on, say, several longitudinal modes but would allow simultaneous oscillation on a longitudinal and a transverse mode having appreciably different intensity distribution in the direction transverse to the laser axis. The latter possibility was verified by using an appropriate pair of curved laser mirrors to introduce transverse modes separated in frequency by tens of MHz from the corresponding longitudinal modes. With a fast response infrared detector, it was possible to obtain beat notes in the appropriate frequency regions dependent, as expected, on the degree of aperturing of the laser resonator. This result indicates the possible simultaneous presence of one longitudinal and several transverse modes at frequencies falling within the 70 MHz limit of the Fabry-Perot.

Study of the output power obtainable from this sytem has revealed an important practical property; namely, that the system is potentially capable of supplying considerable energies and high peak powers in each pulse. The optimum power and efficiency was found to be an increasing function of the applied voltage. At the 20 kv limit of the available high voltage supply, it was possible to obtain 16 kw peak power (corresponding to 0.6% efficiency) in a pulse of 700 ns duration. This was obtained in

a mixture of SF_6, H_2 with partial pressures of 300 and 10 torr respectively. This result suggests that by increasing the applied voltage and scaling the volume and the gas pressure, it is possible to obtain much larger output powers, competitive with those reportedly obtainable in the transverse discharge CO_2 laser.

With the D_2 gas used instead of H_2, it was possible to obtain intense stimulated emissions on the DF transitions in a manner similar to that observed in HF, as described above. With the amplifier used as a laser with regenerative feedback, the DF oscillations appeared over several transitions in the $v=4\rightarrow3$; $v=3\rightarrow2$, $v=2\rightarrow1$, and $v=1\rightarrow0$ bands. In the high pressure region, the lines capable of intense superradiant emission were P(5) and P(6) of both the $v=2\rightarrow1$ and $V=3\rightarrow v=2$ bands. More detailed studies of the pressure dependence of the DF spectrum are now in progress.

In conclusion, we would like to point out that the high pressure transverse gas discharge provides a general method of extracting high peak powers and pulse energy for many other gas laser transitions. For instance, we have recently observed intense laser oscillations in the 5μ bands of Pure CO excited by a transverse gas discharge at relatively high pressures. Detailed study of the system will be published separately [10].

We would like to acknowledge Dr. F. Zernike for making available the Fabry-Perot flats used in the experiment. We would also wish to thank Mr. Ronald McNair and W. L. Ryan for their expert technical assistance. Lastly, we are grateful to Prof. E. V. George and Dr. R. Carbone for numerous helpful discussions.

1. Laser oscillations in the 2.7μ and 3.8μ bands of HF and DF molecules formed chemically in a gaseous discharge, were separated sometime ago by T. F. Deutsch, Appl. Phys. Letters, 10, 234, 1967. Similar results obtained in a transverse discharge at the 2.7μ band of HF have recently been reported by M. C. Lin and W. H. Green, J. Chem. Phys. 53, 3383, 1970. See also C. J. Ultee, IEEE J. of Quantum Electronics, QE-6, 647, 1970. This publication shows the possibility of obtaining large gains in an electrically pulsed, chemical HF laser.
2. For chemical HF, DF lasers produced in a supersonic flowing mixture of D_2 or H_2 with thermally heated SF_6, see D. J. Spencer, H. Mirels, and T. A. Jacobs, Appl. Phys. Letters 16, 284, 1970. For the application of flash photolysis, see J. H. Parkes and G. C. Pimentel, J. of Chem Phys., 51, 91, 1969.
3. A. J. Beaulieu, Appl. Phys. Letters, 16, 504, 1970.
4. Parkes and Pimentel, J. of Chem. Phys., 51, 91, 1969.
5. The transitions in the $v=3\rightarrow2$ and $v = 2\rightarrow1$ bands ranged from P(3) to P(6) with P(3) generally being more intense. In the $v=1\rightarrow0$ band the transitions P(4) through P(6) were observed with P(4) being the most intense.
6. In this process, the rapid decay of the HF molecules in the $v>1$ states to the v=1 will be dominated by v-v type collisions with HF molecules in the v=0 state. However, the slower decay of the v=1 state will result from collisions with H_2 and SF_6 molecules.

7. Under the high gain conditions, it was possible to trigger the amplifier into oscillation with a diffuse regenerative feedback. For instance, by holding a sheet of paper at the output end of the folded amplifier, it was possible to obtain strong oscillations.

This could be detected by means of the feedback monitor (see Fig. 1). For a discussion of non-resonant feedback and its implications see R. V. Ambartsumyan, N. G. Basov, P. G. Kryukov and V. C. Letokhov JETP 24, 481 1967; and R. V. Ambarsumyan, P. G. Kryukov and V. C. Letokhov JETP 24, 1129, 1967.

8. When the device was used as a laser with regenerative feedback, the interferometer could be better aligned with respect to the incident beam without introducing feedback into the laser. Accordingly, a better system finesse was then obtained.

9. An additional source of the smearing of the spatial hole burning may also arise from a rapid variation of the refractive index during the build up of radiation within the resonator causing a wavelength sweeping of each mode. Such an index change may arise from molecular dissociation due to the current pulse and the build-up of population in the high gain amplifying transitions contributing to the refractive index.

10. Osgood, Goldhar and McNair to be published in Journal of Quantum Electronics.

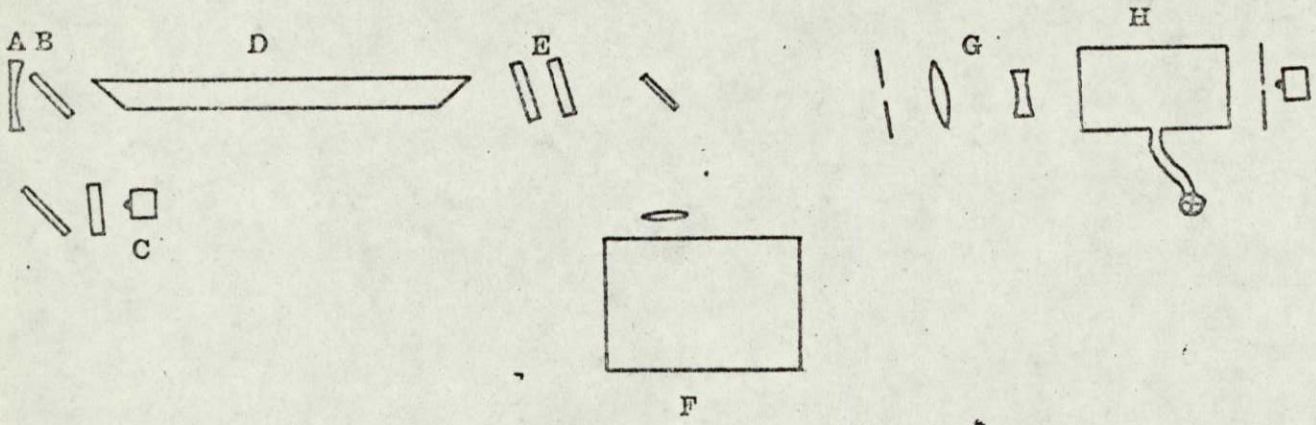
A B
D
E
G
H
C
F

CAPTIONS

Fig. 1: Experimental apparatus for Analyzing the Behaviour of the Superradiant Device.

A) Folding Mirror; B) Sampling;

C) Sampling detector with filter beamsplitter;

D) Discharge tube; E) Absorbing Filters

F) Monochrometers G) Collimator

H) Febry-Perot Interferomater with pressure scanning valve, pinhole and detector.

APPENDIX C. FLUORESCENCE INDUCED BY COHERENT OPTICAL PULSES

H. P. Grieneisen, N. A. Kurnit and A. Szöke

ABSTRACT

A coherent electromagnetic field, resonant with an optical transition, drives the molecules of a gas into the upper and lower states alternately, unless relaxation is too fast. The observation of this coherent excitation of optical levels by fluorescence measurement is discussed and experimental results are presented. The 4.3μ fluorescence of CO_2 gas excited by a 10.6μ laser is studied; values for the dipole moment and relaxation times are obtained in good agreement with those obtained by other methods.

Studies of photon echoes,[1] adiabatic rapid passage,[2] transient nutation,[3] and self-induced transparency[4] have extended into the optical region many of the methods used in magnetic resonance for probing relaxation processes. This letter presents results on a related, sensitive method of examining relaxation effects by the measurement of fluorescence[5,6] excited by a coherent, monochromatic optical pulse in an optically thin sample.[7] In this case, a simple and direct correspondence between the analysis and the experimental results emerges; complications from nonlinear propagation effects[3,4] do not appear.

We consider an atom or molecule in a gas with three energy levels of primary interest. The system is initially in state 1; a resonant optical pulse excites the system coherently to state 2, and the system subsequently decays to state 3 (possibly identical to state 1) while radiating spontaneously. The optical electric field of the running wave pulse, at the position of the atom, x, is described by:

$$\vec{E}(x,t) = \vec{\varepsilon}\mathcal{E}(x,t)\cos(\omega t - kx) \tag{1}$$

where $\vec{\varepsilon}$ is the polarization vector, $\mathcal{E}(x,t)$ is a slowly varying envelope, and $\omega \approx \omega_{12}$ is the optical carrier frequency, possibly also varying slowly in time. During the pulse the equation of motion of the density matrix ρ can thus be approximated by that of a two-level system:

$$\dot{\rho} = -\frac{i}{\hbar}[H,\rho] - \begin{pmatrix} (\rho_{11}-\rho_{11}^{eq})/T_1 & \rho_{12}/T_2 \\ \rho_{21}/T_2 & (\rho_{22}-\rho_{22}^{eq})/T_1 \end{pmatrix} \tag{2}$$

where the Hamiltonian $H = H_o - \vec{\mu}_{op}\cdot\vec{E}(x,t)$ consists of the unper-

turbed part, H_o, having the energy levels 1, 2, and the interaction of the optical field with the electric dipole moment of the atom, $\vec{\mu}_{op}$. The relaxation is treated phenomenologically (Bloch equations), it is characterized by the decay time of the energy, T_1, and that of the coherent dipole moment, T_2. The relaxation can be caused by radiative processes, collisions,[8] or diffusion. A more detailed account is beyond the scope of this letter. Eq. (2) can be integrated (as a rule numerically), with the initial condition $\rho_{ij}(t=0) = \rho^o_{11}\delta_{i1}\delta_{j1}$, to give the value of $\rho_{ij}(t=t_a)$ after passage of the pulse. If for simplicity we assume that the lifetime of the excited population is much longer than T_2, the decay of $\rho_{22}(t>t_a+T_2)$ can be considered separately since $\rho_{12}\to 0$. Thus the fluorescence intensity probes the upper state population at the end of the pulse. We can illustrate the expected results in some simple cases:

1) No relaxation, field on resonance for all the atoms. Eq. (2) can be integrated immediately in the rotating wave approximation to yield:

$$\rho_{22}(t_a) = \rho^o_{11}\sin^2 \int_o^{t_a} (\mu\mathcal{E}(x,t)/2\hbar)dt \qquad (3)$$

where $\mu = |(\vec{\varepsilon}\cdot\vec{\mu}_{op})_{12}|$. This is a dramatic effect. Increasing the field (or lengthening the pulse) first increases, then decreases the observed intensity. The period of the modulation yields the value of the dipole moment μ. Also it is a direct measure of the quantity $\theta = (\mu/\hbar)\int_{-\infty}^{+\infty} \mathcal{E}(x,t)dt$, introduced by McCall and Hahn,[4] which has importance in propagation effects. As an optically thin sample changes the value of θ only slightly, this experiment can be used as a diagnostic tool in self-induced transparency and

related studies. The angle θ is also related to the pulse energy/unit area, S, by $\theta^2 = 8\pi\mu^2 S\tau_p/c\hbar^2$, provided we define the pulse width as $\tau_p = [\int_{-\infty}^{\infty} \mathcal{E}(x,t)dt]^2/\int_{-\infty}^{\infty} \mathcal{E}^2(x,t)dt$.

2) For fast relaxation, $T_1, T_2 << \tau_p$, the steady state solution applies. For a square resonant optical pulse one has

$$\rho_{22}(t_a) = \frac{\rho_{11}^o}{2} \frac{(\mu\mathcal{E}/\hbar)^2 T_1 T_2}{1+(\mu\mathcal{E}/\hbar)^2 T_1 T_2} \tag{4}$$

It can be seen that the fluorescence increases monotonically with pulse energy, first linearly, then more slowly. The saturation field measures the product $T_1 T_2$.

In our experiment we deal with a spatially degenerate rotational-vibrational transition of CO_2. The measured fluorescence intensity is then proportional to

$$\bar{\rho}_{22}(t_a) = \int d(\Delta\omega) g(\Delta\omega) \sum_{M=-J}^{M=+J} \rho_{2M,2M}(\Delta\omega, t_a) \tag{5}$$

where $g(\Delta\omega)$ is a spectral distribution function (a Gaussian of width $\Delta\omega_D$ for Doppler-broadening).[9] In the case of spatial degeneracy, the selection rule $\Delta M=0$ for a linearly polarized field allows the transition to be treated as a collection of two-level systems, each one with its own resonance frequency and matrix element $\mu_M(J) = \mu_o(J)(1-M^2/J^2)^{1/2}$ for a P-branch transition.[10] Eq. (2) and the integral (5) have been evaluated for width $\Delta\omega_D/2\pi$ = 60MHz and for various pulse shapes on a digital computer and results are presented in Fig. 1 for some cases of interest. The fluorescence intensity is plotted against laser field strength for various T_1, T_2 values. The salient features are: At long relaxation times (low pressures) there is modulation even for

high J transitions,[11] the modulation disappears at $T_2 \tilde{\approx} \tau_p$. The fluorescence intensity is always linearly proportional to the laser intensity (quadratic in $\mathcal{E}$) at low laser powers. For $T_1, T_2 \ll \tau_p$ it becomes proportional to the square root of laser intensity (linear in $\mathcal{E}$) when $(\mu\mathcal{E}/\hbar)(T_1T_2)^{1/2} \gtrsim 1$ and finally saturates when $(\mu\mathcal{E}/\hbar)(T_1/T_2)^{1/2} \gtrsim \Delta\omega_D$.[12] The parameters μ, T_2, $(T_1T_2)^{1/2}$ can be estimated from the first minimum, the disappearance of the modulation, and the linear to square root transition region respectively.

Our experimental arrangement is shown in Fig. 2a. A 4m flowing CO_2-N_2-He laser (A), operating on the P(20) 10°0-00°1 10.6μ transition, with line selection provided by a diffraction grating (B), is Q-switched by a rotating mirror (C). Apertures (D) placed at both ends of the cavity each introduce ∿30% diffraction loss in order to eliminate off-axis modes and improve line selection, resulting in a pulse with good amplitude and shape stability (Fig. 2b). Frequency drift of the laser was corrected by moving the 90% reflecting laser output mirror (E) with a piezoelectric transducer (F). The laser gain was kept sufficiently low that detuning of the cavity mode by more than ∿4MHz from line center was readily evidenced by amplitude and shape changes in the laser pulse. The output of the laser passes through an amplifier tube (G) which provides a pulse of typically 2kW peak power and 250 n sec width at half maximum, a dimethyl ether absorption cell (H) utilized to vary the pulse intensity, and two CO_2 sample cells (I,J). It is then attenuated by filters (K) and focused by a lens (L) onto a Ge:Au detector (M) used to monitor the laser intensity and pulse shape. The 4.3μ

fluorescence from the 00°1 to 00°0 CO_2 level (see Fig. 2c) was observed with InSb detectors (N). The second sample cell (J), containing CO_2 at relatively high pressure (4 torr), was used to insure that nonlinearities observed in the low pressure sample were not due to undetected change in the laser frequency or pulse shape.

In order to obtain uniform intensity in the low pressure sample cell (I), a 5mm dia. aperture was placed inside the cell in the center of the beam. This, together with a 7mm aperture placed 4 cm behind it, limits the field of view of the detector to this central 4 cm region, a distance in which diffraction of the laser beam does not produce serious nonuniformities. These apertures also served to reduce a linear background signal believed to orginate from CO_2 adsorbed on the cell windows. The laser profile at the position of the first aperture was measured to be uniform to within 30%, which gives a sufficiently small field variation to avoid severe smoothing of the experimental curve. Attenuation of the laser resulted in no detectable change in the laser profile.

The possibility of a frequency chirp[13] during the laser pulse, which would greatly alter the nature of the observed effect (see Fig. 1b), was checked both by beating the laser against a cw CO_2 laser and by splitting the pulse and recombining it in an interferometric arrangement with a 12m delay in one arm. The latter technique is sensitive to small frequency changes during the pulse, provided the pulse shape is stable. By careful adjustment of the position of the aperture near the rotating mirror, the frequency chirp could be kept under 2MHz during the pulse

($d\omega/dt \leq 4 MHz/\mu sec$).

Although fluorescent signals were directly observable on an oscilloscope even at our lowest pressure (0.05 torr), signal averaging was necessary in order to obtain accuracy.[14] It is interesting to note that at 0.05 torr, in the region of $\mu\mathcal{E}\tau_p/\hbar = \pi$, the signal originates from approximately 2×10^9 excited molecules. This sensitivity compares well with magnetic resonance.

Experimental data (Fig. 3) reproducibly shows modulation of the fluorescence intensity at a pressure of 0.05 torr. This determines the laser intensity in terms of θ. In order to compare our data with theory, the above analysis must be modified. In CO_2, rotational relaxation is the main T_1 mechanism: once a resonant molecule suffers a collision which changes its rotational state, it no longer interacts significantly with the radiation field. It nevertheless contributes to the measured signal since fluorescence is observed from all rotational levels of the 00°1 vibrational state to the ground state. The proper expression for comparison with our data is thus

$$I_{4.3\mu} \propto \rho_{22}(t_a) + \int_o^{t_a} (\rho_{22}(t)/T_1)\,dt \qquad (6)$$

One effect of this additional term is to cause the modulation to disappear more rapidly as the relaxation times are made shorter than τ_p. Also, the fluorescence increases for shorter T_1 because rotational thermalization tends to restore the population of both interacting levels to their equilibrium values.

An additional complication is the presence of radiation trapping, which introduces a pressure dependence in the relationship between observed fluorescence and excited population.

The data plotted in Fig. 3 are proportional to the intensity of fluorescence immediately after the pulse, normalized to CO_2 pressure and multiplied at each pressure by a factor R(p) introduced to account for radiation trapping. At low pressures, a correction has also been made for a residual linear background signal. Theoretical curves are shown utilizing the known relaxation rate of $1/T_2 = 2 \times 10^7$/torr-sec obtained from pressure broadening studies,[15,16] together with a value of $1/T_1 = 10^7$/torr-sec[17] in Eqs. (2) and (6). The set of numbers R(p) which produce agreement with these theoretical curves (see Fig. 3) is consistent with the trapped lifetimes measured by Kovacs and Javan.[6] However, the uncertainty in this trapping factor for our cell geometry and the insensitivity to T_1 of the curves resulting from Eq. (6) prevent an accurate determination of T_1. Variation of T_2 by 50% produces significantly worse agreement with the set of theoretical curves. The measured τ_p of 0.56 μsec and energy/unit area of 0.024 mJ/cm^2 in the region of the 2π condition give a value of $\mu_{oz}(P20) = (2.0 \pm 0.4) \times 10^{-20}$ esu, in agreement with the value of 1.7×10^{-20} esu deduced from absorption measurements.[15]

The example discussed above shows the potential of the fluorescence method for the measurement of the dipole matrix elements and the relaxation parameters T_1 and T_2 in gases in the presence of inhomogeneous broadening. Photon echoes, self-induced transparency and optical nutation measure similar parameters and thus should be compared with our method. When applicable the fluorescence method has the advantage of simplicity and sensitivity: it can measure relaxation in a sample of total absorption 10^{-5} and relaxation times as short as the pulse length itself. This feature makes the method attractive for the measurement of short

relaxation times, especially using tunable short-pulse lasers.

Despite the advantages claimed above for this technique, we think it necessary to point out certain experimental difficulties. It is necessary to have a stable, reproducible, single mode laser with negligible frequency chirp and uniform amplitude across the beam. It is also important to eliminate any linear background signal arising, for example, from gas adsorbed on cell windows. On the positive side, we note that the magnitude of the dips should be much larger than those reported here if the condition $\tau_p \leq \Delta\omega_D^{-1}$ is fulfilled.

Two simplifying assumptions were made in the derivation of Eq. 2: the third level has been neglected, and the radiative reaction on the level pair 1-2 has not been included. It can be shown, using the methods of Feld and Javan,[6] that under the influence of the strong field the radiative lifetime of the level pair 2-3 can change only up to a factor of 2. Superradiant phenomena [18] can also play an important role in determining the shape of the fluorescence curve as well as the fluorescence decay envelope, due to the enhanced rate arising from the superradiant state.[18,1] Both effects are negligible in our experiment.

In conclusion, we note that this technique is also applicable to the study of relaxation in solids and in electronically excited molecular states which are coupled to a quasi continuum of levels.[19] It can be extended to include the time development of the angular distribution and polarization of the emitted radiation, which directly measures the equilibration of the degenerate M-sublevels.

We wish to thank Prof. A. Javan for his continuous encouragement and help in this work. The initial phases of this work were done in cooperation with Dr. C. K. Rhodes, who also bequeathed much of the apparatus.

REFERENCES

1. I.D. Abella, N.A. Kurnit and S.R. Hartmann, Phys. Rev. 141, 391 (1966); C.K.N. Patel and R.E. Slusher, Phys. Rev. Letters 20, 1087 (1968); J.P. Gordon, C.H. Wang, C.K.N. Patel, R.E. Slusher and W.J. Tomlinson, Phys. Rev. 179, 294 (1969).

2. E.B. Treacy, Phys. Letters 27A, 421 (1968).

3. G.B. Hocker and C.L. Tang, Phys. Rev. Letters 21, 591 (1968); G.B. Hocker and C.L. Tang, Phys. Rev. 184, 356 (1969).

4. S.L. McCall and E.L. Hahn, Phys. Rev. Letters 18, 908 (1967); S.L. McCall and E.L. Hahn, Phys. Rev. 183, 457 (1969); C.K. Rhodes, A. Szöke, and A. Javan, Phys. Rev. Letters 21, 1151 (1968); H.M. Gibbs and R.E. Slusher, Phys. Rev. Letters 24, 638 (1970); F.A. Hopf and M.O. Scully, Phys. Rev. B1, 50 (1970); F.A. Hopf, C.K. Rhodes and A. Szöke, Phys. Rev. B1, 2833 (1970).

5. We know by private communication that many of our colleagues have considered similar experiments: S.R. Hartmann, N.A. Kurnit and I.D. Abella in Ruby; F.T. Arecchi, ourselves and A. Javan, and R.T. Hodgson on the 5401Å line of Ne. A preliminary account of the underlying theory can be found in C.K. Rhodes and A. Szöke, Phys. Rev. 184, 25 (1969) Appendix B, also in the thesis of C.K. Rhodes (M.I.T. 1969 unpublished).

6. Previous spontaneous emission studies have utilized other techniques to obtain related information. See for example: R.H. Cordover, P.A. Bonczyk and A. Javan, Phys. Rev. Letters 18, 730, 1104(E) (1967); H.K. Holt, Phys. Rev. Letters 20, 410 (1968); M.S. Feld and A. Javan, Phys. Rev. 177, 540 (1969);

M. Kovacs, D. Ramachandra Rao and A. Javan, J. Chem. Phys. 48, 3339 (1968); M. Kovacs and A. Javan, J. Chem. Phys. 50, 4111 (1969); M. Kovacs, Thesis (M.I.T., 1969, unpublished).

7. Let α be the linear absorption coefficient (in cm^{-1}) of a sample whose length is L cm. We define a sample for which $\alpha L \ll 1$ as optically thin. Under these circumstances the x-dependence of the pulse may be neglected.
8. The collisional relaxation problem in gases is discussed in more detail by S.G. Rautian and I.I. Sobelman, Usp. Fiz. Nauk 90, 209 (1966) (Sov. Phys. Uspekhi 9, 701 (1967); B.L. Gyorffy, M. Borenstein and W.E. Lamb, Jr., Phys. Rev. 169, 340 (1968); C.H. Wang and W.J. Tomlinson, Phys. Rev. 181, 116 (1969); E.G. Pestov and S.G. Rautian, JETP 56, 902 (1969) (Sov. Phys. JETP 29, 488 (1969)).
9. In the presence of collisions this description is not general enough. See Ref. 8. Large deviations from our simplified theory are not expected over the range of this experiment.
10. For a more complete derivation see C.K. Rhodes, A. Szöke and A. Javan, Ref. 4; C.K. Rhodes and A. Szöke, Ref. 5.
11. This may be the reason why Hocker and Tang (Ref. 3) have seen the nutation effect. Their theoretical expressions (see also C.L. Tang and H. Statz, Appl. Phys. Letters 10, 145 (1968)) are not equivalent to ours in that they postulate a collision mechanism which strongly couples the degenerate sublevels without loss of phase.
12. This is a characteristic feature of "power broadening" in an inhomogeneously broadened line, where (4) changes to

$$\bar{\rho}_{22}(t_a) = (\rho_{11}^{o}/2)(\mu\mathcal{E}/\hbar)^2 T_1 (\Delta\omega_D/2)^{-1}(1+(\mu\mathcal{E}/\hbar)^2 T_1 T_2)^{-1/2}.$$

13. E.B. Treacy, Proc. IEEE 56, 2052 (1968); R.L. Abrams, JQE 5, 522 (1969).

14. For this purpose the availability of a PDP-12 computer greatly facilitated the ease and speed of data taking. The rapidly convergent fast algorithm, $Y_n = Y_{n-1} + (X_n - Y_{n-1})/2^k$; $n/2 \leq 2^k < n$, where X_n is the nth experimental value and Y_n is an approximation to the average of the first n samples, allowed averaging and display of 32 points on each of 2 signals at a 120 cycle rate, so that 2000 samples could be averaged in under 20 sec.

15. U.P. Oppenheim and A.D. Devir, J.Opt. Soc. Am., 58, 585 (1968); D.W. Ducsik and E.D. Hoag, App. Phys. Letters (to be published).

16. C. Freed and A. Javan, App. Phys. Letters 17, 53 (1970).

17. P.K. Cheo and R.L. Abrams, App. Phys. Letters 14, 47 (1969).

18. R.H. Dicke, Phys. Rev. 93, 99 (1954), D.C. Burnham and R.Y. Chiao, Phys. Rev. 188, 667 (1969); F.T. Arecchi and E. Courtens, Phys. Rev. A2, 1730 (1970).

19. M. Bixon and J. Jortner, J. Chem. Phys. 48, 715 (1968).

FIGURE CAPTIONS

Fig. 1. Population of upper level as function of θ, calculated for various pulse shapes (S=square, H=approximate hyperbolic-secant, A=approximation of actual pulse of Fig. 2b) with τ_p=0.6 μsec and for $\Delta\omega_D/2\pi$=60 MHz. (a) No relaxation. P,Q indicate average population of degenerate sublevels of high J, $\Delta J=\pm 1$ or $\Delta J=0$ transition. (b) Effect of frequency chirp of 4 MHz/μsec. (c). Effect of relaxation, labeled by T_2,T_1 values (in μsec) as follows: B=∞,D=1, I=0.1, L=0.0125.

Fig. 2. (a) Schematic of experimental apparatus (see text for details). (b) Multiple exposure of laser pulses, 100 nsec/div. (c) Relevant transitions in CO_2.

Fig. 3. Observed fluorescence normalized to CO_2 pressure and multiplied by trapping factor R(p) as function of square root of laser intensity (in units of θ). Theoretical curves from Eq.6, labeled by T_2,T_1 values (in μsec) as follows: C=2, D=1, E=0.5, F=0.25, G=0.2, I=0.1, J=0.05, K=0.025, L=0.0125.Origin is displaced for clarity. Error bars indicate typical uncertainty.

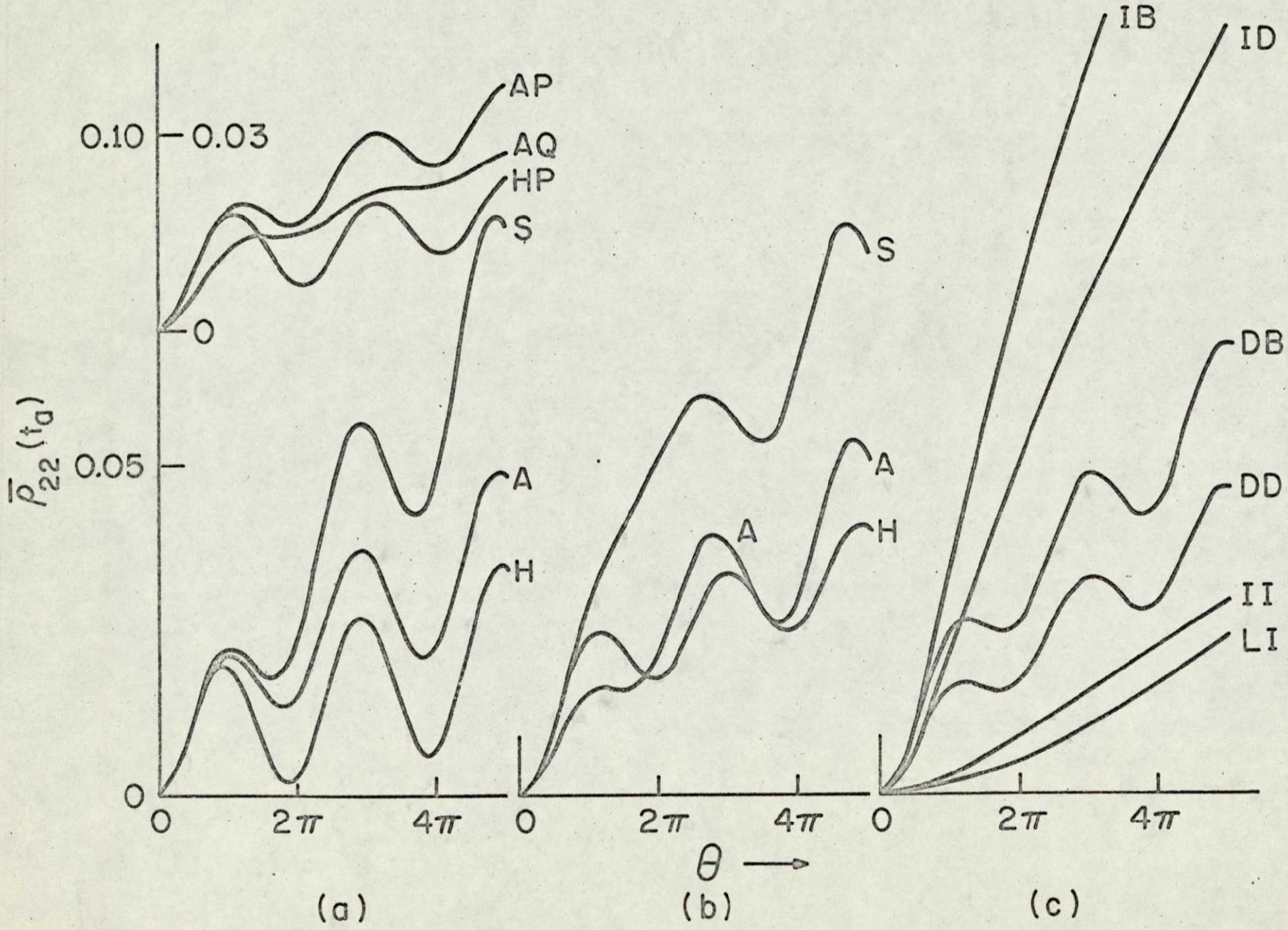
0.10
0.03
0.05
0
$\bar{\rho}_{22}(t_a)$
AP
AQ
HP
S
A
H
0
2π
4π
θ
IB
ID
DB
DD
II
LI
(a)
(b)
(c)

Fig. 1

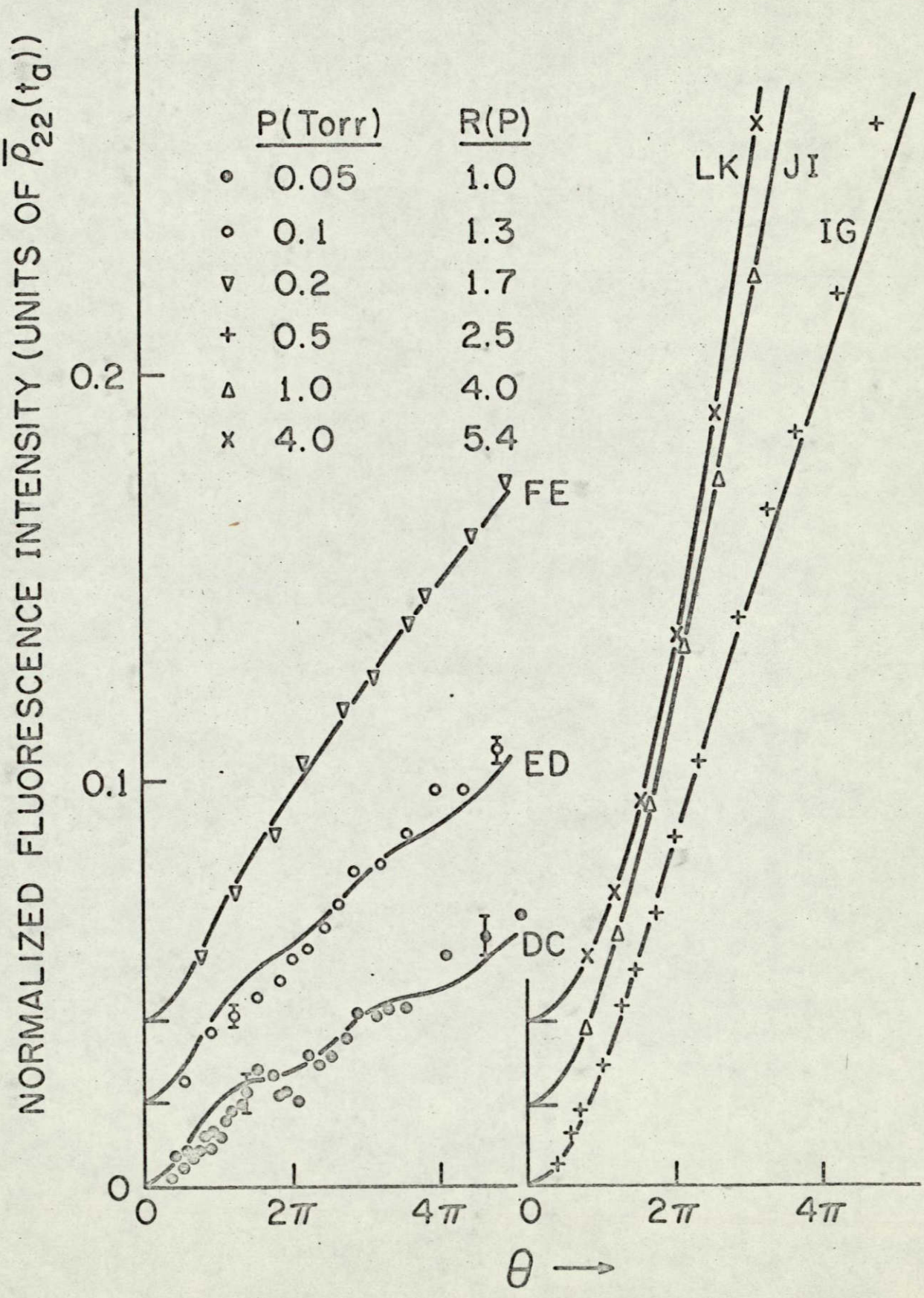
NORMALIZED FLUORESCENCE INTENSITY (UNITS OF $\bar{\rho}_{22}(t_d)$)
P(Torr)
R(P)
0.05
1.0
0.1
1.3
0.2
1.7
0.5
2.5
1.0
4.0
4.0
5.4
FE
ED
DC
LK
JI
IG
0.2
0.1
0
0
2π
4π
0
2π
4π
θ

Fig. 3

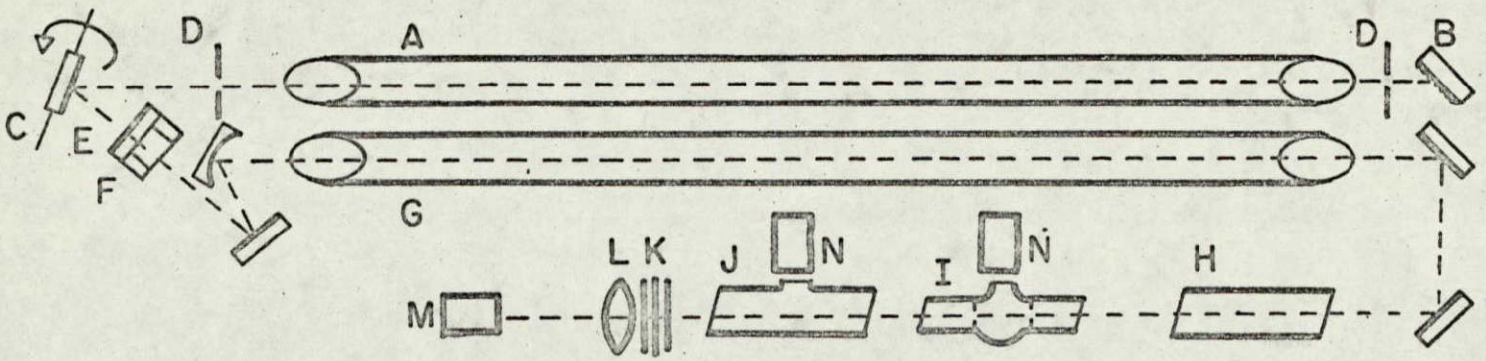

(a)

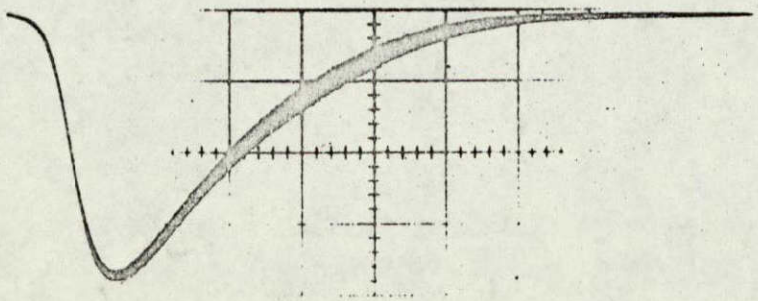

(b)

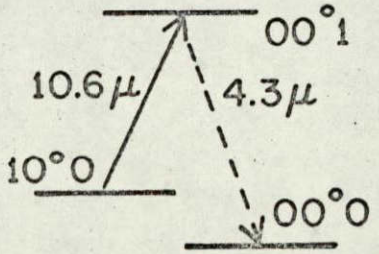

(c)

Fig. 2

APPENDIX D. LASER-INDUCED LINE-NARROWING EFFECTS IN COUPLED DOPPLER-BROADENED TRANSITIONS. II: STANDING WAVE FEATURES

B. J. Feldman and M. S. Feld

Abstract

Previous theoretical results on the influence of a laser on the line shape of a coupled transition -- laser induced line narrowing -- have been restricted to the case where the laser is detuned from the center of its atomic gain profile or is in the form of a traveling wave. This paper extends those results to include the case where the laser is an intense standing wave field tunable to the center of its atomic gain profile (conditions for Lamb dip). The effect may be observed either in transmission, by probing the coupled transition with a weak traveling-wave field coaxial with the laser field, or else in spontaneous emission from the coupled transition viewed along the axis of the laser field. It is now well-known that for a laser detuned from the center of its atomic gain profile, two narrow Lorentzian resonances of different widths appear superimposed upon the broad background signal at frequencies symmetrically located about the corresponding line center. When the laser is tuned to the center of its gain profile, however, additional fine structure develops. This structure, which is particularly significant when the laser field is intense, may have important applications in high resolution spectroscopy and laser frequency stabilization. In this paper the laser frequency may be smaller or larger than the frequency of the coupled transition. In the latter case an intense laser introduces additional splitting effects, even when the laser is detuned. Splitting effects due to weakly saturating laser fields are also discussed. The problem is formulated by ex-

panding elements of the ensemble-averaged density matrix in infinite series of spatial Fourier components. A perturbation technique is employed, valid for a weak probe field and a standing wave field of arbitrary intensity. One obtains an expression for emission induced by the probe field due to atoms moving with one velocity, written in terms of continued fractions in the general case and with Bessel functions in an important special case. This expression is integrated over the atomic velocity distribution by means of computer to obtain the total emission due to atoms moving with all velocities. A detailed discussion of line shape and of the physical processes involved is included.

I. Introduction

The lineshape of a Doppler-broadened transition is dramatically altered by the presence of a standing-wave laser field resonating with a second Doppler-broadened transition sharing a common level (Fig. 1a). For a laser detuned from the center of its atomic gain profile, two narrow Lorentzian resonances of different widths appear superimposed upon the broad background signal of the coupled transition at frequencies symmetrically located about its line center (Fig. 1b).[1-6] Recent observations of this effect,[7-11] called "laser induced line narrowing", confirm the predictions of the theory. The line-narrowing produced, which can be 100-1000 times narrower than the Doppler background, has been utilized in a variety of ways as a high-resolution spectroscopic technique for determining isotope shifts,[12] fine[13] and hyperfine[11, 14, 15] structure, g-factors[14, 16] and linewidth parameters.[17, 18, 19] The effect may be observed either in transmission, by probing the coupled transition with a weak traveling-wave field co-axial with the laser field, or else in spontaneous emission from the coupled transition viewed along the axis of the laser field (Fig. 2). Note that identical lineshapes will be observed in both cases since the spontaneous emission lineshape is equivalent to the line-shape of emission induced by a probe field containing a single photon in each mode.[4]

The overall features of the line-narrowing effect may be understood in terms of the velocity selection of moving atoms by the standing-wave laser field. The field selectively interacts with atoms whose velocities Doppler shift one of its traveling wave components into resonance. This produces changes in the

laser level populations over two narrow intervals symmetrically located about the center of the velocity distribution. These changes reflect themselves in the gain profile of the coupled transition. The above explanation does not account for the different widths of the two change signals, nor, as shall be seen, for the other striking lineshape features to be described below. The formulation, analysis and interpretation of these effects form the content of this paper.

Previous theoretical results[1-6] on the influence of the laser on the lineshape of a coupled transition have been limited to the case where the laser is detuned from the center of its atomic gain profile (or is weak). A detailed treatment was given in Ref. 4, the first paper in this series (which shall be referred to hereafter as "I"), using a method of calculation in which the E.M. fields are treated classically. The present paper extends this approach to the important case in which the laser is of arbitrary intensity and may be tuned to the center of its gain profile (conditions for Lamb dip). This case is of particular interest in view of the fact that recent theoretical studies[20, 21] predict that under these conditions the laser-induced change in the velocity distribution departs from a simple Lorentzian-like curve. Instead, additional fine structure develops for atoms with low velocities[22] (Fig. 3a). This fine structure does not manifest itself in the Lamb dip. We shall show below that related fine structure <u>does</u> appear in the gain profile of the coupled transition. This structure is particularly significant when the laser field is intense. An example is shown in Fig. 3b, where the fine structure is clearly discernable on the wings of the central dip. The

additional central feature of Fig. 3a results from other spatial interference effects to be described below.

When the laser field is intense other related lineshape effects can occur, even when the laser is detuned from the atomic center frequency. For example, when the laser frequency is higher than the frequency of the coupled transition under study, the narrow resonance splits into two (Fig. 4). This new effect should not be confused with another splitting effect which occurs for weak fields.[23-25] Both of these effects are treated below.

It should also be noted that the lineshape details analyzed here are of importance in considering stabilization schemes based on laser induced line narrowing effects.

This paper is divided into five sections. In Section II we set up the problem using the ensemble-averaged density matrix equations of motion. We obtain an expression for the small-signal gain profile of a transition coupled to a laser transition, valid for arbitrary values of laser intensity, laser detuning, level lifetimes, Doppler width, and relative frequencies of laser and coupled transitions. These expressions are given in terms of continued fractions in the general case and Bessel functions in important special cases. In Section III computer methods of evaluating these expressions are discussed. In Section IV we present the results in a number of special cases which emphasize the different physical effects which come into play. These results are compared with a simplified expression obtainable from a rate-equation approximation, and also with the <u>independent field approximation</u>. A brief discussion of the area (integrated intensity) properties of these results is given in Section V. Lengthy

mathematical discussions which would interrupt the continuity are deferred to appendices.

II. Theory

The theoretical problem under consideration is the interaction of a coupled Doppler-broadened three-level system with two co-axial applied fields, an intense standing-wave field resonating with the "laser" transition and a weak traveling-wave probe field resonating with the coupled transition. To be concrete we shall deal with the folded level configuration of Fig. 1a. However, the results may be easily extended to the cascade configuration.[26]

In formulating the problem it is most convenient to treat the applied fields classically. It is important to note, however, that the resulting line shape expression is also applicable to the case of spontaneous emission at the probe frequency.[27] The formalism of the ensemble-averaged density matrix is adopted. In this formalism one considers the interaction of the applied fields with atoms moving with a given axial velocity. Having obtained the response at the probe frequency, it is necessary to sum up over the entire distribution of atomic velocities. Note that in the ensemble-averaged formalism the initial conditions at which individual atoms are produced have already been averaged over, a considerable simplification.

The problem is solved by means of a perturbation technique. In the absence of the probe field the problem reduces to the interaction of a standing-wave field with a two-level system. We then consider the influence of the probe field as a small perturbation on the unperturbed system. The unperturbed problem has already been solved for arbitrary intensities and detuning of the standing-wave field in Ref. 21. Thus, we may directly substitute the required terms into the perturbation equations. In the unperturbed solution it is important to include spatial variations of high harmonic content produced by the standing-wave field in the level populations and the

induced polarization. In Ref. 21 the unperturbed solution is expanded in an infinite series of spatial Fourier components. In the present problem it is also convenient to expand the perturbation solution in spatial Fourier series. This immediately leads to an infinite set of coupled nonhomogeneous linear difference equations which may be solved subject to the appropriate boundary conditions.

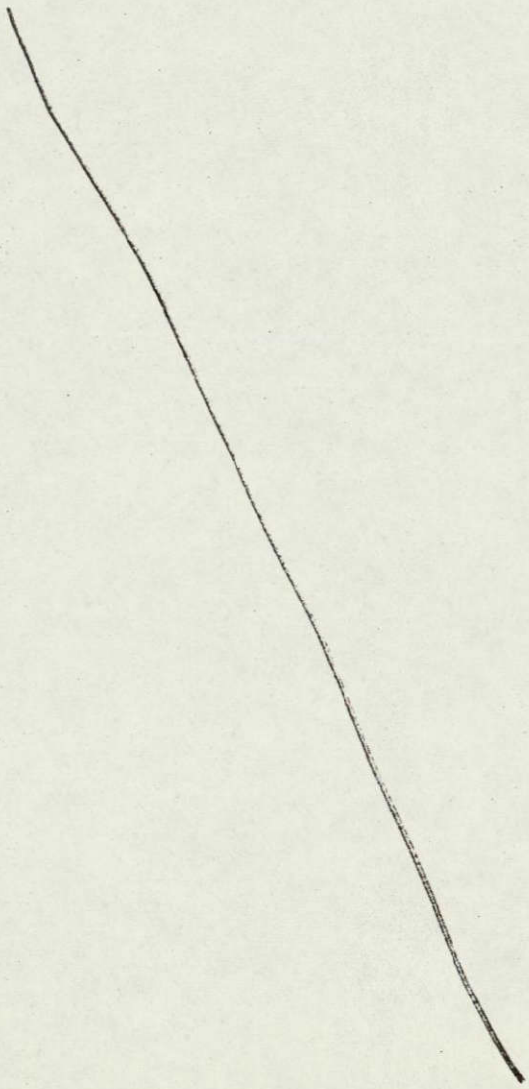

In the general case the solution may be expressed in terms of continued fractions and in important special cases in terms of Bessel functions. One then obtains an expression for the emission induced by the probe field due to atoms moving with one velocity. This expression is integrated over the atomic velocity distribution by means of computer to obtain the total emission due to atoms moving with all velocities. In certain special cases the integrations may be done analytically.

The three level system under study is of the type shown in Fig. 1a. Level 0, the common level, is coupled to levels 1 and 2 by electric dipole matrix elements μ_{10} and μ_{20}, respectively. From parity considerations, $\mu_{21}=0$ and there are no diagonal matrix elements. Denote the energy of level j by $\hbar W_j$, and let $W_0 - W_j = \omega_j$: ω_1 and ω_2 fall in the optical-infrared region. We shall assume that $|\omega_2 - \omega_1|$ is large compared to the Doppler widths so that E_1 does not resonate with ω_2, nor E_2 with ω_1. The system interacts with a strong standing wave laser field $E_2(z,t)$ at Ω_2 , a frequency close to ω_2. The resonance at ω_1 is probed by the weak field $E_1(z,t)$ at variable frequency Ω_1 . Specifically:

$$E_1(z,t) = E_1^{\circ} \cos(\Omega_1 t - k_1 z + \phi_1), \tag{1a}$$

$$E_2(z,t) = E_2^{\circ} \sin k_2 z \cos(\Omega_2 t + \phi_2), \tag{1b}$$

with

$$k_j = \Omega_j / c, \tag{1c}$$

and ϕ_1 and ϕ_2 are constant phase factors. The additional condition

$$k_2 = \frac{m\pi}{L}, \tag{1d}$$

(L=cavity length, m is an integer) is imposed on E_2 by the laser resonator. The total Hamiltonian for the system is

$$H = H_o + V, \tag{2}$$

where H_o is the Hamiltonian of an unperturbed atom with stationary states of energy $\hbar W_j$, and V is the interaction Hamiltonian,

$$V = -\mu E(z,t), \tag{3a}$$

$$E(z,t) = E_1(z,t) + E_2(z,t), \tag{3b}$$

with electric dipole operator μ.

The problem is most readily treated by means of the ensemble averaged density matrix $\rho(v,z,t)$, which describes an ensemble of atoms at coordinates $\{z,t\}$ moving with axial (z-axis) velocity v. The equation of motion of ρ, derived in Ref. 21, is given by

$$\left(\frac{\partial}{\partial t} + v\,\frac{\partial}{\partial z}\right)\rho = -\frac{i}{\hbar}[H,\rho] - 1/2\,\{\rho - \rho^o, \Gamma\}, \tag{4}$$

where [] and {} are commutator and anti-commutator brackets, respectively. The left-hand side is the total derrivative of ρ. Relaxation is accounted for in the second term on the right-hand side through Γ, which has elements

$$\Gamma_{ij} = \gamma_j\,\delta_{ij}, \tag{5}$$

where γ_j is the relaxation rate of level j. Also, ρ^o describes the steady-state ensemble, assumed spatially uniform, in the absence of applied fields:

$$\rho^o_{ij} = n_j(v)\,\delta_{ij}, \tag{6}$$

$n_j(v)$ being the steady-state population density per velocity interval in level j in the absence of applied fields. We may write

$$n_j(v) = N_j G_j(v), \tag{7a}$$

with N_j the total population density of level j and $G_j(v)$ its normalized velocity distribution:

$$\int_{-\infty}^{\infty} G_j(v)dv = 1. \tag{7b}$$

For further details regarding Eq. (4) see Ref. 21.

The partial induced polarization due to the atoms moving with velocities in the interval between v and v + dv is

$$P(v, z, t)dv = Tr[\mu\rho]\,dv. \tag{8}$$

The net polarization is obtained by considering contributions from all velocities:

$$P(z,t) = \int_{-\infty}^{\infty} Tr[\mu\rho]\,dv. \tag{9}$$

To formulate the perturbation approach let us rewrite the Hamiltonian of Eq. (2) in the form

$$H = H^u + H', \tag{10}$$

with

$$H^u = H_o - \mu E_2 \tag{11}$$

and

$$H' = -\mu E_1. \tag{12}$$

Thus, H^u is the unperturbed Hamiltonian, describing the interaction of the standing wave field with the atomic system in the absence of E_1. The corresponding unperturbed density matrix, ρ^u, is the solution to Eq. (4) with H' equal to zero:

$$\left(\frac{\partial}{\partial t} + v\frac{\partial}{\partial z}\right)\rho^u = -\frac{i}{\hbar}[H^u, \rho^u] - 1/2\,\{\rho^u - \rho^o, \Gamma\}. \tag{13}$$

The additional term H', due to the weak probe field, is taken to be a small perturbation on H^u. Thus, H' produces a small correction ρ' to ρ^u:

$$\rho = \rho^{u} + \rho' . \tag{14}$$

Inserting Eqs. (10) and (14) into Eq. (4), subtracting Eq. (13), and neglecting the $[H', \rho']$ term, which does not contribute to ρ' to lowest order in H', one obtains

$$\left(\frac{\partial}{\partial t} + v \frac{\partial}{\partial z}\right) \rho' = -\frac{i}{\hbar} [H', \rho^{u}] - \frac{i}{\hbar} [H^{u}, \rho'] - 1/2 \{\rho', \Gamma\}. \tag{15}$$

Assuming ρ^{u} is known, ρ' is completely specified by Eq. (15).

Equation (13) has been studied in detail in Ref. 21. Its solution, ρ^{u} valid for arbitrary values of E_2, has elements of the form

$$\rho^{u}_{20}(v, z, t) = \lambda^{u}(v, z) e^{i\Omega_2 t}, \tag{16a}$$

$$\lambda^{u}(v, z) = n_{02} \sum_{\text{odd } n \geq 1} \left[\Pi_n^{+} e^{ink_2 z} + \Pi_n^{-} e^{-ink_2 z} \right], \tag{16b}$$

$$\rho^{u}_{21} = \rho^{u}_{01} = 0, \tag{16c}$$

$$\rho^{u}_{ik} = \rho^{u*}_{ki}, \tag{16d}$$

$$\rho^{u}_{00}(v, z, t) = n_0 + n_{02} \sum_{\text{even } n \geq 0} \left[a_n(v) e^{ink_2 z} + \text{c.c.} \right], \tag{16e}$$

$$\rho_{22}^{u}(v,z,t) = n_2 + n_{02}\sum_{\text{even } n\geq 0}\left[b_n(v)e^{ink_2 z}+\text{c.c.}\right], \tag{16f}$$

$$\rho_{11}^{u} = n_1, \tag{16g}$$

where

$$n_{ij} = n_i - n_j. \tag{16h}$$

(In obtaining Eqs. (16) it is assumed, as stated above, that E_2 does not resonate with ω_1.) For convenience a_n, b_n and $\Pi_n^{\pm}$, obtained in Ref. 21, are given in Table 1. Note that Z_n Eq. (T 14), is a continued fraction which is to be evaluated subject to the boundary condition $Z_n \to 0$ for $n\to\infty$. The computation of Z_n is discussed in Section III.

Let us now consider Eq. (15). The weak probe field does not perturb the level populations, so that

$$\rho'_{kk} = 0, \quad k = 0,1,2. \tag{17}$$

Therefore, using Eqs. (16c) and (16g), the equations of motion of the off-diagonal martix elements of ρ may be written as

$$\left(\frac{\partial}{\partial t} + v\frac{\partial}{\partial z} + i\omega_1 + \gamma_{10}\right)\rho'_{01} = -\frac{i}{\hbar}\left[\mu_{01}E_1\left(\rho_{00}^{u} - n_1\right) - \mu_{02}E_2\rho'_{21}\right], \tag{18a}$$

$$\left(\frac{\partial}{\partial t} + v\frac{\partial}{\partial z} + i(\omega_1-\omega_2) + \gamma_{21}\right)\rho'_{21} = -\frac{i}{\hbar}\left[\mu_{01}E_1\rho_{20}^{u} - \mu_{20}E_2\rho'_{01}\right], \tag{18b}$$

$$\left(\frac{\partial}{\partial t} + v\frac{\partial}{\partial z} - i\omega_2 + \gamma_{20}\right)\rho'_{20} = -\frac{i}{\hbar}\left[\mu_{20}E_2\left(\rho'_{22} - \rho'_{00}\right) + \mu_{10}E_1\rho_{21}^{u}\right]. \tag{18c}$$

This set of equations may be solved by inserting E_1 and E_2 [Eq. (1)] in complex form:

$$E_1(z,t) = A_1 e^{-ik_1 z} e^{i\Omega_1 t} + c.c, \tag{19a}$$

$$E_2(z,t) = (A_2/2)(e^{ik_2 z} - e^{-ik_2 z})\, e^{i\Omega_2 t} + c.c. \quad , \tag{19b}$$

with

$$A_1 = \tfrac{1}{2} E_1^o\, e^{i\phi_1} \quad , \tag{20a}$$

$$A_2 = -\frac{i}{2} E_2^o e^{i\phi_2} \quad . \tag{20b}$$

The various spatial and temporal Fourier components of E_1 and E_2 drive the off-diagonal elements of ρ'. Let us consider the variations of the ρ'_{ij}. Of special importance are the coefficients of ρ'_{ij} on the left hand sides of Eqs. (18). These are associated with the resonant behavior of the induced polarization. The only important frequency components of a ρ'_{ij} are those for which $\partial \rho'_{ij}/\partial t$ cancels the $i\omega$ factor for appropriate values Ω_1 and Ω_2, thereby reducing the coefficient of ρ'_{ij} to $\gamma_{ij} + v\partial/\partial z$. Therefore, a nearly complete solution to Eqs. (18) will be of the form

$$\rho'_{01} = \Lambda(v, z)\, e^{-i\Omega_1 t}, \tag{21a}$$

$$\rho'_{21} = D(v, z) e^{i(\Omega_2 - \Omega_1)t}, \tag{21b}$$

$$\rho'_{20} = \lambda(v, z) e^{i\Omega_2 t}, \tag{21c}$$

where Λ, D and λ are time-independent. Inserting Eqs. (16a), (19) and (21) into Eqs. (18) and equating like coefficients of the complex frequency factors, one finds that $\lambda(v, z) = 0$ and that

$$(\Delta_1+iv\frac{\partial}{\partial z}+i\gamma_{10})\Lambda=\alpha^* e^{ik_1z}(\rho_{00}^u-n_1) + \frac{i}{2}\beta(e^{ik_2z}-e^{-ik_2z})D, \tag{22a}$$

$$(\Delta_{12}+iv\frac{\partial}{\partial z} + i\gamma_{21})D=\alpha^* e^{ik_1z}\lambda^u + \frac{i}{2}\beta^*(e^{ik_2z}-e^{-ik_2z})\Lambda, \tag{22b}$$

where

$$\alpha = \mu_{10}A_1/\hbar , \tag{23}$$

$$\beta = -i\mu_{02}A_2^*/\hbar , \tag{24}$$

$$\Delta_j = \Omega_j - \omega_j, \tag{25}$$

and

$$\Delta_{12} = \Delta_1 - \Delta_2. \tag{26}$$

We may proceed by expressing Λ and D in Fourier expansions in k_2z. Note in Eq. (16) that ρ_{00}^u is expanded in the even harmonics of k_2z, whereas λ^u is expanded in the odd harmonics. It directly follows from Eq. (22) that Λ will consist of the even harmonics of k_2z, and D of the odd harmonics. Therefore, the required solution will be of the form

$$\Lambda(v, z)=\alpha^* e^{ik_1z}\left[\Lambda_0+\sum_{\substack{\text{even}\\ n\geq 2}}\left\{\Lambda_n^+(v)e^{ink_2z}+\Lambda_n^-(v)e^{-ink_2z}\right\}\right], \tag{27a}$$

$$D(v, z)=\alpha^* e^{ik_1z}\sum_{\substack{\text{odd}\\ n\geq 1}}\left\{D_n^+(v)e^{ink_2z}+D_n^-(v)e^{-ink_2z}\right\}. \tag{27b}$$

The induced polarization at Ω_1, obtained from Eqs. (8) and (21), is of the form

$$P_1(v, z, t) = \mathrm{Re}\left[2\mu_{10}\Lambda e^{-i\Omega_1 t}\right]. \tag{28}$$

The average power increase per unit volume at Ω_1 induced by E_1, due to atoms located at z and moving with axial velocity v is given by

$$\Delta I(v, z)\, dvdz = -\left\langle \dot{P}_1(v, z, t) E_1(z, t) \right\rangle_{\text{time average}} dvdz. \tag{29}$$

The net power increase per unit volume is obtained by integrating this quantity over the distribution of atomic velocities and the length, ℓ of the active medium, centered at position a:

$$\Delta I = \int_{a-\ell/2}^{a+\ell/2} dz \int_{-\infty}^{\infty} dv \Delta I(v, z). \tag{30 a}$$

Making use of Eqs. (29) and (27a), and indicating velocity averages by $\langle\ \rangle$, i.e.

$$\langle O \rangle = \int_{-\infty}^{\infty} O(v)\, dv,$$

we obtain

$$\Delta I = -2\hbar\Omega_1 |\alpha|^2 \ell \left\{ \mathrm{Im} \langle \Lambda_0 \rangle + \text{additional terms of the form } \frac{\lambda}{n\ell} \langle \Lambda_n^{\pm} \rangle \right\}, \tag{30b}$$

where $\lambda = 2\pi/k_2$ is the wavelength of the intense standing-wave field. Since $\lambda/\ell \ll 1$, the additional terms are negligible as long as the $\Lambda_n^{\pm}$ do not diverge for large n. As shown in Appendix A, the convergence of the $\Lambda_n^{\pm}$ as $n \to \infty$ is a necessary condition for a physically acceptable solution. Accordingly, the additional terms may be neglected, and we obtain

$$\Delta I = -2\hbar\Omega_1 |\alpha|^2 \ell \mathrm{Im} \langle \Lambda_0 \rangle. \tag{32}$$

Note that only Λ_0 contributes to the net emitted power.

We now solve for Λ_0. Inserting Eqs. (16b), (16e) and (27) into Eqs. (22) and equating like harmonics of $k_2 z$, we obtain a set of equations which can be written in the following compact form:

$$\pm \frac{i\beta_0}{2} \left[x_{\pm}(n+1) - x_{\pm}(n-1) \right] + L(\pm n) x_{\pm}(n) = n_{02} t_{\pm}(n), \quad n \geq 1, \tag{33a}$$

$$\frac{i\beta_0}{2} \left[x_+(1) - x_-(1) \right] + L(0) x(0) = t(0). \tag{33b}$$

The following definitions have been made:

$$x_{\pm}(n) = \begin{cases} (\beta/\beta_0) D_n^{\pm} & n = 1, 3, 5 \ldots \quad (34a) \\ \Lambda_n^{\pm} & n = 2, 4, 6 \ldots \quad (34b) \end{cases}$$

$$x_{\pm}(0) = x(0) = \Lambda_0 \quad (34c)$$

$$t_{+}(n) = \begin{cases} (\beta/\beta_o)\ \Pi_n^{+} & n = 1, 3, 5 \ldots \quad (35a) \\ a_n & n = 2, 4, 6 \ldots \quad (35b) \end{cases}$$

$$t_{-}(n) = \begin{cases} (\beta/\beta_o)\ \Pi_n^{-} & n = 1, 3, 5 \ldots \quad (35c) \\ a_n^* & n = 2, 4, 6 \ldots \quad (35d) \end{cases}$$

$$t(0) = n_{02}\,[a_0 + a_0^*] + n_{01} \quad (35e)$$

$$L(\pm n) = \begin{cases} \Delta_{12} - (k_1 \pm nk_2)\, v + i\gamma_{21} & n = 1, 3, 5 \ldots \quad (36a) \\ \Delta_1 - (k_1 \pm nk_2)\, v + i\gamma_{10} & n = 0, 2, 4, 6 \ldots \quad (36b) \end{cases}$$

Equations (33a) and (33b) constitute an infinite set of coupled nonhomogeneous linear difference equations, in which the $t_{\pm}(n)$' s , known quantities determined by the unperturbed solution, act as driving terms for the $x_{\pm}(n)$' s. We are particularly interested in obtaining Λ_0, since, from Eq. (32), the emitted power is proportional to $\mathrm{Im}\Lambda_0$. It is shown in Appendix A

that the solution for Λ_0 is

$$\Lambda_0 = \frac{n_{01}+n_{02}\left\{a_0+a_0^*+\sum_{j=1}^{\infty}(-)^j\left[t_+(j)u_+(j)+t_-(j)u_-(j)\right]\right\}}{\frac{i\beta_o}{2}\left[u_+(1)-u_-(1)\right]+L(0)}, \qquad (37)$$

where

$$u_{\pm}(j) = \prod_{k=1}^{j} W_{\pm}(k), \qquad (38)$$

and $W_{\pm}(k)$ is the continued fraction

$$W_{\pm}(k) = \cfrac{\frac{\pm i\beta_o}{2}\frac{1}{L[\pm k]}}{1-\cfrac{\frac{\beta_o^2}{4}\frac{1}{L[\pm k]}\frac{1}{L[\pm(k+1)]}}{1-\cfrac{\frac{\beta_o^2}{4}\frac{1}{L[\pm(k+1)]}\frac{1}{L[\pm(k+2)]}}{1-\ddots}}} \qquad (39a)$$

evaluated subject to the condition

$$\lim_{k\to\infty} W_{\pm}(k) = 0\,. \qquad (39b)$$

For the special case $\gamma_0=\gamma_2, \Delta_2=0$ we find

$$u_{\pm}(j) = \frac{i^j J_{\tau(j)}(-\beta_o/k_2 v)}{J_{\tau(0)}(-\beta_o/k_2 v)}, \qquad (40a)$$

$$\tau(j) = \mp L(\pm j)/k_2 v, \qquad (40b)$$

where $J_\tau(z)$ represents a Bessel function of complex order τ and (real) argument z. The final expression for ΔI may be obtained from Eqs. (32), (37) and (38). The numerical evaluation of $W_{\pm}(k)$ is discussed in Section III.

III. Computer Evaluation of ΔI

The calculation of ΔI , the emitted power at Ω_1, from Eqs. (35), (37), (38), (39) and (31), requires the evaluation of continued fractions and velocity integrals. The computations have been performed on the M. I. T. 360 computer using double precision complex arithmetic. Continued fractions were evaluated by comparing the value obtained by truncating the continued fraction after j terms with the value obtained by truncating after j+1 terms. The algorithm used in calculating a truncated continued fraction of j terms is given in Appendix C. If the absolute value of the fractional difference between the two calculated values is less than 10^{-5}, the $j+1^{th}$ value is taken as the numerical answer. The $u_{\pm}$'s and y's represented as convergent continued fractions have been calculated from Eqs. (38) and Table I with all the continued fractions computed independently to insure that small errors did not propagate. In the summations in Eqs. (37) sufficient terms were included so that the absolute value of the ratio of the last value to the first is less than 10^{-6}. The convergence of this sum is a consequence of the boundary conditions, which require Λ_n to approach 0 for large n (Appendix A).

As a check, when $\gamma_0=\gamma_2$ and $\Delta_2=\Delta_1$ we have compared our continued fraction results with the Bessel function expressions and find agreement to 6 places of accuracy.

To simplify the interpretation of our results we have chosen a rectangular population distribution,

$$G_j(v) = \begin{cases} \dfrac{k_2}{69.8\gamma_{20}} & \text{for } |v| \leq 34.9\gamma_{20}/k_2 \\ 0 & \text{for } |v| > 34.9\gamma_{20}/k_2 \end{cases} \qquad (40)$$

for all values of j. This procedure greatly reduces the effects of a finite velocity distribution, which would arise had we chosen a more realistic

population distribution.[28] It would, of course, be easy to insert any desired form of $G_j(v)$ into the program.

The velocity integrations are evaluated using Simpson's rule with intervals of $.2k_2v/\gamma_{20}$. The accuracy of the integration is better than 2%. The accuracy of our calculations was checked by decreasing the step size and increasing the limits of integration. Our numerical results are in excellent agreement with the limiting case of a weakly saturating standing wave field (3rd order polarization) and with the case in which the laser is of arbitrary intensity but significantly detuned, cases for which we have obtained analytic expressions. (See discussion below.)

IV. Results

Equation (32) may be written in the following form:

$$\Delta I(\Omega_1) = \hbar\Omega_1 \langle (n_2-n_1) J_{21} + (n_0-n_1) J_{01} \rangle , \tag{41}$$

(as before, <> indicates velocity average), where

$$J_{21} = 2|\alpha|^2 \ell \mathrm{Im} \left\{ \frac{a_0 + a_0^* + \sum_{j=1}^{\infty} (-1)^j \left[t_+(j)u_+(j) + t_-(j)u_-(j) \right]}{\frac{i\beta_o}{2} \left[u_+(1) - u_-(1) \right] + L(0)} \right\} , \tag{42a}$$

$$J_{01} = -2|\alpha|^2 \ell \mathrm{Im} \left\{ \frac{1 + a_0 + a_0^* + \sum_{j=1}^{\infty} (-1)^j \left[t_+(j)u_+(j) + t_-(j)u_-(j) \right]}{\frac{i\beta_o}{2} \left[u_+(1) - u_-(1) \right] + L(0)} \right\} . \tag{42b}$$

Expressions in the same form for the off-resonance case $(\Delta_2/\gamma_{20}) > (1+I/2)^{1/2}$ were previously discussed in I, where it was shown that J_{21} represents the double-quantum transition rate per atom, in which atoms produced in level 2 subsequently decay from level 1 by the net exchange of two photons with the applied radiation fields, one absorbed at Ω_2 and one emitted at Ω_1. J_{01} was introduced as the single-quantum transition rate per atom, due to atoms produced in level 0 which subsequently decay from level 1, emitting a single photon at Ω_1. In this paper, however, we find it more convenient to express our results for $\Delta I(\Omega_1)$ in terms of n_0-n_2 and n_0-n_1. We thus have, equivalent to Eq. (41),

$$\Delta I(\Omega_1) = \hbar\,\Omega_1 \left[\langle R_{02} \rangle + \langle R_{01} \rangle \right] , \tag{43a}$$

where

$$R_{02} = -2n_{02} |\alpha|^2 \ell\, \mathrm{Im} \left\{ \frac{a_0 + a_0^* + \sum_{j=1}^{\infty} (1)^j \left[t_+(j)\, u_+(j) + t_-(j) u_-(j) \right]}{\frac{i\beta_o}{2} \left[u_+(1) - u_-(1) \right] + L(0)} \right\} , \tag{43b}$$

$$R_{01} = -2n_{01} |\alpha|^2 \mathrm{Im} \left\{ \frac{1}{\frac{i\beta_o}{2} \left[u_+(1) - u_-(1) \right] + L(0)} \right\} . \tag{43c}$$

In Figs. 5 through 8, $\langle R_{02} \rangle$ and $\langle R_{01} \rangle$ are plotted for various parameters. For convenience we have introduced the usual saturation parameter

$$I = \frac{2\beta_o^2}{\gamma_0 \gamma_2} , \tag{44}$$

as a measure of the intensity of the standing wave field (E_2). In Figs. 5, 7a and 7b the standing wave field is on resonance ($\Delta_2/\gamma_{02}=0$). In Figs. 6, 7c and 7d the standing wave field is off resonance $[\Delta_2/\gamma_{02} >> (1+I/2)^{1/2}]$. In Figs. 8a and 8b the standing wave field is near resonance $[\Delta_2/\gamma_{02} \approx (1+I/2)^{1/2}]$.

Briefly, the general behavior of the curves is as follows: $\langle R_{02} \rangle$ curves: When the laser is detuned a pair of resonances, one broad, one narrow, but of equal area, occurs symmetrically located about ω_1. In the folded configuration discussed here (Fig. 1a) the narrow resonance and the laser are always detuned to the same side of their respective Doppler profiles. (In a cascade configuration the narrow and broad resonances would be interchanged [Ref. I]). In the special case $k_2 > k_1$ the narrow resonance splits into two for intense laser fields. As the laser is tuned to line center the resonances overlaps and additional complex structure develops.

$\langle R_{01} \rangle$ curves (background): The background is unaffected by the laser when detuned, except in the case $k_2 > k_1$, in which structure develops on the same side of the Doppler profile as the narrow resonance in the $\langle R_{02} \rangle$ curves. (In no case does structure occur on the opposite side of the Doppler profile.) As the laser is tuned to line center structure emerges for strong laser fields. In all cases, the area under the background curve is unchanged by the presence of the laser field.

The additional features occurring on resonance are due to the standing wave nature of the intense field, whose traveling wave components simultaneously interact with atoms moving in the same narrow range of velocities. It will be shown below that off resonance, where the traveling wave components of E_2 no longer couple to the same atomic velocity band, that the line shape can be analyzed in terms of the two oppositely directed traveling waves at Ω_2 which do not couple to one another.

Intense Standing Wave Field - On Resonance [$\Delta_2=0$]

Typical results obtained from Eq. (43) are shown in Figs. 5a-5f. To understand the significance of these results and how they differ from the curves produced by an intense traveling wave field, consider the case $k_1=k_2$. For the traveling wave case broad ($E_1||E_2$) or narrow (E_1 anti-$||E_2$) resonances are produced in the $\langle R_{02}\rangle$ curves, depending on the relative directions of the two fields. No additional features occur as the traveling wave laser field is tuned through resonance. In the standing wave case the broad and narrow resonances occur simultaneously on opposite sides of the ω_1 gain profile when the laser is detuned. When the laser approaches line center, these resonances overlap. The resulting curve is not simply a superposition of broad and narrow signals. Complicated structure occurs. This structure results from the fact that the induced polarizations at Ω_1 associated with each of these resonances, being coherent with one another, interfere by means of spatial variations induced in both the population distribution [ρ^u_{00} Eq. (16e)] and the parametric driving terms at $\Omega_2-\Omega_1$ [produced by ρ^u_{20}, Eq. (16a)], causing complex line structure to develop [compare Eqs. (21a,b) and (27a, b)].

On resonance the standing wave background curves also exhibit complex structure resulting from coupling of the spatial variations in the polarization at Ω_1 directly through ρ'_{21}, which drives the system parametrically at $\Omega_2-\Omega_1$. Note that the characteristic behavior of the background term is distinct from that of the $\langle R_{02}\rangle$ term, occurring even when there is complete transparency at the laser transition ($n_2=n_0$). It is also interesting to note

that the area under the background curves remains unaffected by the laser field in all cases, consequence of the fact that the area of the response of each atomic velocity ensemble is unaltered by the laser field. A comprehensive discussion of this fact will be presented in a forthcoming publication.

It is worthwhile to reexamine the above line shape features from another point of view. In Refs. 20 and 21 it was shown that when an intense standing wave field is tuned to the center of the Doppler profile of a two level system, fine structure occurs in the spatially averaged population distribution. An example is shown in Fig. 3a. This structure results from the coherent ringing of slow atoms moving through the spatial nodes of the standing wave field (See Ref. 21, Sec. 7 for detailed discussion.) This curve is compared with a typical $\langle R_{20} \rangle$ curve in Fig. 3a. The influence of the velocity deformations in the spatially averaged population are clearly evident on the wings of the central dip in $\langle R_{02} \rangle$. No such fine structure appears in the central tuning dip of the two level gain profile (or the Lamb Dip), obtained by tuning the intense field through the center of the atomic resonance. Thus experimental observation of curves such as $\langle R_{02} \rangle$ of Fig. 3b would not only confirm the present results but would also provide evidence of the population structure predicted in Refs. 20 and 21.

Indeed, a major incentive of this work has been to determine the extent to which the structure in the population distribution would manifest itself in the radiation at the coupled transition.

This behavior was anticipated on the basis of a simple argument ignoring field interactions between E_1 and E_2 [Independent Field

Approximation (IFA)]. In this limit the spontaneous emission at Ω_1 is given by

$$\Delta I(\Omega_1)_{IFA} = h\Omega_1\gamma_{10}\frac{k_1}{\pi}\left\langle \frac{\gamma_{10}(n_0+n_{02}[a_0+a_0^*])}{(\Delta_1-k_1v)^2+\gamma_{10}^2} \right\rangle , \qquad (45)$$

where $n_0+n_{02}(a_0+a_0^*)$ is the spatially uniform component of $\rho_{00}^u(v)$, Eq. (16e), in the presence of the standing-wave laser field. One would expect the fine structure to wash out for $\gamma_{10} >> \gamma_{20}$ since in this case the broad Lorentzian cannot follow the narrow structure within the population curve (whose fine structure is of the order of γ_{20}). However, with $\gamma_{10} \lesssim \gamma_{20}$ fine structure would occur. Needless to say the IFA expression is not rigorous. For purposes of comparison the IFA results are plotted together with the exact expression for $\langle R_{02} \rangle$ [Eq. (43b)] and the corresponding rate equation approximation (REA), discussed below, in Fig. 9.

For the case $k_1 \neq k_2$ additional line shape features develop. These features are also observed when the laser is detuned from resonance, where they can be separated from the standing wave interactions discussed above. We defer discussion of these traveling-wave effects to the next sub-section, where algebraic expressions for $\langle R_{02} \rangle$ and $\langle R_{01} \rangle$, valid for a detuned standing-wave laser field of arbitrary intensity, are presented.

Intense Standing-Wave Field-Off Resonance [$\Delta_2/\gamma_{20} >> (1+I/2)^{1/2}$]

Next consider the case when the laser field is off resonance (Figs. 6, 7c and 7d). In this limit R_{02} and R_{01} reduce to

$$R_{02}=-(1/2)n_{02}\beta_o|\alpha|^2\ell \quad x$$

$$\mathrm{Im}\left\{\frac{\frac{y_1^{REA}}{L(1)}\left[\frac{\Delta_2}{\gamma_{02}+ik_2v}+\frac{[L(1)+i\gamma_0]}{\gamma_0}\right]+\frac{y_1^{*REA}}{L(-1)}\left[\frac{\Delta_2}{\gamma_{02}-ik_2v}+\frac{[L(-1)+i\gamma_0]}{\gamma_0}\right]}{\frac{-\beta_o^2}{4}\left[\frac{1}{L(1)}+\frac{1}{L(-1)}\right]+L(0)}\right\}, \tag{46a}$$

$$R_{01}=-2n_{01}|\alpha|^2\ell\,\mathrm{Im}\left\{\frac{1}{\frac{-\beta_o^2}{4}\left[\frac{1}{L(1)}+\frac{1}{L(-1)}\right]+L(0)}\right\}, \tag{46b}$$

Where y_1^{REA} is given in Table I, Eq. (T21).

These results are equivalent to the Rate Equation Approximation (REA), in which the spatial harmonics induced by the standing-wave field are neglected. (See Appendix A and Table I.) Since we are restricting our considerations here to the detuned case, Eqs. (46) further simplify to

$$R_{02}=R_{02}(+)+R_{02}(-) \tag{47a}$$

$$R_{01}=R_{01}^{o}+R_{01}(+)+R_{01}(-), \tag{47b}$$

with

$$R_{02}(\pm)=2n_{02}|\alpha|^2\beta_o\ell\ \mathrm{Re}\left\{\frac{\frac{1}{i\gamma_0}\mathrm{Re}\left(\frac{1}{F_\pm}\right)-\frac{1}{2L(\pm 1)F_\pm}}{\left[1+\frac{2\beta_o}{\gamma}\mathrm{Re}\left(\frac{1}{F_\pm}\right)\right]\left[L(0)-\frac{\beta_o^2/4}{L(\pm 1)}\right]}\right\}, \tag{48a}$$

where

$$\frac{1}{F_\pm}=\frac{\beta_o}{2}\left\{\frac{1}{\gamma_{20}+i(\Delta_2\pm k_2 v)}\right\}, \tag{48b}$$

and

$$R_{01}(\pm)=-(1/2)n_{01}|\alpha|^2\beta_o^2\ell\,\mathrm{Im}\left\{\frac{1}{L(0)\left[L(0)L(\pm 1)-\frac{\beta_o^2}{4}\right]}\right\}, \tag{49a}$$

$$R_{01}^{o}=-2n_{01}|\alpha|^2\ell\,\mathrm{Im}\left[\frac{1}{L(0)}\right]. \tag{49b}$$

The terms naturally break into pairs (+ and -) as a consequence of the fact that when the standing-wave laser field is detuned from resonance the oppositely directed traveling-wave components of E_2 couple to distinct bands of atoms moving with opposite velocities. In fact, the (+)[(-)] refers to the component of E_2 anti-parallel[parallel] to E_1. Note that R_{01}^{o} represents the usual background term in the absence of E_2. These results were previously obtained in I, where the intense field was assumed to be in the form of a travelling wave. In the Doppler broadened limit the velocity integration of Eqs. (48) and (49) may be carried out analytically.[29] The results for the two cases $k_1 > k_2$ and $k_1 < k_2$ differ qualitatively.

Case 1: $k_1 \geq k_2$

In this case we find that

$$\langle R_{01}^{o} \rangle = R^{o} W_{01}(\Delta_1/k_1), \tag{50a}$$

$$\langle R_{01}(\pm) \rangle = 0, \tag{50b}$$

$$\langle R_{02}(\pm) \rangle = -R^{o} \frac{n_{02}(0)}{n_{01}(0)} W_{02}(\Delta_1/k_1) \left\{ \frac{k_1 \beta_o^2}{2k_2 \gamma_0 Q} \operatorname{Im}\left[\frac{1}{\Omega_{\pm} - i\Gamma_{\pm}/2} \right] \right\}, \tag{50c}$$

where

$$n_{ij}(\Delta_1/k_1) = N_i G_i(\Delta_1/k_1) - N_j G_j(\Delta_1/k_1), \tag{51a}$$

$$W_{ij}(\Delta_1/k_1) = \frac{n_{ij}(\Delta_1/k_1)}{n_{ij}(0)}, \tag{51b}$$

$$R^{o} = \frac{2\pi}{k_1} |\alpha|^2 \ell n_{01}(0), \tag{51c}$$

$$Q = \left[1 + \frac{4\beta_o^2}{\gamma_0 \gamma_2} \right]^{1/2}, \tag{51d}$$

$$\Omega_{\pm} = \Delta_1 \pm (k_1/k_2)\Delta_2 \tag{51e}$$

$$\Gamma_{\pm} = \gamma_1 + \gamma_{\pm} Q , \tag{51f}$$

and

$$\gamma_{\pm} = \frac{k_1}{k_2} \gamma_2 + \frac{|k_2 \pm k_1|}{k_2} \gamma_0 . \tag{51g}$$

Equations (50), valid for large values of E_2, were first given in I. Curves of $\langle R_{01} \rangle$ and $\langle R_{02} \rangle$ for the detuned case with $k_1 \geq k_2$ are plotted from Eqs. (43 b, c) in Figs. 6a,b,e,f,7c and 7d. It is found that the results agree with the analytical expressions, Eqs. (50). The $\langle R_{02} \rangle$ curves exhibit a pair of Lorentzian resonances of equal area at $\Omega_{\pm} = 0$, of widths $\Gamma_{\pm}$ as in Eq. (50c). Note that $\Gamma_{\pm}$ are significantly power broadened for intense laser fields ($Q \gg 1$), as in Eq. (51f). The + and - resonances correspond to the interaction of E_1 with that component of E_2 anti-parallel and parallel to E_1, respectively. The $\langle R_{01} \rangle$ curve exhibits no structure, in accord with Eq. (50b), and is identical to the background one would observe if E_2 were absent.

Case 2: $k_1 < k_2$

In this case we find that

$$\langle R_{01} \rangle = \langle R_{01}^{o} + R_{01}(-) \rangle = -R^{o} W_{01}(\Delta_1/k_1)\, \mathrm{Im}\left(\frac{T}{Y}\right), \tag{52a}$$

$$\langle R_{01}(+) \rangle = 0 \quad , \tag{52b}$$

$$\langle R_{02}(+) \rangle = \text{same as for } k_1 \geq k_2 \text{ , Eq. (50c)}, \tag{52c}$$

$$\langle R_{02}(-) \rangle = -R^{o} \frac{n_{02}(0)}{n_{01}(0)} W_{02}(\Delta_1/k_1)\, \frac{B_o^2}{2Q} \left(\frac{k_1}{k_2}\right)^2 x$$

$$\mathrm{Im}\left\{ Y^{-1} \left(\frac{1}{B_+} \left[\frac{1+Q}{2} + i\, \frac{k_1 - k_2}{\gamma_0 k_1} (A_+ + \delta) \right] \right.\right.$$

$$\left.\left. + \frac{1}{B_-} \left[\frac{1-Q}{2} + i\, \frac{k_1 - k_2}{\gamma_0 k_1} (A_- + \delta) \right] \right) \right\}, \tag{52d}$$

where

$$S^2 = \frac{k_1}{k_2} \left(\frac{k_2 - k_1}{k_2} \right) \beta_o^2 \quad , \tag{53a}$$

$$T = \Omega_- + \frac{1}{2} i \left(\gamma_- + \gamma_1 \right), \tag{53b}$$

$$Y = + \left[S^2 - T^2 \right]^{1/2} \quad , \tag{53c}$$

$$A_{\pm} = \frac{-k_2}{2(k_2 - k_1)} (T \pm iY) + (\Delta_1 + i\gamma_{01}) \, , \tag{53d}$$

$$B_{\pm} = \pm A_{\pm} + \frac{k_1}{k_2}\left(i\gamma_{20}Q \mp \Delta_2\right), \tag{53e}$$

$$\delta = \frac{-k_1}{k_2 - k_1}\left(\Delta_{21} - i\gamma_{21}\right) . \tag{53f}$$

As an example, curves of $\langle R_{02} \rangle$ and $\langle R_{01} \rangle$ for the case $k_1 = k_2/2$ are plotted from Eqs. (43b,c) in Figs.6c,d and 7c,d. The results agree with curves plotted for the analytic expressions, Eq. (52), and differ significantly from those for the case $k_1 \geq k_2$: The $\langle R_{02} \rangle$ curves still exhibit a Lorentzian resonance at $\Omega_+ = 0$ of width Γ_+ corresponding to the interaction of E_1 with the anti-parallel component of E_2 , just as for the case $k_1 \geq k_2$. However, the resonance at $\Omega_- = 0$, corresponding to the interaction of E_1 with the parallel component of E_2 , exhibits a splitting which increases with increasing field strength E_2 and vanishes in the limit of weakly saturating fields, where the resonance reduces to a Lorentzian of width Γ_- (see following paragraph). In addition to the features in $\langle R_{02} \rangle$, structure in $\langle R_{01} \rangle$ also manifests itself. We see that a distinctly non-Lorentzian resonance appears at $\Omega_- = 0$. This resonance features a central dip and broad wings peaking off center, in such a manner as to leave the area of the $\langle R_{01} \rangle$ background curve unaltered by the presence of E_2 . The resonance is a result of the interaction of E_1 with that component of E_2 parallel to E_1 , and as such is a travelling wave effect. This effect, which occurs even for weakly saturating values of E_2 , has recently been observed in Ref. 9. The splitting of the $\langle R_{02} \rangle$ resonance, which appears only for a strongly saturating value of E_2 , is a new effect and has not yet been observed.

Intense Standing-Wave Field--Near Resonance $\left[\Delta_2/\gamma_{20} \simeq (1 + I/2)^{1/2}\right]$

In the near resonance case interference effects produce additional lineshape alterations. Examples, plotted from Eqs. (43b,c), are given in Figs. 8a,b. Note that these curves combine features of the off-resonance and on-resonance cases, leading to complex asymmetric lineshapes.

Limit of Weakly Saturating Laser Field (Q≈1)

The results for the case of weakly saturating laser are plotted in Fig. 7. The analytical expressions for the case $k_1 \geq k_2$ are the same in Eqs. (50) but with Q= 1, indicating that the Lorentzian resonances of different width but of equal area occur in $\langle R_{02} \rangle$ even in this limit. It follows from Eqs. (43b) and (43c) that in the weak saturation limit Eqs. (50) are valid even when the laser is tuned to the line center.

In this limit it follows from Eqs. (52) that the analytical results for the case $k_1 < k_2$ are identical to the results for $k_1 \geq k_2$ with the exception of $\langle R_{01}(-) \rangle$, which is given by[23-25]

$$\langle R_{01}(-) \rangle = R^{o} W_{01} (\Delta_1/k_1) \beta_o^2 \left(\frac{k_1}{k_2}\right)^2 \frac{k_2 - k_1}{2k_2} \mathrm{Re}\left[\frac{1}{\Omega_- + i\left(\frac{\gamma_- + \gamma_1}{2}\right)}\right]^2 , \quad k_2 > k_1. \tag{54}$$

Therefore, even for a weakly saturating laser field structure appears on the background lineshape when $k_2 > k_1$, although the area under $\langle R_{01} \rangle$ remains independent of E_2 . No such structure appears when $k_1 > k_2$. Note also that the splitting of the narrow resonance of the $\langle R_{02} \rangle$ curves, which occurs at intense laser fields for $k_2 > k_1$, disappears in this limit. All these remarks are contingent upon the assumption that the Doppler widths are much greater than the natural widths.

Computer plots of Eq. (43) for I= 0.1 are given in Figs. 7c,d for the off-resonance case and Figs. 7a,b for the on-resonance case. Note that the latter curves are just the superposition at $\Delta_1 = 0$ of the detuned resonances, indicating that spatial interference effects between components of the induced polarization at Ω_1 are not significant here.

V. Equal Area Property

Some interesting properties of the laser induced change signals emerge from the results presented here. First, as stated above, the area under the $\langle R_{01} \rangle$ background is always independent of E_2. Secondly, the area under the $\langle R_{02} \rangle$ lineshape is independent of the field interactions between E_1 and E_2. From this consideration it follows that when the laser is detuned the broad and narrow resonances are always equal in area, even when the narrow resonance splits in two. In fact, it may be shown that in each case the area under the exact lineshape curve [Eq. (43a)] is identically equal to that under the corresponding IFA curve [Eq. (45)]. This property is a manifestation of the fact, first pointed out by Javan[30], that the area under the response of each individual atomic velocity ensemble is equal to that obtained from the corresponding IFA, even though the actual frequency behavior differs significantly. These results can be shown to follow from an elementary quantum mechanical analysis of the transition rates of three level systems coupled to applied fields. A detailed discussion will be deferred to a later publication.

Acknowledgement

This work has benefitted from discussions with Professor Ali Javan and his support of the research.

Appendix A: Solution to the Nonhomogeneous Linear Difference Equations (33)

Consider the coupled nonhomogeneous linear difference equations, Eqs. (33) of the text, which may be written in the form

$$x_{\pm}(n+1) - x_{\pm}(n-1) + A_{\pm}(n)\, x_{\pm}(n) = \phi_{\pm}(n), \quad n \geq 1 \tag{A1a}$$

$$x_{+}(1) - x_{-}(1) + A(0)x(0) = \phi(0) \tag{A1b}$$

$$x_{+}(0) = x_{-}(0) \equiv x(0), \tag{A1c}$$

where

$$A\pm(n) = \frac{2}{i\beta_0} L(\pm n) , \tag{A2a}$$

$$\phi_{\pm}(n) = \frac{\pm 2n_{02}}{i\beta_0} t_{\pm}(n) , \tag{A2b}$$

$$A(0) = \frac{2}{i\beta_0} L(0) , \tag{A2c}$$

and

$$\phi(0) = \frac{2}{i\beta_0} t(0) . \tag{A2d}$$

Note that adjacent $x_{\pm}(n)$'s are coupled together in three's. The $\phi_{\pm}(n)$'s are prescribed driving terms. Equations (A1b) and (A1c) serve to join the $x_{+}(n)$ with the $x_{-}(n)$. Henceforth, the $\pm$ subscripts will be deleted when convenient.

The solution to Eqs. (A1) may be formed from the solutions to the associated homogeneous equations, $x^H(n)$. The homogeneous equations are obtained by setting the $\phi(n) = 0$:

$$x^H(n+1) - x^H(n-1) + A(n)\, x^H(n) = 0, \quad n \geq 1 \quad . \tag{A3}$$

Solutions to equations of the type Eq. (A3) are discussed in detail in Section 5 of Ref. 21. A brief account is given here in Appendix B, where it is shown that the most general solution for $x^H(n)$ may be written in the form

$$x^H(n) = Cu(n) + Dv(n), \tag{A4}$$

where $u(n)$ and $v(n)$ separately satisfy Eq. (A3), and C and D are arbitrary constants independent of n. The $u(n)$'s and $v(n)$'s are distinct classes of solutions characterized by their behavior at large n. The $u(n)$'s, which we call B-type solutions, have the limiting behavior

$$u(n) \sim \frac{1}{n!}\left(\frac{\beta_o}{2ik_2v}\right)^n \quad , \ n \text{ large.} \tag{A5a}$$

The $v(n)$'s, called N-type solutions, have the limiting behavior

$$v(n) \sim (n-1)!\left(\frac{2k_2v}{i\beta_o}\right)^n, \ n \text{ large.} \tag{A5b}$$

Accordingly, in the limit $n \to \infty$, $u(n)$ vanishes whereas $v(n)$ diverges. In subsequent discussions it will be convenient to normalize $u(n)$ and $v(n)$ such that

$$u(0) = v(0) = 1. \tag{A6}$$

Solutions to the nonhomogeneous equations, Eq. (A1a), may be constructed using the method of variation of parameters.[31] Let us assume $x(n)$ to be of the form

$$x(n) = C(n)\, u(n) + D(n)\, v(n), \quad n \geq 0. \tag{A7}$$

Inserting Eq. (A7) into Eq. (A1), and eliminating terms containing $A(n)$ by means of Eq. (A3), one obtains, for $n \geq 1$,

$$\delta C(n)u(n+1) + \delta D(n)v(n+1) + \delta C(n-1)\, u(n-1) + \delta D(n-1)\, v(n-1) = \phi(n), \tag{A8}$$

with

$$\delta C(n) = C(n+1) - C(n), \tag{A9a}$$

$$\delta D(n) = D(n+1) - D(n). \tag{A9b}$$

Trial solution (A7) does not uniquely specify the $C(n)$'s and $D(n)$'s, and in Eq. (A8) we are free to choose

$$\delta C(n)\, u(n) + \delta D(n)\, v(n) = 0, \quad n \geq 0, \tag{A10}$$

whereupon for $n \geq 1$,

$$\delta C(n)\, u(n+1) + \delta D(n)\, v\,(n+1) = \phi(n). \tag{A11}$$

Combining Eqs. (A10) and (A11), we find

$$\left.\begin{aligned} \delta C(n) &= \frac{\phi(n)v(n)}{u(n+1)\ v\ (n)-u(n)\ v(n+1)} \qquad \text{(A12a)} \\ \delta D(n) &= \frac{-\phi(n)\ u(n)}{u(n+1)\ v(n)\ -\ u(n)\ v(n+1)} \qquad \text{(A12b)} \end{aligned}\right\} \quad n \geq 1.$$

These expressions may be simplified by means of the following identity, obtained from Eq. (A3):

$$\begin{aligned} u(n+1)v(n)-v(n+1)u(n) &= -[u(n)v(n-1)-v(n)u(n-1)] \qquad \text{(A13)} \\ &= (-1)^n\ [u(1)\ -\ v(1)]\ . \end{aligned}$$

(The last step follows by induction.) Thus,

$$\left.\begin{aligned} \delta C(n) &= \frac{(-1)^n\phi(n)v(n)}{u(1)\ -\ v(1)} \qquad \text{(A14a)} \\ \delta D(n) &= \frac{(-1)^n\phi(n)\ u(n)}{u(1)\ -\ v(1)} \qquad \text{(A14b)} \end{aligned}\right\} \quad n \geq 1\ .$$

Accordingly, for $n>1$,

$$C(n) = C(1) + \frac{1}{u(1)\ -\ v(1)} \sum_{j=1}^{n-1} (-1)^j \phi(j)\ v(j), \qquad \text{(A15a)}$$

$$D(n) = D(1) - \frac{1}{u(1)-v(1)} \sum_{j=1}^{n-1} (-1)^j \phi(j) u(j). \qquad \text{(A15b)}$$

An additional equation, obtainable from Eq. (A10) for n = 0, is

$$C(0) + D(0) = C(1) + D(1) \qquad \text{(A16)}$$

since, by Eq. (A6),

$$u(0) = v(0) = 1. \qquad \text{(A17)}$$

Therefore, using Eq. (A6), we can write down the sequence

$$x(0) = C(1)+D(1), \qquad \text{(A18a)}$$

$$x(1) = C(1)u(1)+D(1)v(1), \qquad \text{(A18b)}$$

$$x(n) = \left\{C(1) + \frac{1}{u(1)-v(1)} \sum_{j=1}^{n-1} (-1)^j \phi(j) v(j)\right\} u(n) + \left\{D(1) - \frac{1}{u(1)-v(1)} \sum_{j=1}^{n-1} (-1)^j \phi(j) u(j)\right\} v(n), \; n \geq 1. \qquad \text{(A18c)}$$

Thus the x(n) may be expressed in terms of two quantities independent of n, C(1) and D(1), as of yet undetermined.

The value of D(1) may be established by considering the behavior of x(n) as $n \to \infty$. Recall from Section II that the x(n)' s are the coefficients of Fourier expansions in $k_2 z$ for ρ'_{21} and ρ'_{01}. The latter quantity is essentially the induced polarization at Ω_1, consequently the emitted power, ΔI, may be expressed as a sum of x(n)' s (n even), [Eq. (30b)]. For all physically possible (i.e. finite) values of $\phi(n)$ ΔI must remain finite, hence the x(n)' s may not diverge. [It was shown in Ref. 21 that the $\phi(n)$'s themselves strongly converge to 0 as $n \to \infty$. See also Table I.]

This requirement on x(n) places a restriction on the coefficient of v(n) in Eq.(A18c). Note first that in Eq.(A18c) both summation terms (including multiplication by u(n) or v(n), respectively) converge rapidly to zero for n large. Thus, since u(n) itself converges ~ 1/n! [Eq.(A5a)], the entire first bracketted term of Eq.(A18c) converges. But, as can be seen in Eq.(A5b), v(n) diverges ~ (n-1)!, placing a restriction on its coefficient. In fact, the required boundary condition can only be guaranteed by setting

$$D(1) = \frac{1}{u(1)-v(1)} \sum_{j=1}^{\infty} (-1)^j \phi(j)v(j) \ . \qquad \text{(A19)}$$

The remaining constant, C(1), may now be determined. Displaying the subscripts as in Eq. (A1), we have:

from Eq. (A1b),

$$x_+(1)-x_-(1)+A(0)\ x(0) = \phi(0), \qquad \text{(A20a)}$$

from Eq.(A17b),

$$x_+(1) = C_+(1)u_+(1)+D_+(1)v_+(1), \qquad \text{(A20b)}$$

$$x_-(1) = C_-(1)u_-(1)+D_-(1)v_-(1), \qquad \text{(A20c)}$$

and from Eqs.(A18a) and (A17),

$$x(0) = C_+(1)+D_+(1), \qquad \text{(A20d)}$$

$$x(0) = C_-(1)+D_-(1). \qquad \text{(A20e)}$$

These equations may be routinely combined to obtain

$$x(0) = \frac{\phi(0)+\sum_{j=1}^{\infty} (-1)^j\{\phi_+(j)u_+(j) - \phi_-(j)u_-(j)\}}{u_+(1) - u_-(1) + A(0)} \ . \qquad \text{(A21)}$$

Substitution of definitions (A2) gives the result of Eq. (37) of the text.

Rate Equation Approximation:

The Rate Equation Approximation (REA) for a two level system interacting with a standing wave field is that approximation in which spatial population variations arising from the interaction are neglected. In extending this approximation to a 3-level system we ignore contributions of the polarization arising from these terms (i.e. $x_n = 0$, $n > 1$). The difference equations [Eq. (A1 a-c)] considerably simplify and we have

$$x(0)+A_{\pm}(1)x_{\pm}(1) = \phi_{\pm}^{REA}(1), \tag{A22a}$$

$$x_{+}(1)-x_{-}(1)+A(0)x(0) = \phi \quad . \tag{A22b}$$

Solving these equations directly, we find

$$x^{REA}(0) = \frac{\phi^{REA}(0) + \frac{\phi_{-}^{REA}(1)}{A_{-}(1)} + \frac{\phi_{+}^{REA}(1)}{A_{+}(1)}}{A(0)+\frac{1}{A_{+}(1)}-\frac{1}{A_{-}(1)}}, \tag{A23}$$

where the $\phi^{REA}(n)$ are obtained from Eq. (A2) and Eq. (35), using the REA values, Table I, Eqs. (T20)-(T22).

Appendix B: Solution of the Second Order Linear Homogeneous Difference Equation (A3):

Consider Eq. (A3),

$$x^H_{\pm}(n+1)-x^H_{\pm}(n-1) + A_{\pm}(n)x_{\pm}(n)=0,\ n\geq 1, \tag{B1}$$

where

$$A_{\pm}(n) = \pm \frac{2}{i\beta_o} L(\pm n), \tag{B2}$$

$$L_{\pm}(n)=\begin{cases}\Delta_{12}-(k_1\pm nk_2)v+i\gamma_{21}, & n \text{ odd}\\ \Delta_1-(k_1\pm nk_2)v+i\gamma_{10}, & n \text{ even}\end{cases} \tag{B3}$$

In second order homogeneous difference equations, such as Eq.(B1), one may distinguish two classes of solutions, characterized by the behavior of $x^H(n)$ for large values of n.[21] In the present case the nature of these types of solutions is readily ascertained, noting that for large enough n (for $v\neq 0$),

$$L_{\pm}(n) \to \mp nk_2 v, \tag{B4}$$

so that

$$A_{\pm}(n) \to \frac{2ik_2 v}{\beta_o}\ n. \tag{B5}$$

To obtain the first class of solutions, assume that for large n

$$x^H_{\pm}(n+1) >> x^H_{\pm}(n-1). \tag{B6}$$

Then

$$\frac{x_{\pm}^{H}(n+1)}{x_{\pm}^{H}(n)} \sim \frac{2k_2 v}{i\beta_o} n, \tag{B7}$$

so that

$$x_{\pm}(n) \propto (n-1)!\left(\frac{2k_2 v}{i\beta_o}\right)^n . \tag{B8}$$

Note that $x_{\pm}(n) \to \infty$ for large n, in accord with initial assumption (B6). We denote solutions of this type by $v_{\pm}(n)$. Because of their close connection with Neumann functions we refer to solutions of the latter type as N-type solutions.[21]

The second class of solutions is obtained by assuming

$$x_{\pm}^{H}(n-1) >> x_{\pm}^{H}(n+1). \tag{B9}$$

Then

$$\frac{x_{\pm}^{H}(n)}{x_{\pm}^{H}(n-1)} \sim \left(\frac{\beta_o}{2ik_2 v}\right)\frac{1}{n}, \tag{B10}$$

so that

$$x_{\pm}(n) \propto \frac{1}{n!}\left(\frac{\beta_o}{2ik_2 v}\right)^n . \tag{B11}$$

Note that $x_{\pm}(n) \to 0$ for large n, in accord with initial assumption (B9). These convergent solutions are denoted by $u_{\pm}(n)$. Because of their close connection with Bessel functions we refer to solutions of this type as B-type solutions.[21]

To express $u_{\pm}(n)$ in a form convenient for computation we define the quantity

$$W_{\pm}(n) = \frac{u_{\pm}(n)}{u_{\pm}(n-1)} . \tag{B12}$$

Then from Eq. (B1) we obtain an expression for $W_{\pm}(n)$ in continued fraction form,

$$W_{\pm}(n) = \cfrac{\pm\, i\beta_o/2L[\pm n]}{1 - \cfrac{\beta_o^2/(4L[\pm n]L[\pm(n+1)])}{1 - \cfrac{\beta_o^2/(4L[\pm(n+1)]L[\pm(n+2)])}{1 \pm i\beta_o W_{\pm}(n+3)\,/\,2L[\pm(n+2)]}}} \qquad \text{(B13)}$$

Then

$$u_{\pm}(n) = \prod_{k=1}^{n} W_{\pm}(k)\ , \qquad \text{(B14)}$$

where we have set $u_{\pm}(0)=1$ without loss of generality.

Special Case $\gamma_2=\gamma_0$ and $\Delta_2=0$

For the case $\gamma_2=\gamma_0$ and $\Delta_2=0$, $u_{\pm}(n)$ may be written analytically in terms of $J_{\tau}(z)$, the Bessel function of real argument z and complex order τ:

$$u_{\pm}(n) = \frac{i^n J_{\tau(n)}(-\beta_o/k_2 v)}{J_{\tau(0)}(-\beta_o/k_2 v)}\ , \qquad \text{(B15)}$$

where

$$\tau(n) = \mp L(\pm n)/k_2 v. \qquad \text{(B16)}$$

As before, Eq. (B15) is normalized such that $u_{\pm}(0) = 1$. Equation (B15) follows from Eq. (B1) which, in this special case, reduces to the well-known recurrence relation for cylindrical functions.[21]

Appendix C: Algorithm for Computing Continued Fractions

Let

$$C = \cfrac{a_1}{1 + \cfrac{a_2}{1 + \cfrac{a_3}{1 + a_4}}} \quad . \qquad \text{(C1)}$$

Define

$$\frac{P_n}{Q_n} = \cfrac{a_1}{1 + \cfrac{a_2}{1 + \cfrac{a_3}{1 + a_4}}} \quad . \qquad \text{(C2)}$$

$$\cfrac{}{1 + a_n}$$

One can then show that P_n and Q_n obey the following difference equations:

$$P_n = P_{n-1} + a_n P_{n-2}, \qquad \text{(C3a)}$$

$$Q_n = Q_{n-1} + a_n Q_{n-2}, \qquad \text{(C3b)}$$

with

$$P_{-1} = 1, P_0 = 0 \qquad \text{(C3c)}$$

$$Q_{-1} = 0, Q_0 = 1. \qquad \text{(C3d)}$$

From the recurrence relations for P_n and Q_n one can readily

compute P_n and Q_n for any value of n. The computation is halted when

$$\left| \frac{(P_{n+1}/Q_{n+1}) - (P_n/Q_n)}{P_n/Q_n} \right| < 10^{-6}. \qquad \text{(C4)}$$

We then set

$$C = \frac{P_{n+1}}{Q_{n+1}} . \qquad \text{(C5)}$$

References

1. H.R. Schlossberg and A. Javan, Phys. Rev. 150, 267 (1966).

2. H.K. Holt, Phys. Rev. Letters 19, 1275 (1967).

3. T. Ya Popova, A. K. Popov, S. G. Rautian and R. I. Sokolovskii, Soviet Physics JETP 30, 466 (1970) [ZhETF 57, 850 (1969)] and erratum: Soviet Physics JETP 30, 1208 (1970) [ZhETF 57, 2254 (1970)].

4. M.S. Feld and A. Javan, Phys. Rev. 177, 540 (1969). This paper shall be referred to subsequently as I.

5. Th. Hansch and P. Toschek, Z. Physik 236, 213 (1970).

6. J.A. White and R. Bose, Bull. Am. Phys. Soc. 13, 172 (1968).

7. H.K. Holt, Phys. Rev. Letters 20, 410 (1968).

8. I.M. Beterov and V.P. Chebotaev, JETP Letters 9, 127 (1969) [ZhETF Pis. Rde. 9, 216 (1969)].

9. T. Hansch, R. Keil, A. Schabert, Ch. Schmelzer and P. Toschek, Z. Physik 226, 293 (1969); T. Hansch, Ph.D. Thesis, University of Heidelberg, Germany (1969) unpublished.

10. M.S. Feld, B.J. Feldman and A. Javan, Bull. Am. Phys. Soc. 12, 669 (1967); L.H. Domash, M.S. Feld, B.J. Feldman and A. Javan, to be published.

11. T. Ducas, M.S. Feld, L.W. Ryan, Jr., N. Skribanowitz and A. Javan, to be published.

12. R.H. Cordover, P.A. Bonczyk and A. Javan, Phys. Rev. Letters 18, 730 (1967).

13. M.S. Feld, Ph.D. Thesis, M.I.T., 1967 (unpublished). See also Ref. 10.

14. H.R. Schlossberg and A. Javan, Phys. Rev. Letters 17, 1242 (1966).

15. J.S. Levine, P.A. Bonczyk, and A. Javan, Phys. Rev. Letters 22, 267 (1969).

16. G.W. Flynn, M.S. Feld and B.J. Feldman, Bull. Am. Phys. Soc. 12, 669 (1967).

17. I.M. Beterov, Yu. A. Matyugin and V.P. Chebotaev, JETP Letters 10, 187 (1969) [ZhETF Pis. Red. 10, 296 (1969).

18. T. Hansch and P. Toschek, IEEE J. Quantum Electronics QE-4, 467 (1968).

19. W.G. Schweitzer, Jr., M.M. Birky and J.A. White, J. Opt. Soc. Am. 57, 1226 (1967).

20. S. Stenholm and W. E. Lamb, Jr., Phys. Rev. 181, 618 (1969).

21. B.J. Feldman and M.S. Feld, Phys. Rev. A1, 1375 (1970).

22. The explanation of the velocity fine structure is discussed in detail in Ref. 21.

23. T. Ya. Popova, A.K. Popov, S.G. Rautian and R.I. Sokolovskii, National Symposium on the Physics of Gas Lasers, Novosibirsk, U.S.S.R. June 1969; A.K. Popov, Soviet Physics JETP, 31, 870 (1970) [ZhETF 58, 1623 (1970)].

24. T. Hansch and P. Toschek, National Symposium on the Physics of Gas Lasers, Novosibirsk, U.S.S.R., June, 1969; see also Ref. 5.

25. M.S. Feld, National Symposium on the Physics of Gas Lasers, Novosibirsk, U.S.S.R., June, 1969.

26. See Appendix C3 of I.

27. See I, Section III-B for further discussion.

28. Narrower velocity distributions, both rectangular and Gaussian, were found to produce small variations in the lineshapes. See, for example, G.E. Notkin, S.G. Rautian and A.A. Feoktistov, Soviet Physics JETP, 25, 1112 (1967) [ZhETF 52, 1673 (1967)].

29. The integrations can be done by contour integration or by the method of partial fractions. See, for example, Appendix D of I.

30. A. Javan, Phys. Rev. 107, 1579 (1957).

31. F.B. Hildebrand, Finite Difference Equations and Simulations, (Prentice Hall, Englewood Cliffs, New Jersey, 1968).

Table I: Definition of Symbols Appearing in Equation (16)

$$\gamma_{20} = \frac{1}{2}(\gamma_0+\gamma_2) \qquad (T1)$$

$$\Delta_2 = \Omega_2 - \omega_2 \qquad (T2)$$

$$\beta = \frac{\mu_{02} E_2^o}{2\hbar} e^{-i\phi_2} \qquad (T3)$$

$$\beta_o = |\beta| \qquad (T4)$$

$$\bar{\gamma} = \gamma_0\gamma_2/\gamma_{20} \qquad (T5)$$

$$\Pi_n^+ = -\frac{1}{2}\left[1 - \frac{i\Delta_2}{\gamma_{20} + ink_2v}\right] \frac{\beta^*}{\beta_o} y_n \qquad (T6)$$

$$\Pi_n^- = \frac{1}{2}\left[1 - \frac{i\Delta_2}{\gamma_{20} - ink_2v}\right] \frac{\beta}{\beta_o} y_n^* \qquad (T7)$$

odd $n \geq 1$

$$a_n = \frac{1}{2}\left[\frac{\gamma_2 + ink_2v}{\gamma_{20} + ink_2v}\right] y_n \qquad (T8)$$

$$b_n = -\frac{1}{2}\left[\frac{\gamma_0 + ink_2v}{\gamma_{20} + ink_2v}\right] y_n \qquad (T9)$$

even $n \geq 2$

$$a_0 + a_0^* = \frac{\gamma_2}{2\gamma_{20}}[y_o - 1] \qquad (T10)$$

$$b_0 + b_0^* = \frac{-\gamma_0}{2\gamma_{20}}[y_0 - 1] \qquad (T11)$$

General Expression for y_n

$$y_0 = \frac{1}{1 + \frac{2\beta_o}{\bar{\gamma}} \mathrm{Re}\,(Z_0)} \qquad (T12)$$

$$y_{n+1} = -Z_n y_n, \quad n = 0, 1, 2 \ldots \qquad (T13)$$

$$Z_n = \cfrac{1}{F_{n+1} + \cfrac{1}{F_{n+2} + \cfrac{1}{F_{n+3} + \cdots}}} \qquad (T14)$$

with

$$\frac{1}{F_n} = \begin{cases} \frac{\beta_o}{2}\left[\frac{1}{\gamma_0+ink_2v} + \frac{1}{\gamma_2+ink_2v}\right] & n=0,2,4.... \\ \frac{\beta_o}{2}\left[\frac{1}{\gamma_{20}+i(nk_2v+\Delta_2)} + \frac{1}{\gamma_{20}+i(nk_2v-\Delta_2)}\right] & n=1,3,5,.... \end{cases} \quad (T15)$$

evaluated subject to the condition

$$\lim_{n\to\infty} Z_n = 0 \quad (T16)$$

Expression for y_n when $\gamma_0=\gamma_2\equiv\gamma, \Delta_2=0$

$$y_n = \frac{i^n J_{\nu(n)}(\eta)/J_{\nu(0)}(\eta)}{1 + \frac{2\beta_o}{\gamma} \mathrm{Im}\left[J_{\nu(1)}(\eta)/J_{\nu(0)}(\eta)\right]} \quad (T17)$$

$$\eta = \frac{2\beta_o}{k_2 v} \quad (T18)$$

$$\nu(n) = n - \frac{i\gamma}{k_2 v} \quad (T19)$$

with

$J_\nu(z)$ = Bessel function of order ν, argument z

Rate Equation Approximation to y_n

$$y_0^{REA} = \frac{1}{1 + \frac{2\beta_o}{\gamma} \mathrm{Re}\left(\frac{1}{F_1}\right)} \quad (T20)$$

$$y_1^{REA} = -y_o^{REA}/F_1 \quad (T21)$$

$$y_n^{REA} = 0, \quad n\geq 2 \quad (T22)$$

Figure Captions

Figure 1(a). Energy level scheme considered in this paper. Note that ω_1/ω_2 is variable and may be greater or less than unity.

Figure 1(b). Typical gain at Ω_1 for standing-wave field at Ω_2 detuned from resonance. The broad and narrow dips in the laser transition gain profile will be treated in a separate publication. The dips in the coupled transition are treated here. The insert depicts the dips as they occur in the absence of the background ($\langle R_{02} \rangle$ of the text). In the example shown, the background ($\langle R_{01} \rangle$) is unaltered by the standing wave field. In other cases both terms may be influenced by it.

Figure 2. Possible experimental arrangements for observing laser-induced line narrowing.

(a) Transmission - a tunable probe field $E_1(\Omega_1)$ is coaxial with standing wave laser field $E_2(\Omega_2)$. A filter blocks E_2. The output intensity of the probe field is monitored as a function of Ω_1.

(b) Spontaneous emission - the fluorescence spectrum $E_1(\Omega_1)$ emitted along the axis of the laser cavity is studied by means of a high resolution scanning Fabry-Perot inteferometer. The filter transmits only E_1.

The lineshape effects will be observed in both arrangements.

Figure 3(a). Plot of the spatially averaged population distribution vs. axial velocity for the upper level of a two-level system interacting with an intense standing wave field on reso-

nance. Note the fine structure appearing in the central dip over a narrow range of velocities about v=0.

(b). Typical curve of gain at Ω_1 as a function of Δ_1, the detuning from the atomic center frequency of the coupled transition for the same case as Figure 3(a). Comparison indicates that structure similar to the population fine structure occurs at the wings of the narrow central dip of the profile. The central dip itself originates from complex interference effects discussed in Section IV.

Figure 4. Gain at Ω_1, background omitted, for the case $\omega_1 \simeq \omega_2/2$ as influenced by an intense standing wave field E_2 detuned from resonance. Note that the dip on the right is split. For weakly saturating values of E_2, the splitting disappears. This new effect should not be confused with another effect which appears in the background term even for weakly saturating values of E_2 [see Figure 7(d)].

Figure 5. Intense standing-wave field on resonance ($\Delta_2=0$).

(a). $\langle R_{02} \rangle$ versus Δ_1 for $k_1=k_2$. The additional structure on the sides of the central dip emerges as I increases. The latter structure is closely correlated with the structure in the space-averaged population distribution (Figure 3a).

(b). $\langle R_{01} \rangle$ versus Δ_1 for the same conditions as in (a). Note that this structure would be present even if the medium were transparent ($n_2=n_0$).

(c). $\langle R_{02} \rangle$ versus Δ_1 for $k_1=k_2/2$. The splitting observed in the central dip also occurs when E_2 is off resonance [Figure 6(c)] and is a traveling wave effect.

(d). $\langle R_{01} \rangle$ versus Δ_1 for the same conditions as in (c). This structure also occurs in the detuned case [Figure 6(d)] and is a traveling wave effect.

(e). $\langle R_{02} \rangle$ versus Δ_1 for $k_1=2k_2$. The complex structure observed within the broad central dip is the result of interference effects due to the standing wave nature of E_2 and does not appear when E_2 is detuned [Figure 6(e)].

(f). $\langle R_{01} \rangle$ versus Δ_1 for the same conditions as in (e). The structure here is also the result of standing wave interference effects and does not appear when E_2 is detuned [Figure 6(f)].

Figure 6. Intense standing-wave field well detuned from resonance ($\Delta_2/\gamma_{02}=7.5k_2/k_1$).

(a). $\langle R_{02} \rangle$ versus Δ_1 for $k_1=k_2$. Two Lorentzian resonances occur at $\Omega_{\pm}=0$ of FWHM $\Gamma_{\pm}$, respectively, in accord with the analytic expressions Eq. (50c).

(b). $\langle R_{01} \rangle$ versus Δ_1 for same conditions as in (a). Note that E_2 has negligible effect on the background.

(c). $\langle R_{02} \rangle$ versus Δ_1 for $k_1=k_2/2$. A Lorentzian of width Γ_+ occurs at $\Omega_+=0$. The resonance at $\Omega_-=0$ splits into two, with increasing splitting for increasing values of I.

(d). $\langle R_{01} \rangle$ versus Δ_1 for the same conditions as (c). The background curve exhibits non-Lorentzian structure at $\Omega_-=0$. No structure appears at $\Omega_+=0$.

(e). $\langle R_{02} \rangle$ versus Δ_1 for $k_1=2k_2$. Lorentzian resonances of widths $\Gamma_{\pm}$ occur at $\Omega_{\pm}=0$.

(f). $\langle R_{01} \rangle$ versus Δ_1 for the same conditions as in (e). The flat curve indicates that E_2 has a negligible effect on

$\langle R_{01} \rangle$ when the standing wave field is detuned.

Figure 7. Weakly-saturating standing wave field.

(a). $\langle R_{02} \rangle$ versus Δ_1 for $\Delta_2=0$. In the weak field limit the resonances at $\Delta_1=0$ are essentially the sum of two Lorentzians of widths Γ_+ and Γ_-.

(b). $\langle R_{01} \rangle$ versus Δ_1 for $\Delta_2=0$. Note that for $k_1 \geq k_2$, the background curve is unaffected by E_2. However, for $k_1 < k_2$, a non-Lorentzian structure appears about $\Delta_1 \cong 0$.

(c). $\langle R_{02} \rangle$ versus Δ_1 for $\Delta_2=7.5k_2/k_1$. The two resonances at $\Omega_\pm=0$ are of widths $\Gamma_\pm$.

(d). $\langle R_{01} \rangle$ versus Δ_1 for $\Delta_2=7.5k_2/k_1$. These curves are the same as the background curves of (b) except that the non-Lorentzian resonance at $\Omega_-=0$ in the $k_1=k_2/2$ curve is shifted.

Figure 8. Plots of $\langle R_{02} \rangle$ (a) and $\langle R_{01} \rangle$ (b) versus Δ_1 for I=16, $k_1=k_2$, for the case in which E_2 is near resonance, $\Delta_2/\gamma_{02}=3.0$. These curves show features common to both the off-resonance and on-resonance conditions, indicating the complexity of the line-shape resulting from the interference effects treated in this paper.

Figure 9. Comparison of $\langle R_{02} \rangle$ versus Δ_1 for I=16, $k_1=k_2$ for the exact solution [Eq. 43(b)], the IFA [Eq. (45)] and the REA [Eq. (A23)]. Note that structure in the exact curve on the wings of the central dip coincides with the residual structure in the IFA arising because of the fine structure in the population distribution of level 2, although the structure in the exact curve is significantly enhanced. This enhancement results from spatial interference effects and does not appear in the REA curve. The

narrow central dip in the exact curve is in part due to the field interactions between E_1 and E_2 in the absence of spatial variations in the population of level 2, as can be seen by comparison with the central dip of the REA curve. The exact curve, however, is further influenced by spatial interference effects.

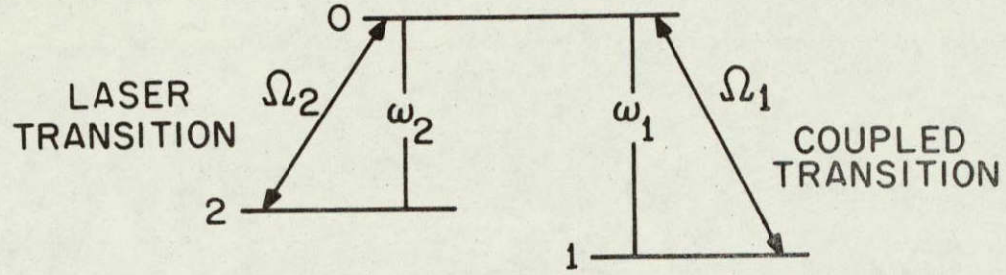

(a) Energy Level Diagram

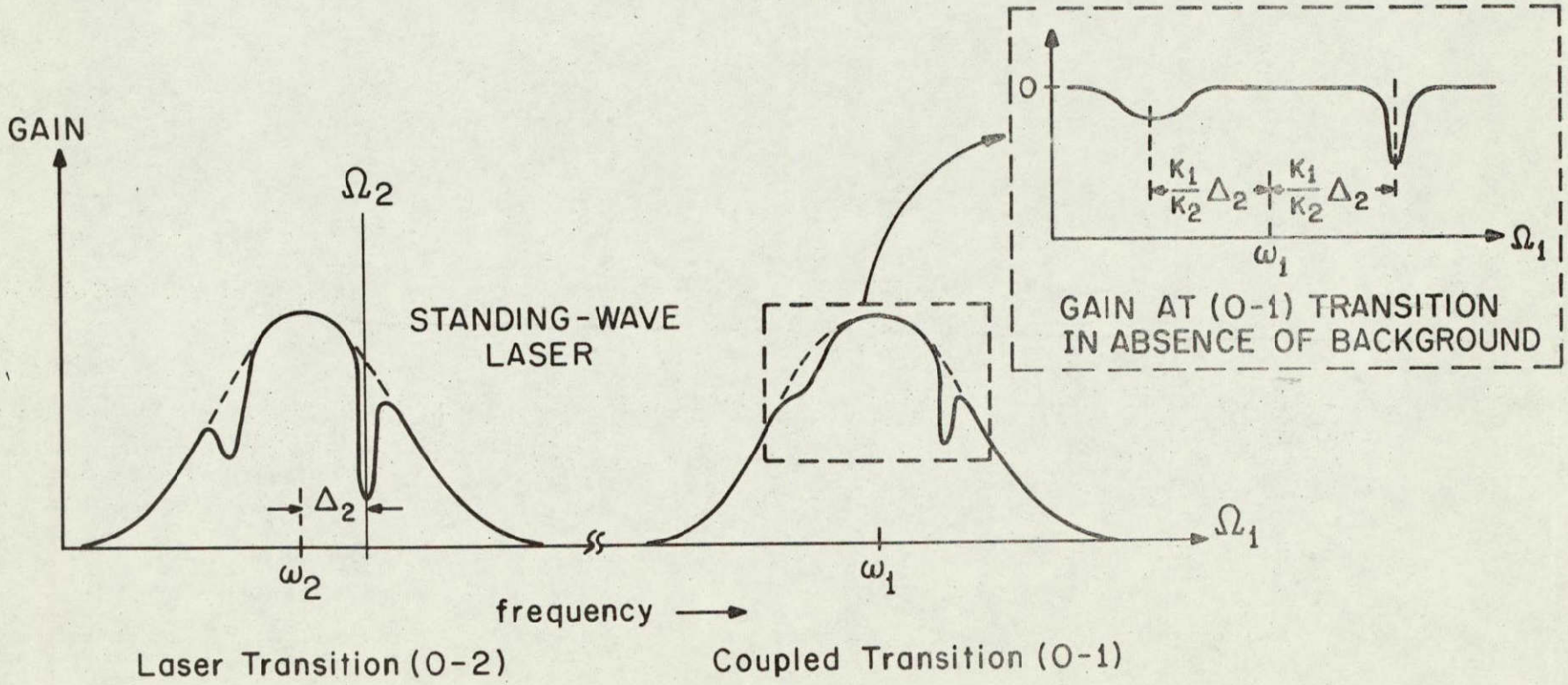

(b) Gain Profile

Fig. 1

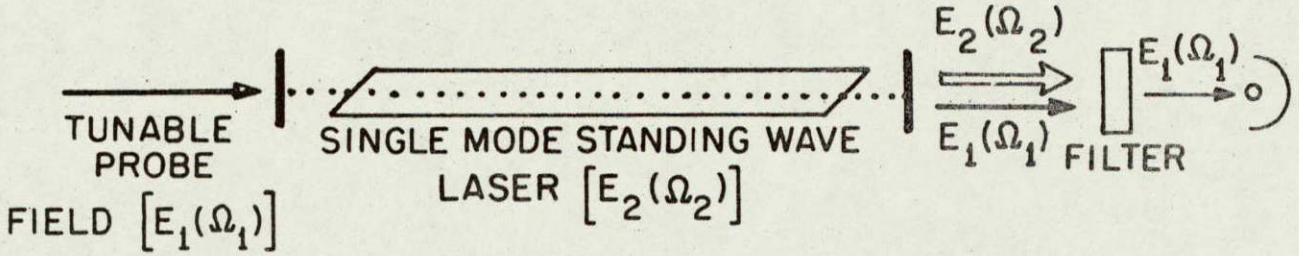

a) Experimental Arrangement – Transmission

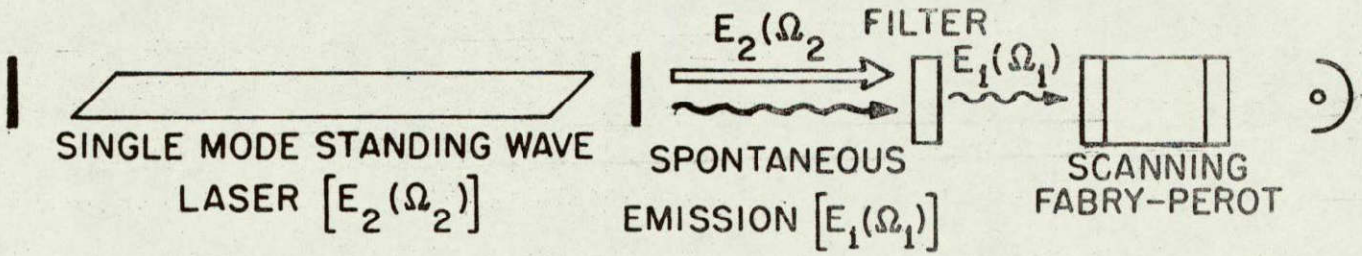

b) Experimental Arrangement - Spontaneous Emission

Fig. 2

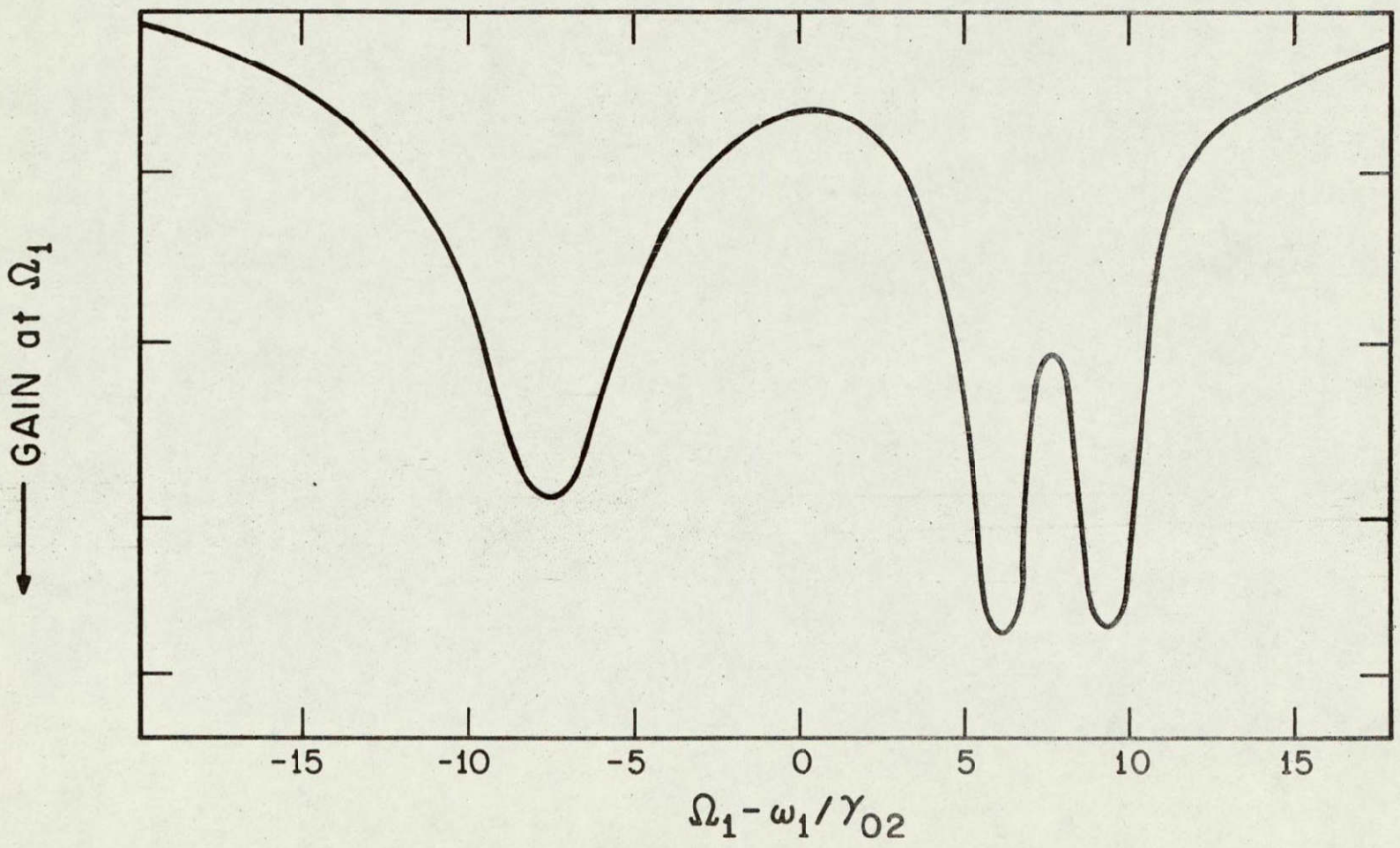

Fig. 4

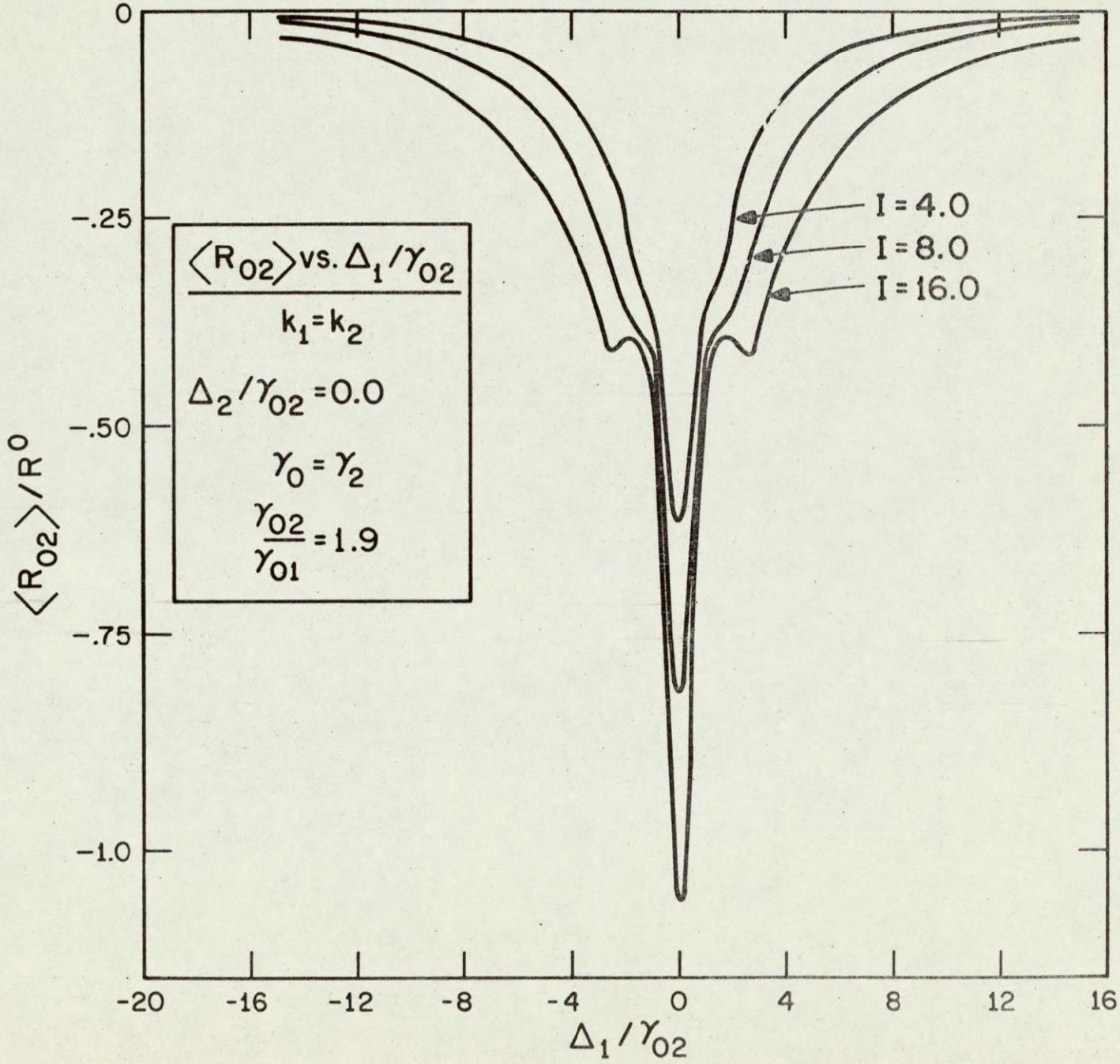
0
-.25
-.50
-.75
-1.0
$\langle R_{02} \rangle / R^0$
$\langle R_{02} \rangle$ vs. Δ_1/γ_{02}
$k_1 = k_2$
$\Delta_2/\gamma_{02} = 0.0$
$\gamma_0 = \gamma_2$
$\frac{\gamma_{02}}{\gamma_{01}} = 1.9$
I = 4.0
I = 8.0
I = 16.0
-20
-16
-12
-8
-4
0
4
8
12
16
Δ_1/γ_{02}

Fig. 5a

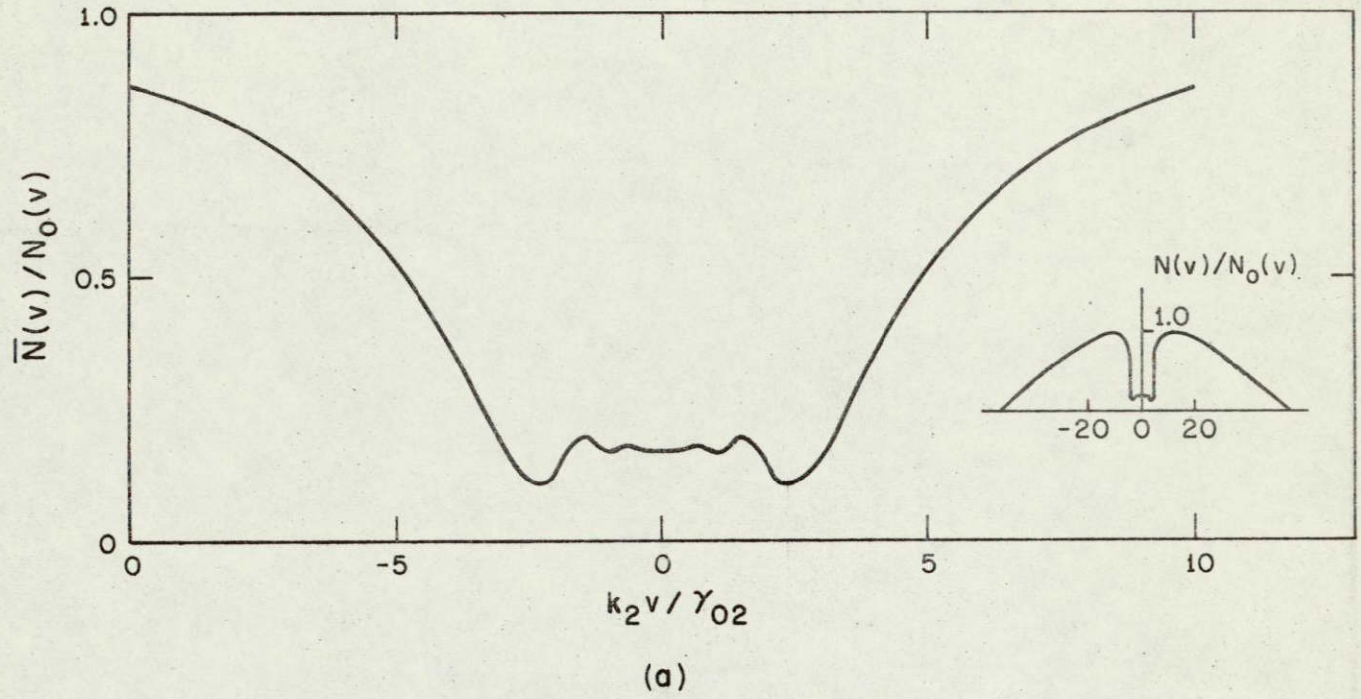
1.0
0.5
0
$\bar{N}(v)/N_0(v)$
0
-5
0
5
10
$k_2 v/\gamma_{02}$
$N(v)/N_0(v)$
1.0
-20
0
20

(a)

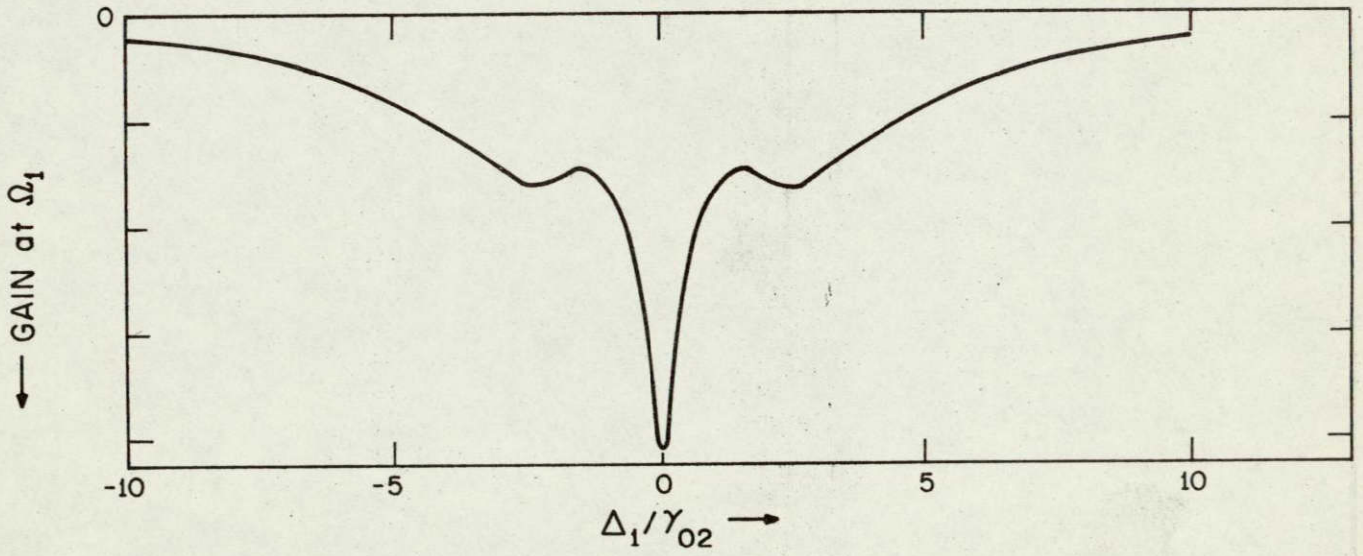
0
GAIN at Ω_1
-10
-5
0
5
10
Δ_1/γ_{02}

(b)

Fig. 3

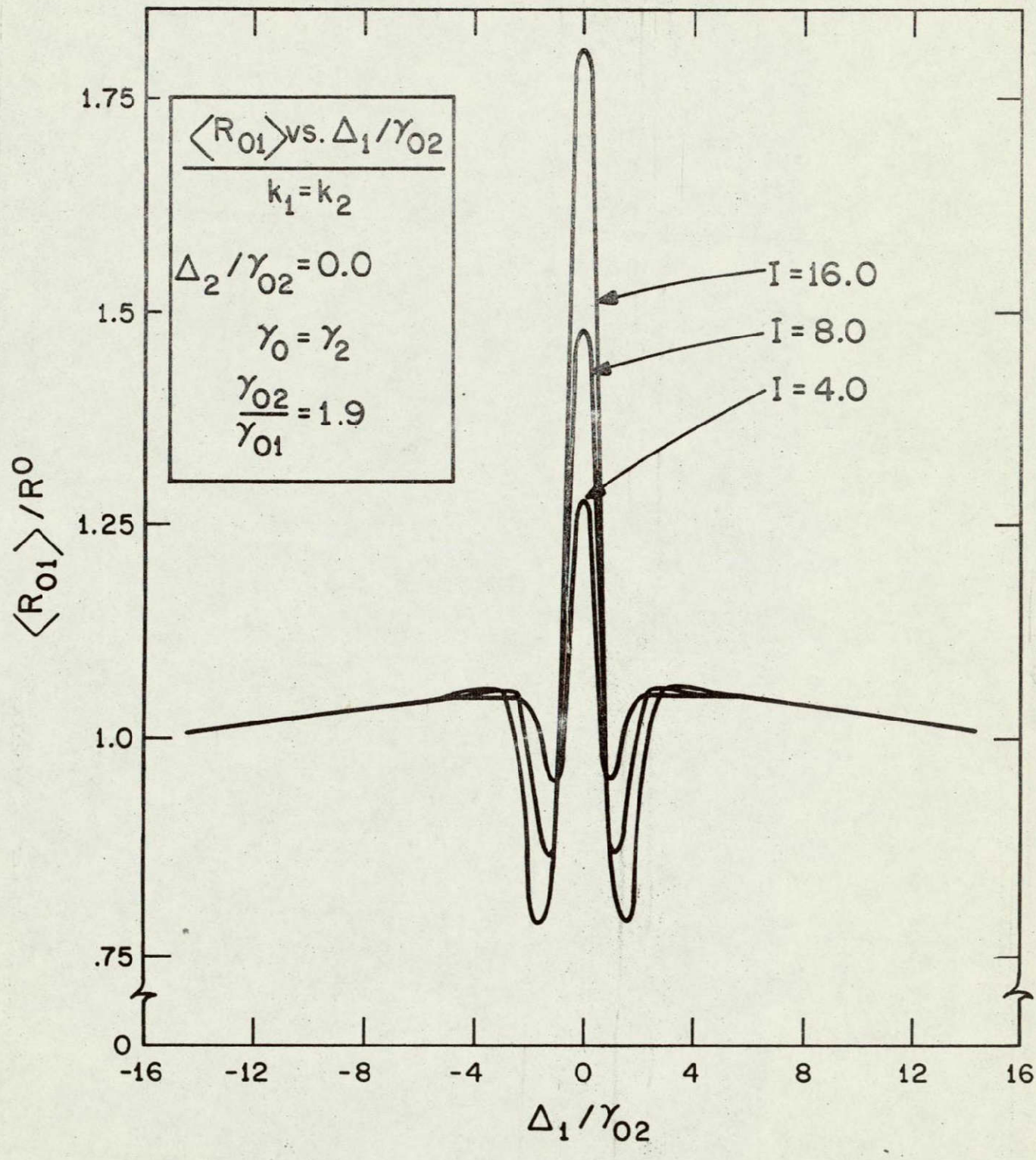
$\langle R_{01} \rangle$ vs. Δ_1/γ_{02}
$k_1 = k_2$
$\Delta_2/\gamma_{02} = 0.0$
$\gamma_0 = \gamma_2$
$\frac{\gamma_{02}}{\gamma_{01}} = 1.9$
I = 16.0
I = 8.0
I = 4.0
$\langle R_{01} \rangle / R^0$
1.75
1.5
1.25
1.0
.75
0
-16
-12
-8
-4
0
4
8
12
16
Δ_1/γ_{02}

Fig. 5b

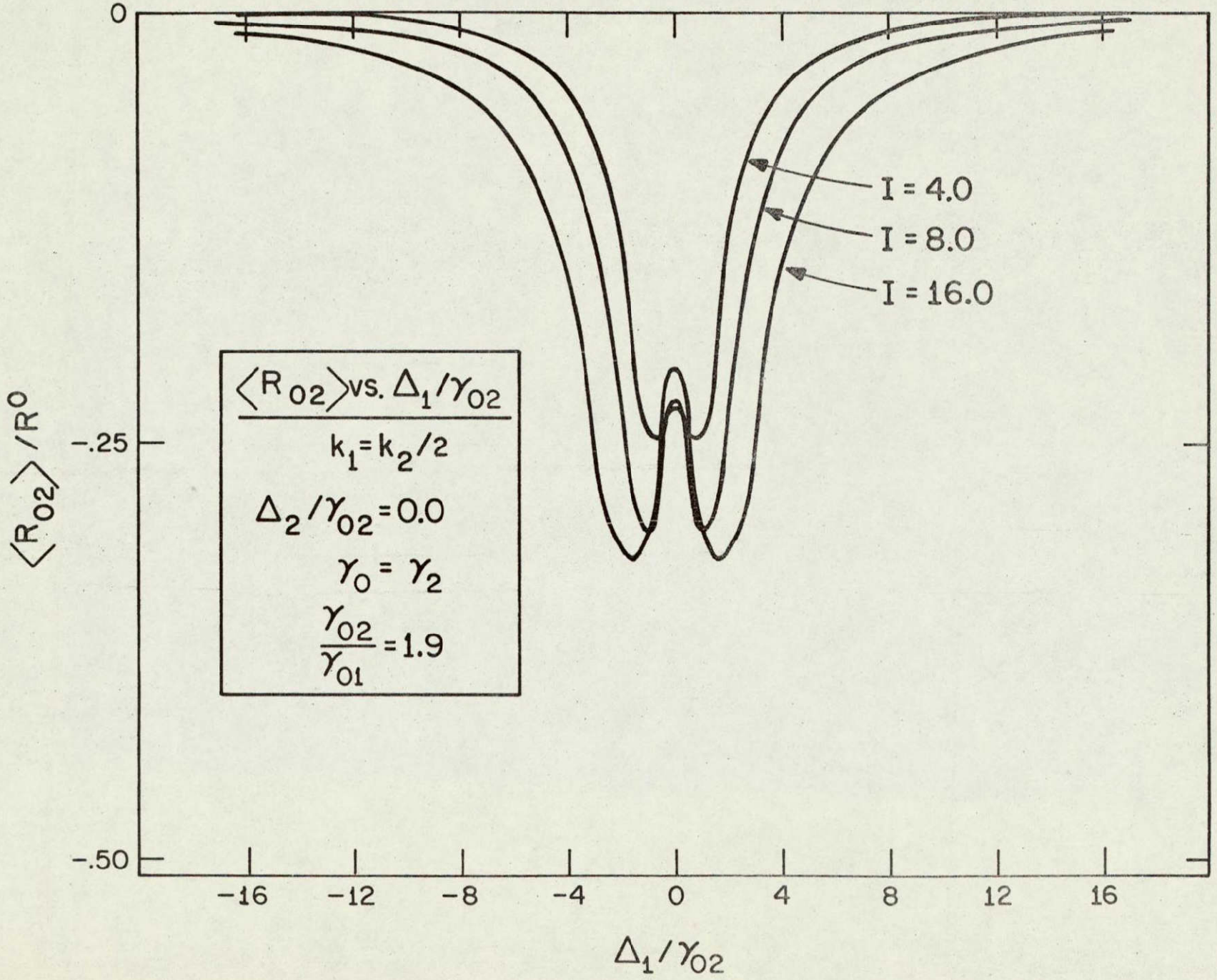
0
-.25
-.50
$\langle R_{02} \rangle / R^0$
I = 4.0
I = 8.0
I = 16.0
$\langle R_{02} \rangle$ vs. Δ_1/γ_{02}
$k_1 = k_2/2$
$\Delta_2/\gamma_{02} = 0.0$
$\gamma_0 = \gamma_2$
$\frac{\gamma_{02}}{\gamma_{01}} = 1.9$
-16
-12
-8
-4
0
4
8
12
16
Δ_1/γ_{02}

Fig. 5c

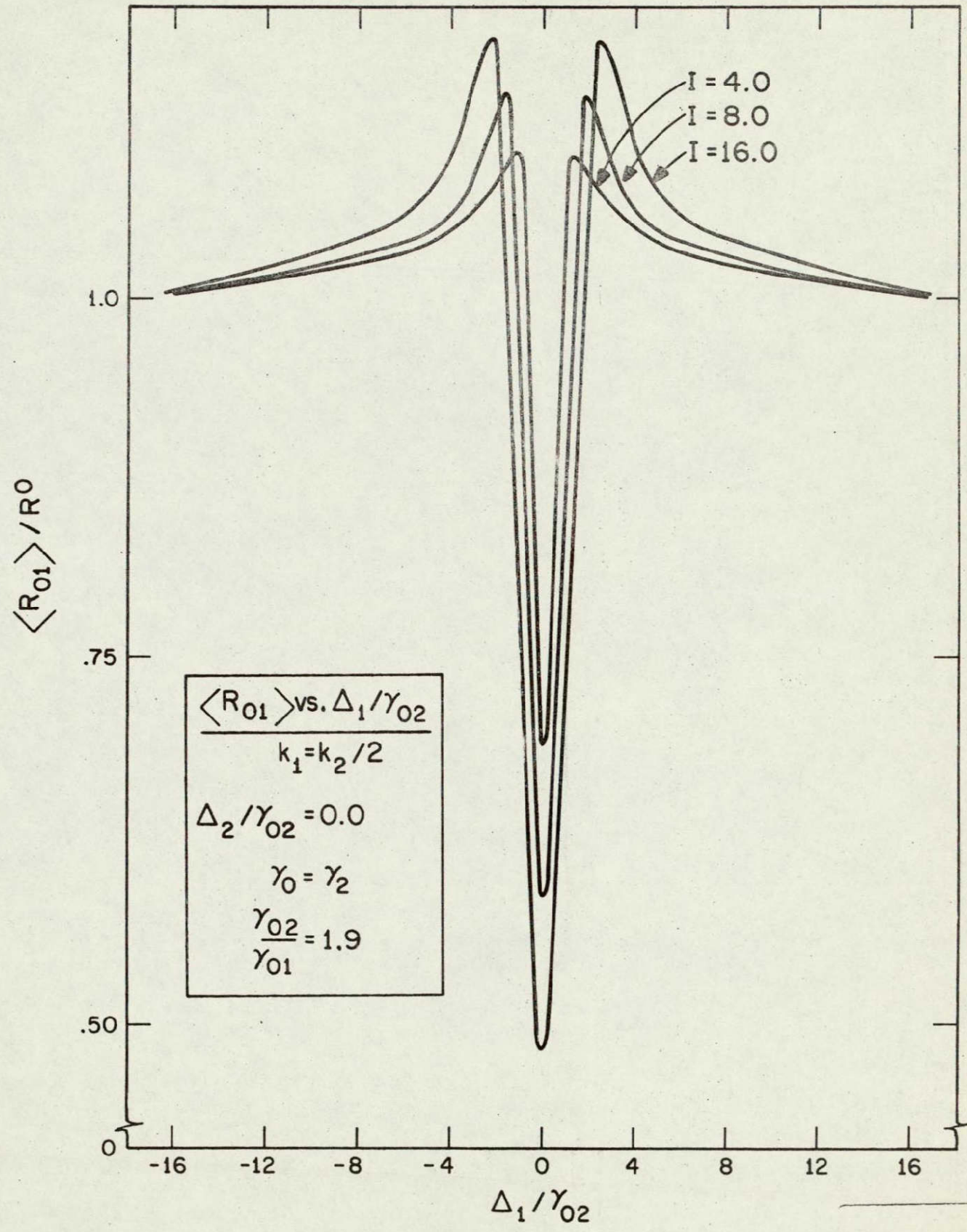
I = 4.0
I = 8.0
I = 16.0
1.0
.75
.50
0
$\langle R_{01} \rangle / R^0$
$\langle R_{01} \rangle$ vs. Δ_1/γ_{02}
$k_1 = k_2/2$
$\Delta_2/\gamma_{02} = 0.0$
$\gamma_0 = \gamma_2$
$\frac{\gamma_{02}}{\gamma_{01}} = 1.9$
-16
-12
-8
-4
0
4
8
12
16
Δ_1/γ_{02}

Fig. 5d

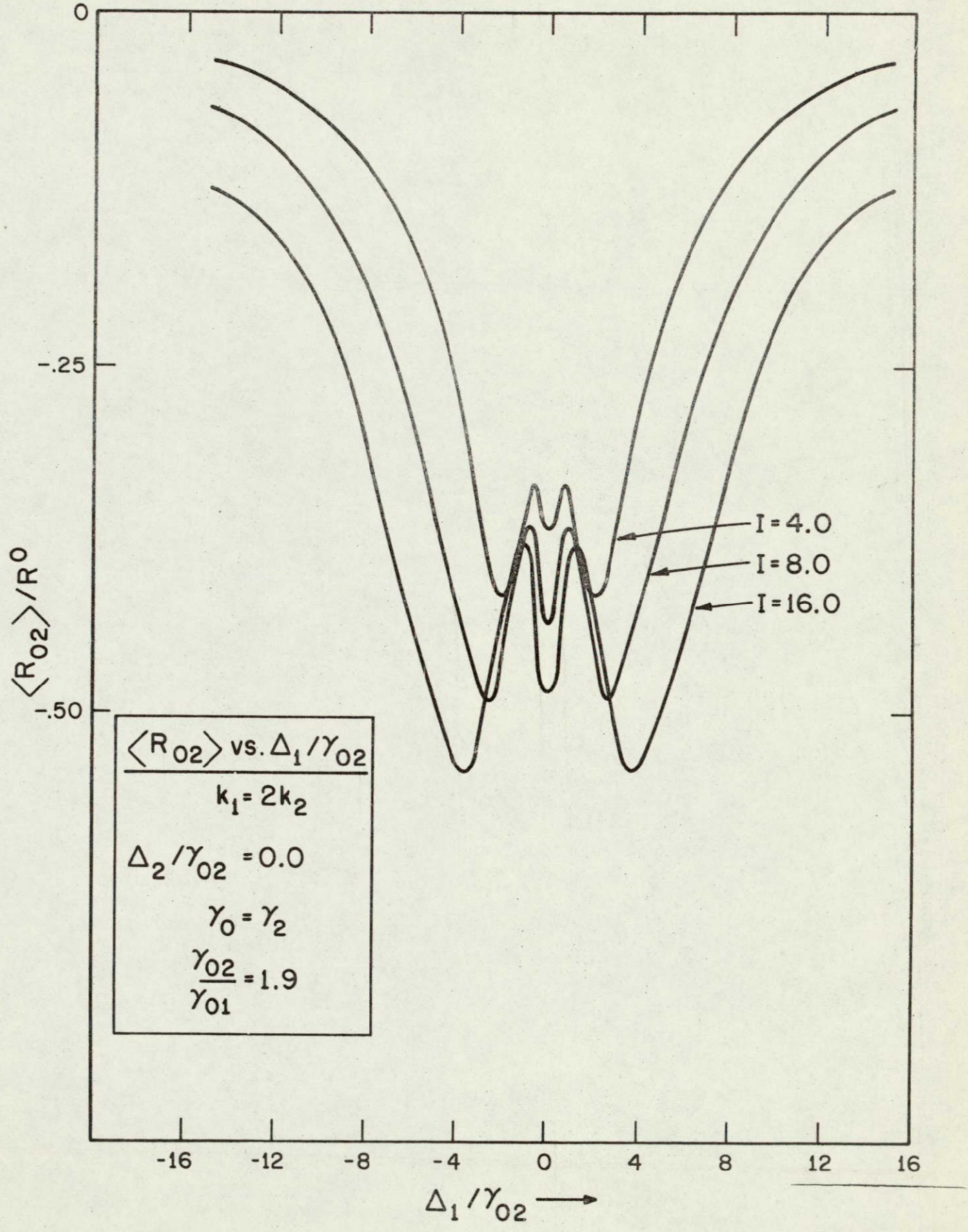
0
-.25
-.50
$\langle R_{02} \rangle / R^0$
I = 4.0
I = 8.0
I = 16.0
$\langle R_{02} \rangle$ vs. Δ_1 / γ_{02}
$k_1 = 2k_2$
$\Delta_2 / \gamma_{02} = 0.0$
$\gamma_0 = \gamma_2$
$\frac{\gamma_{02}}{\gamma_{01}} = 1.9$
-16
-12
-8
-4
0
4
8
12
16
Δ_1 / γ_{02} ⟶

Fig. 5e

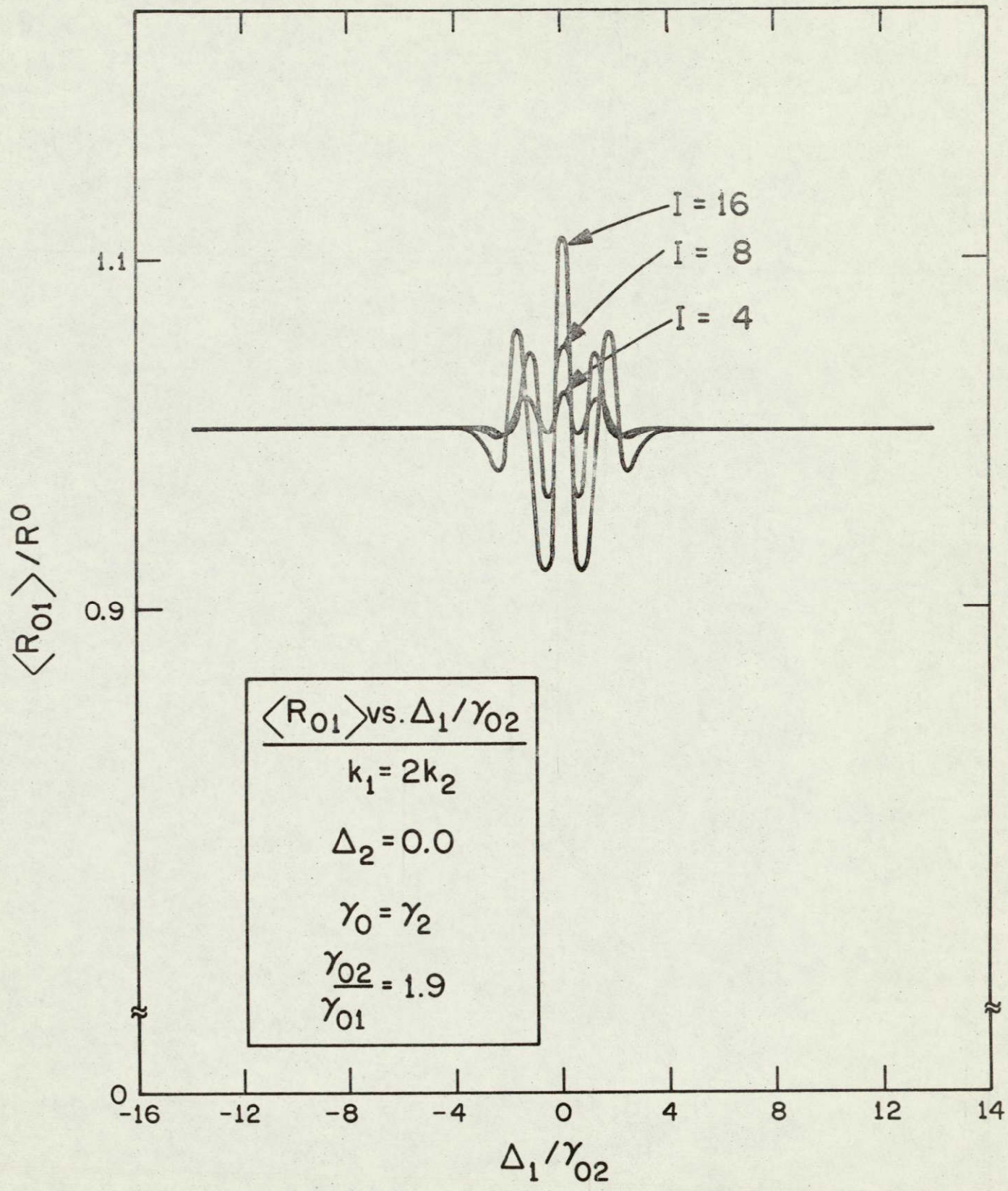
I = 16
I = 8
I = 4
1.1
0.9
0
$\langle R_{01} \rangle / R^0$
$\langle R_{01} \rangle$ vs. Δ_1/γ_{02}
$k_1 = 2k_2$
$\Delta_2 = 0.0$
$\gamma_0 = \gamma_2$
$\frac{\gamma_{02}}{\gamma_{01}} = 1.9$
-16
-12
-8
-4
0
4
8
12
14
Δ_1/γ_{02}

Fig. 5f

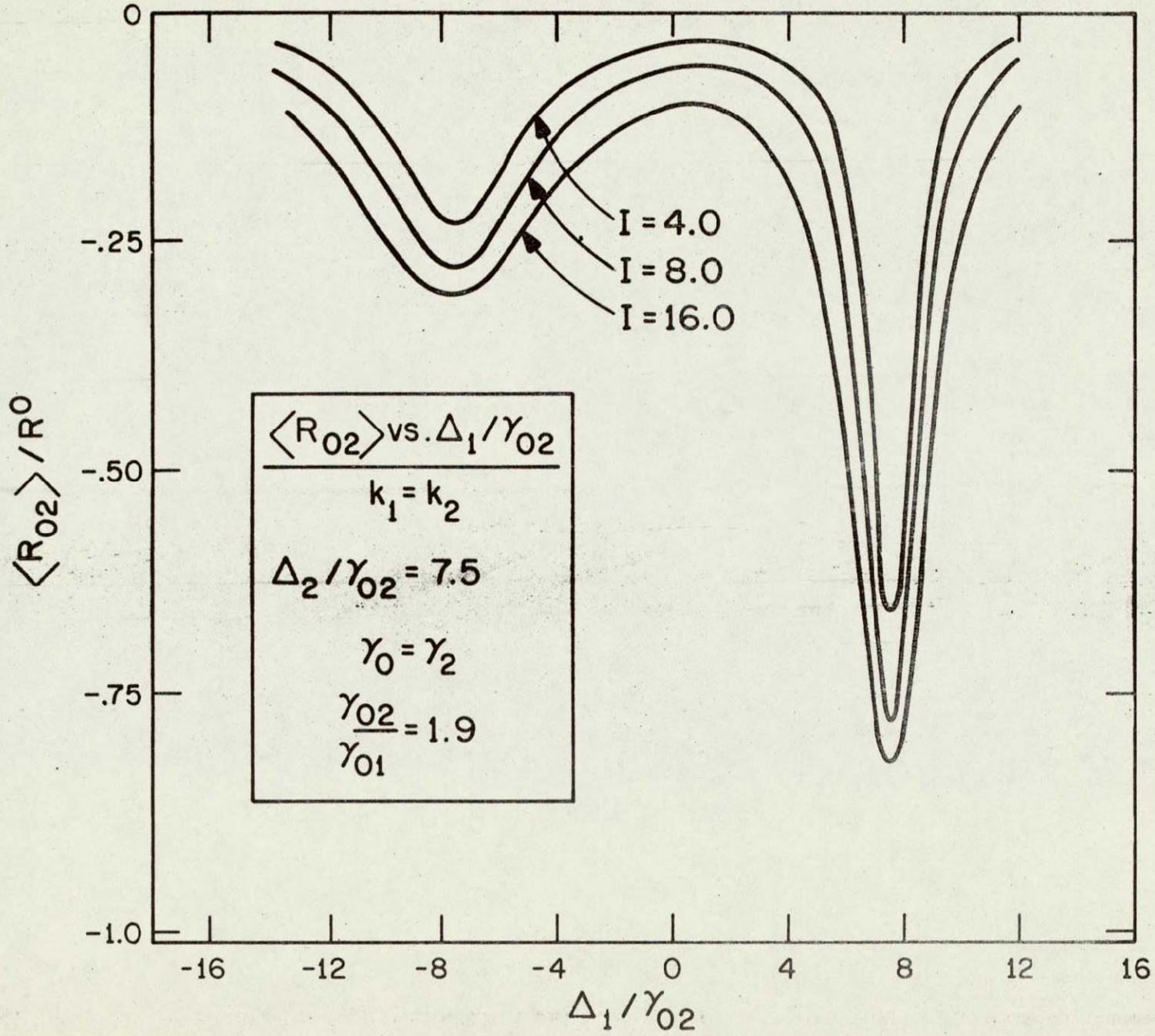
0
-.25
-.50
-.75
-1.0
-16
-12
-8
-4
0
4
8
12
16
$\langle R_{02} \rangle / R^0$
Δ_1 / γ_{02}
I = 4.0
I = 8.0
I = 16.0
$\langle R_{02} \rangle$ vs. Δ_1 / γ_{02}
$k_1 = k_2$
$\Delta_2 / \gamma_{02} = 7.5$
$\gamma_0 = \gamma_2$
$\frac{\gamma_{02}}{\gamma_{01}} = 1.9$

Fig. 6a

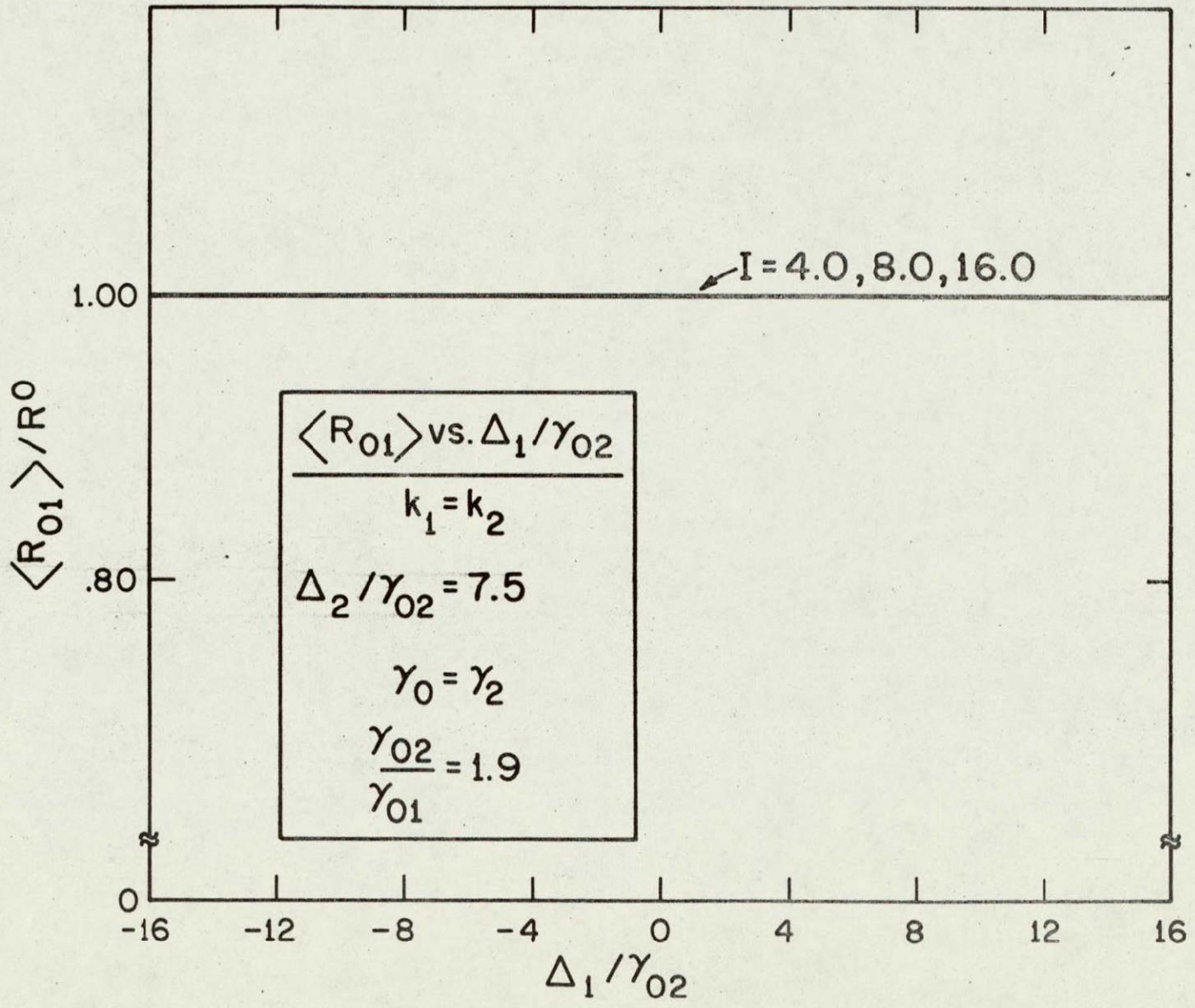
I = 4.0, 8.0, 16.0
1.00
.80
0
$\langle R_{01} \rangle / R^0$
$\langle R_{01} \rangle$ vs. Δ_1/γ_{02}
$k_1 = k_2$
$\Delta_2/\gamma_{02} = 7.5$
$\gamma_0 = \gamma_2$
$\frac{\gamma_{02}}{\gamma_{01}} = 1.9$
-16
-12
-8
-4
0
4
8
12
16
Δ_1/γ_{02}

Fig. 6b

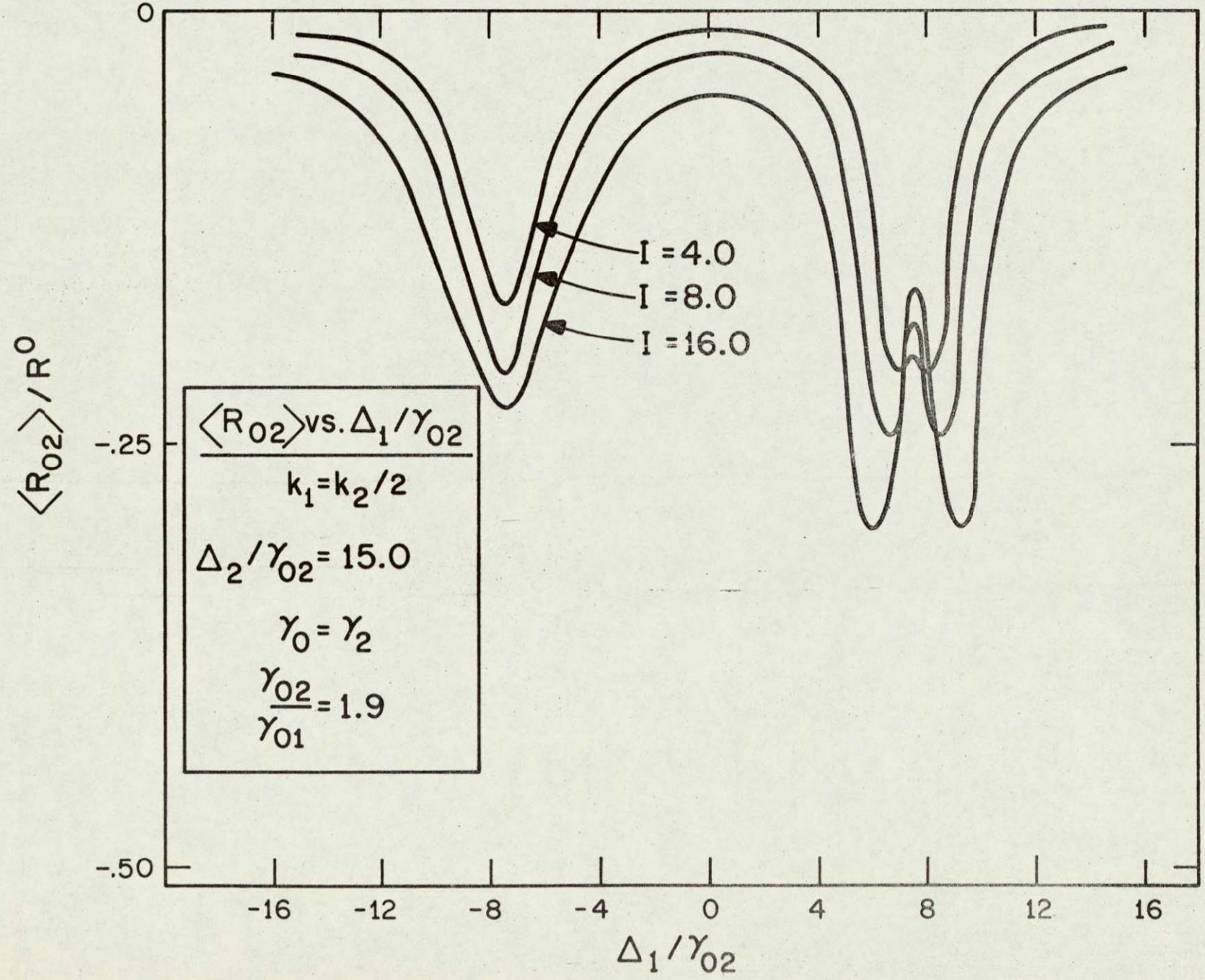
0
-.25
-.50
$\langle R_{02} \rangle / R^0$
I = 4.0
I = 8.0
I = 16.0
$\langle R_{02} \rangle$ vs. Δ_1/γ_{02}
$k_1 = k_2/2$
$\Delta_2/\gamma_{02} = 15.0$
$\gamma_0 = \gamma_2$
$\frac{\gamma_{02}}{\gamma_{01}} = 1.9$
-16
-12
-8
-4
0
4
8
12
16
Δ_1/γ_{02}

Fig. 6c

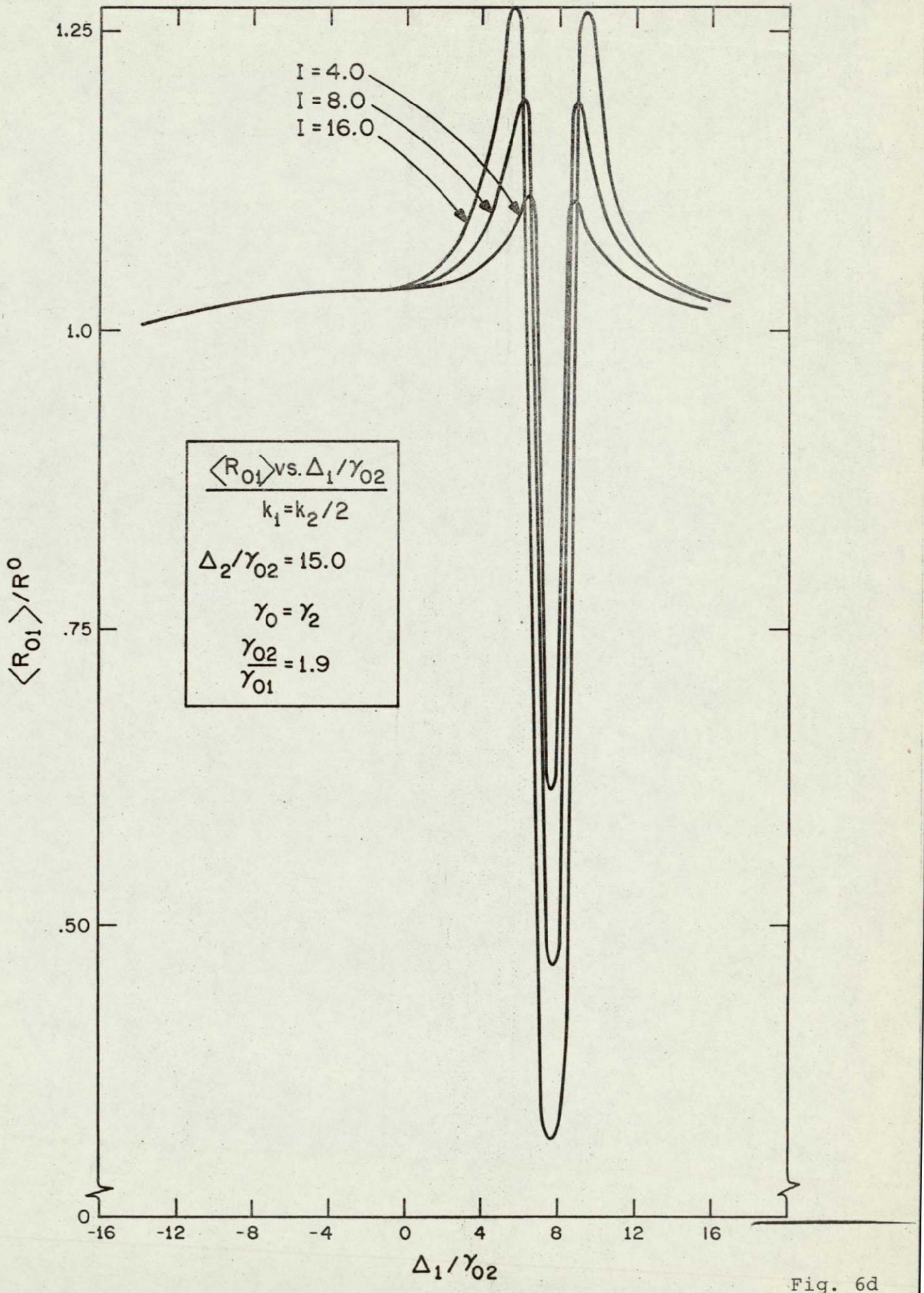
1.25
1.0
.75
.50
0
I = 4.0
I = 8.0
I = 16.0
$\langle R_{01} \rangle$ vs. Δ_1/γ_{02}
$k_1 = k_2/2$
$\Delta_2/\gamma_{02} = 15.0$
$\gamma_0 = \gamma_2$
$\frac{\gamma_{02}}{\gamma_{01}} = 1.9$
$\langle R_{01} \rangle / R^0$
-16
-12
-8
-4
0
4
8
12
16
Δ_1/γ_{02}

Fig. 6d

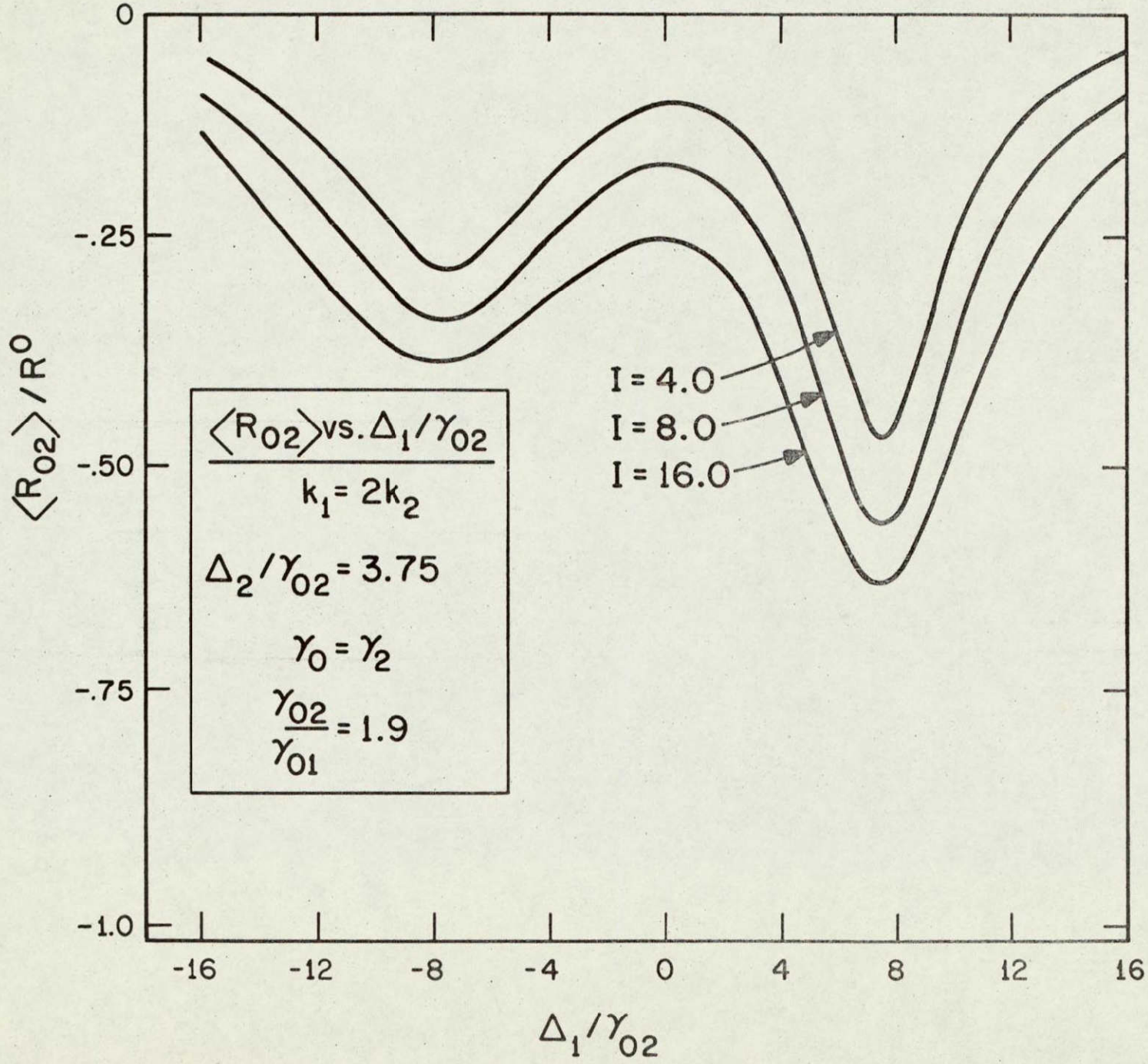
0
-.25
-.50
-.75
-1.0
$\langle R_{02} \rangle / R^0$
-16
-12
-8
-4
0
4
8
12
16
Δ_1 / γ_{02}
$\langle R_{02} \rangle$ vs. Δ_1 / γ_{02}
$k_1 = 2k_2$
$\Delta_2 / \gamma_{02} = 3.75$
$\gamma_0 = \gamma_2$
$\frac{\gamma_{02}}{\gamma_{01}} = 1.9$
I = 4.0
I = 8.0
I = 16.0

Fig. 6e

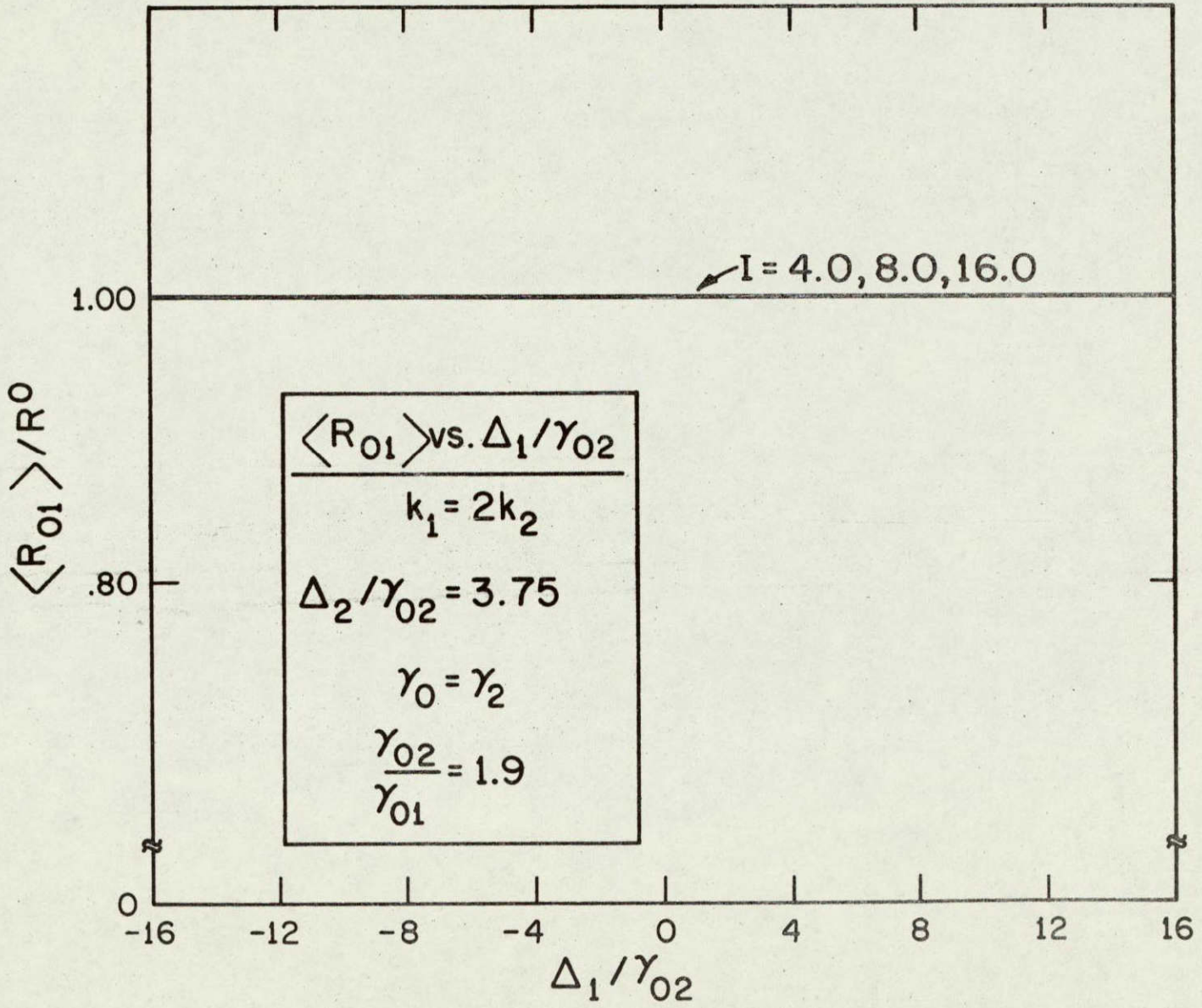
I = 4.0, 8.0, 16.0
1.00
.80
0
$\langle R_{01} \rangle / R^0$
$\langle R_{01} \rangle$ vs. Δ_1/γ_{02}
$k_1 = 2k_2$
$\Delta_2/\gamma_{02} = 3.75$
$\gamma_0 = \gamma_2$
$\frac{\gamma_{02}}{\gamma_{01}} = 1.9$
-16
-12
-8
-4
0
4
8
12
16
Δ_1/γ_{02}

Fig. 6f

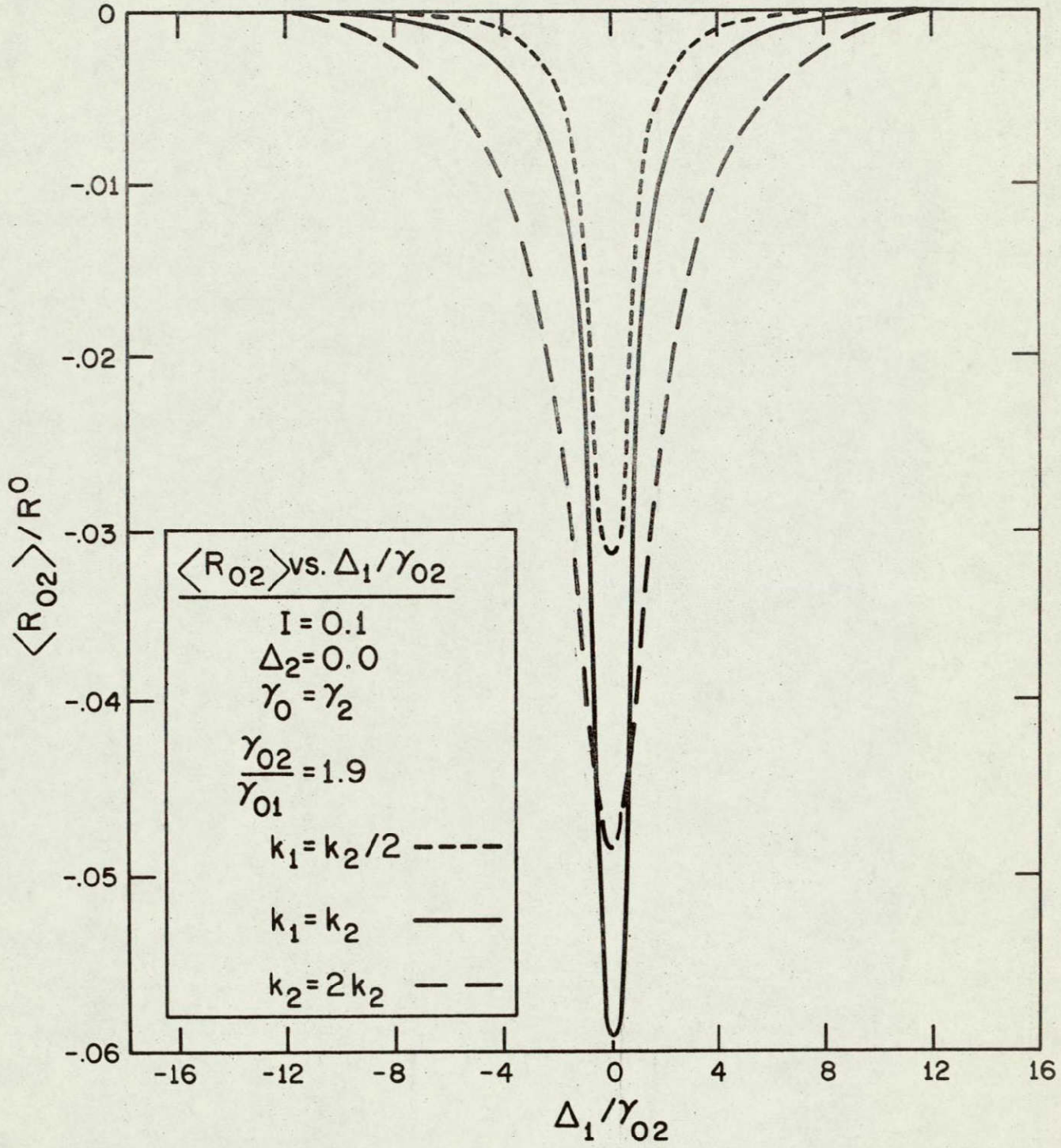
0
-.01
-.02
-.03
-.04
-.05
-.06
-16
-12
-8
-4
0
4
8
12
16
$\langle R_{02} \rangle / R^0$
Δ_1 / γ_{02}
$\langle R_{02} \rangle$ vs. Δ_1 / γ_{02}
I = 0.1
$\Delta_2 = 0.0$
$\gamma_0 = \gamma_2$
$\frac{\gamma_{02}}{\gamma_{01}} = 1.9$
$k_1 = k_2/2$
$k_1 = k_2$
$k_2 = 2k_2$

Fig. 7a

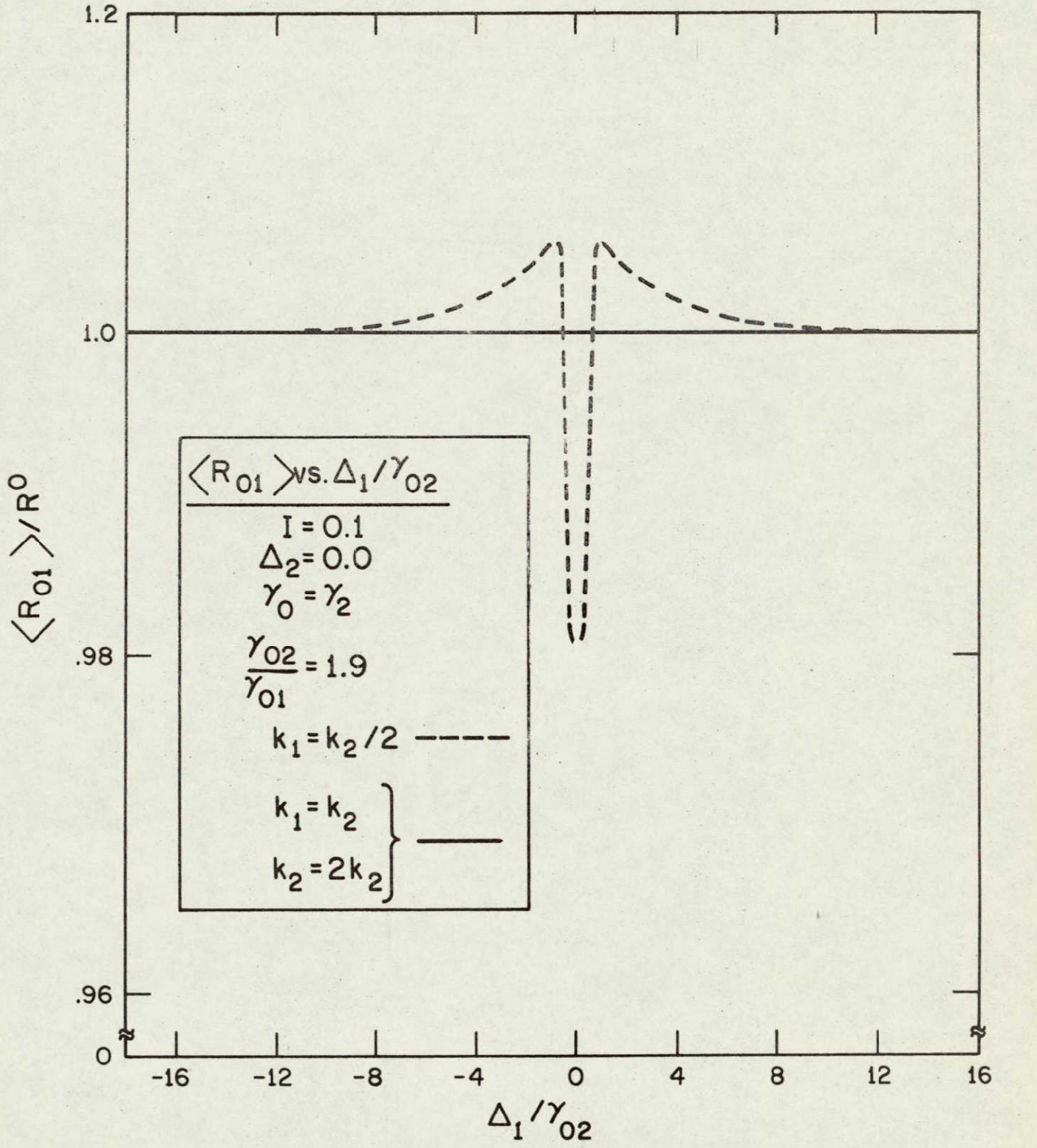
1.2
1.0
.98
.96
0
$\langle R_{01} \rangle / R^0$
$\langle R_{01} \rangle$ vs. Δ_1/γ_{02}
I = 0.1
$\Delta_2 = 0.0$
$\gamma_0 = \gamma_2$
$\frac{\gamma_{02}}{\gamma_{01}} = 1.9$
$k_1 = k_2/2$
$k_1 = k_2$
$k_2 = 2k_2$
-16
-12
-8
-4
0
4
8
12
16
Δ_1/γ_{02}

Fig. 7b

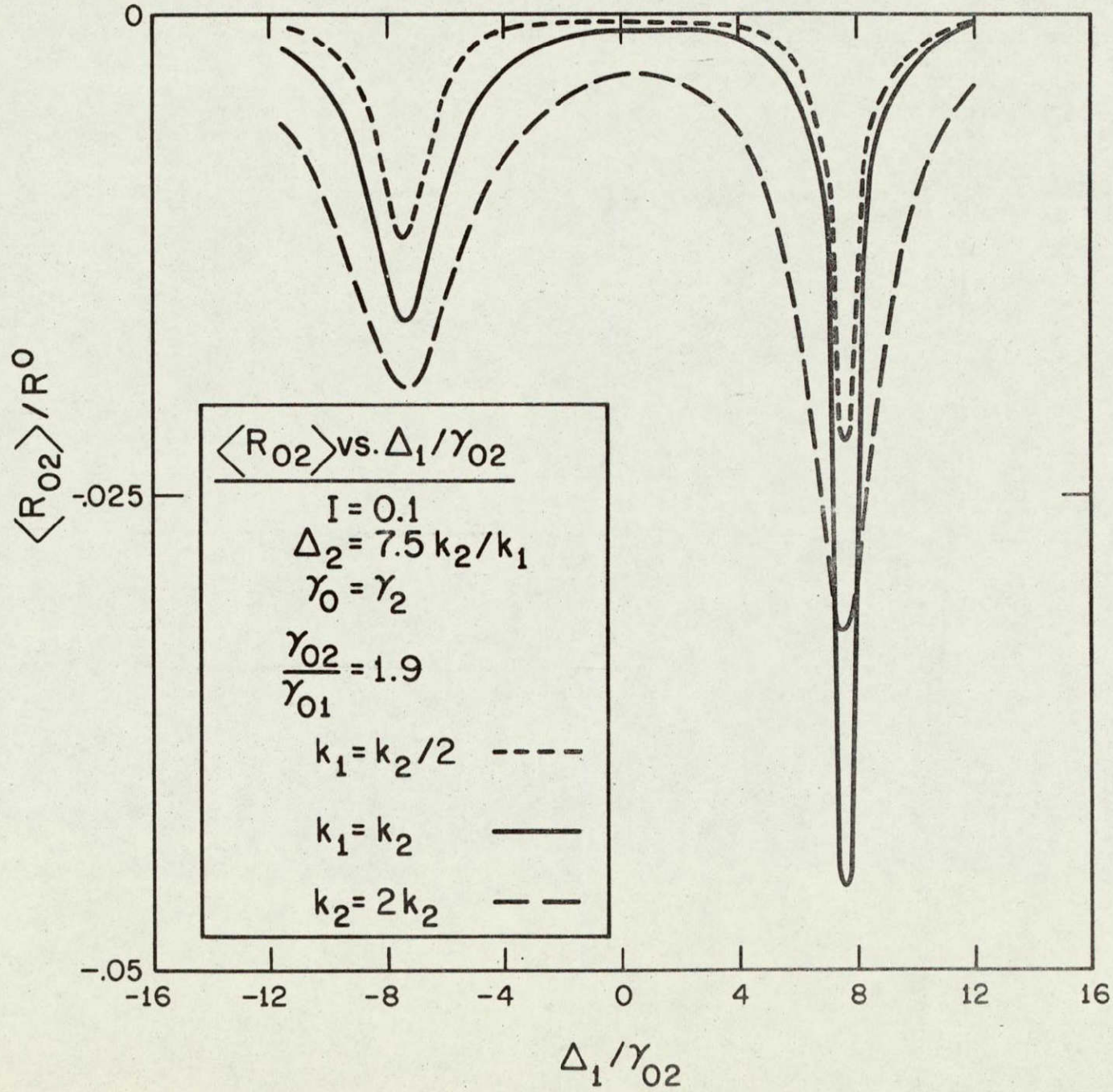
0
-.025
-.05
$\langle R_{02} \rangle / R^0$
-16
-12
-8
-4
0
4
8
12
16
Δ_1 / γ_{02}
$\langle R_{02} \rangle$ vs. Δ_1 / γ_{02}
I = 0.1
$\Delta_2 = 7.5\, k_2 / k_1$
$\gamma_0 = \gamma_2$
$\frac{\gamma_{02}}{\gamma_{01}} = 1.9$
$k_1 = k_2/2$
$k_1 = k_2$
$k_2 = 2k_2$

Fig. 7c

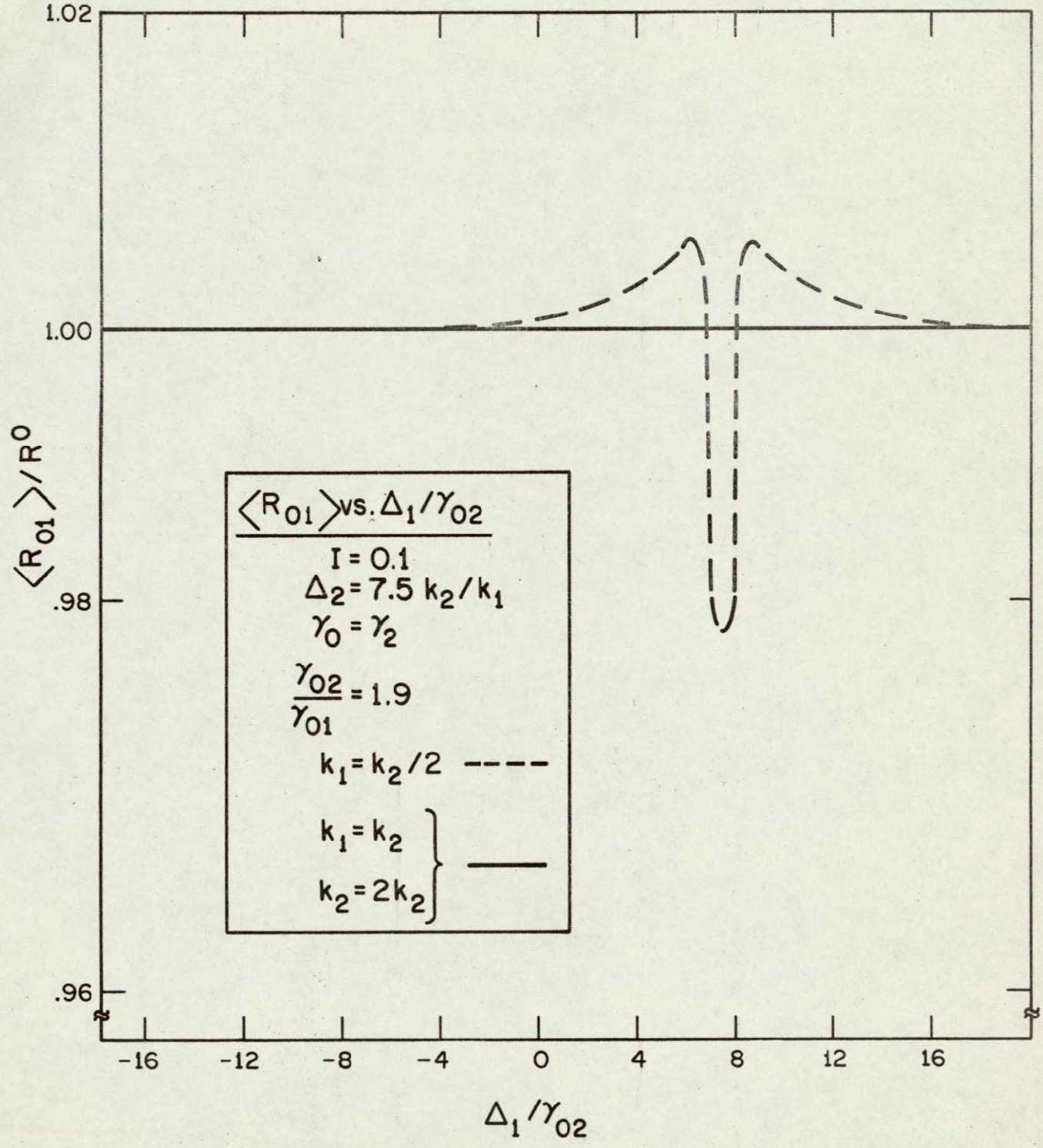
1.02
1.00
.98
.96
$\langle R_{01} \rangle / R^0$
$\langle R_{01} \rangle$ vs. Δ_1/γ_{02}
I = 0.1
$\Delta_2 = 7.5\ k_2/k_1$
$\gamma_0 = \gamma_2$
$\frac{\gamma_{02}}{\gamma_{01}} = 1.9$
$k_1 = k_2/2$
$k_1 = k_2$
$k_2 = 2k_2$
-16
-12
-8
-4
0
4
8
12
16
Δ_1/γ_{02}

Fig. 7d

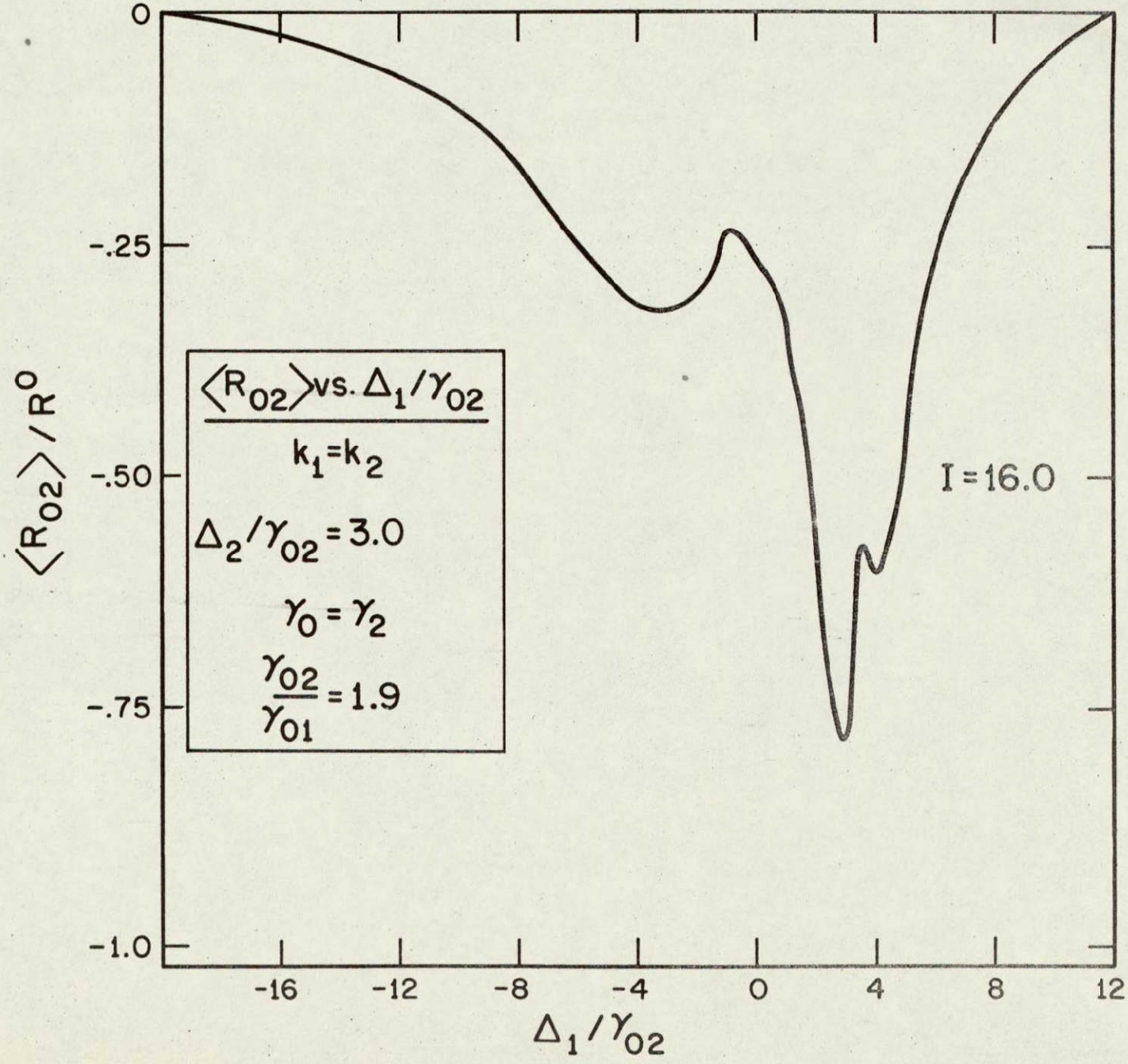
0
-.25
-.50
-.75
-1.0
$\langle R_{02} \rangle / R^0$
$\langle R_{02} \rangle$ vs. Δ_1/γ_{02}
$k_1 = k_2$
$\Delta_2/\gamma_{02} = 3.0$
$\gamma_0 = \gamma_2$
$\frac{\gamma_{02}}{\gamma_{01}} = 1.9$
I = 16.0
-16
-12
-8
-4
0
4
8
12
Δ_1/γ_{02}

Fig. 8a

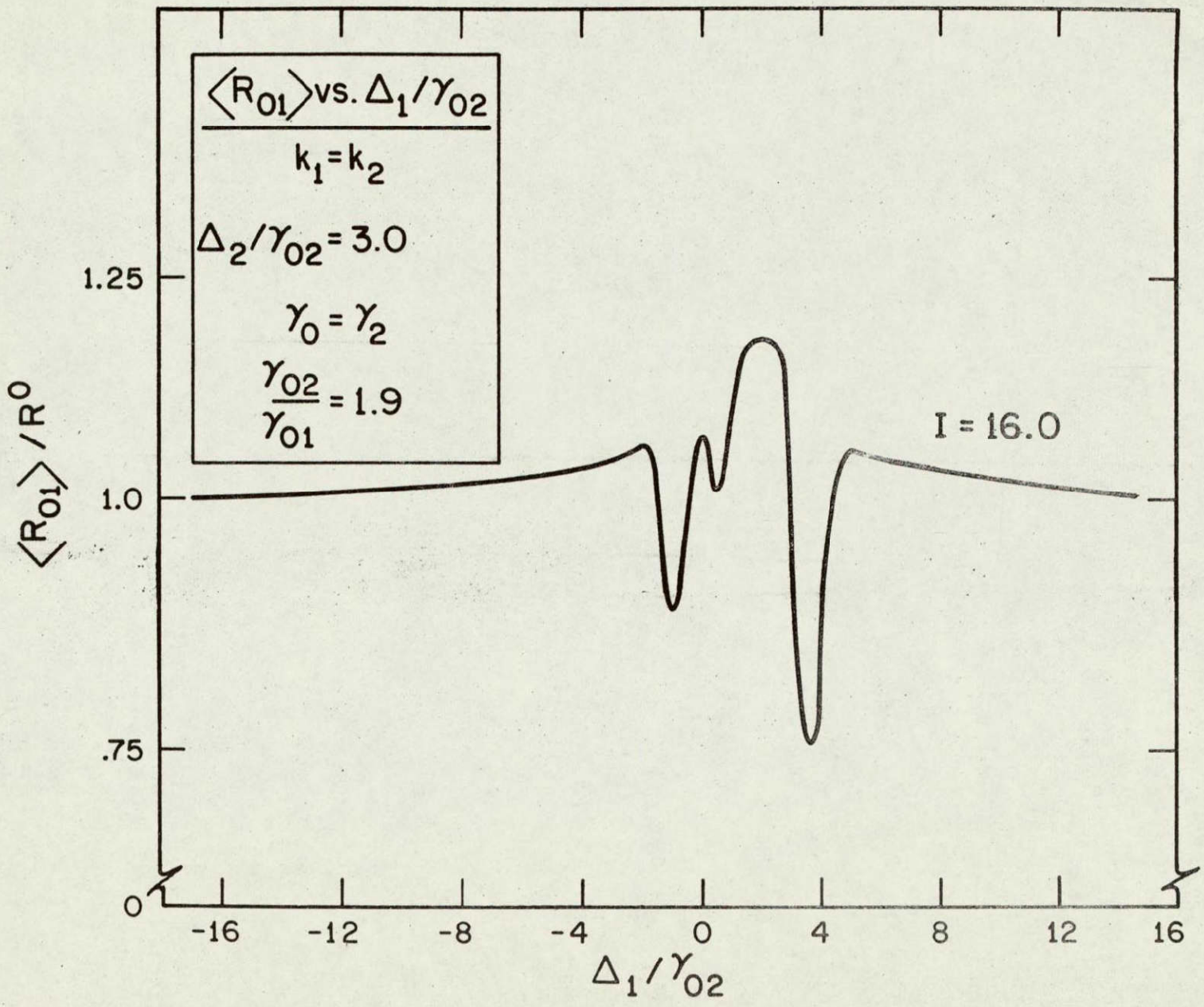
$\langle R_{01} \rangle$ vs. Δ_1/γ_{02}
$k_1 = k_2$
$\Delta_2/\gamma_{02} = 3.0$
$\gamma_0 = \gamma_2$
$\frac{\gamma_{02}}{\gamma_{01}} = 1.9$
I = 16.0
$\langle R_{01} \rangle / R^0$
1.25
1.0
.75
0
-16
-12
-8
-4
0
4
8
12
16
Δ_1/γ_{02}

Fig. 8b

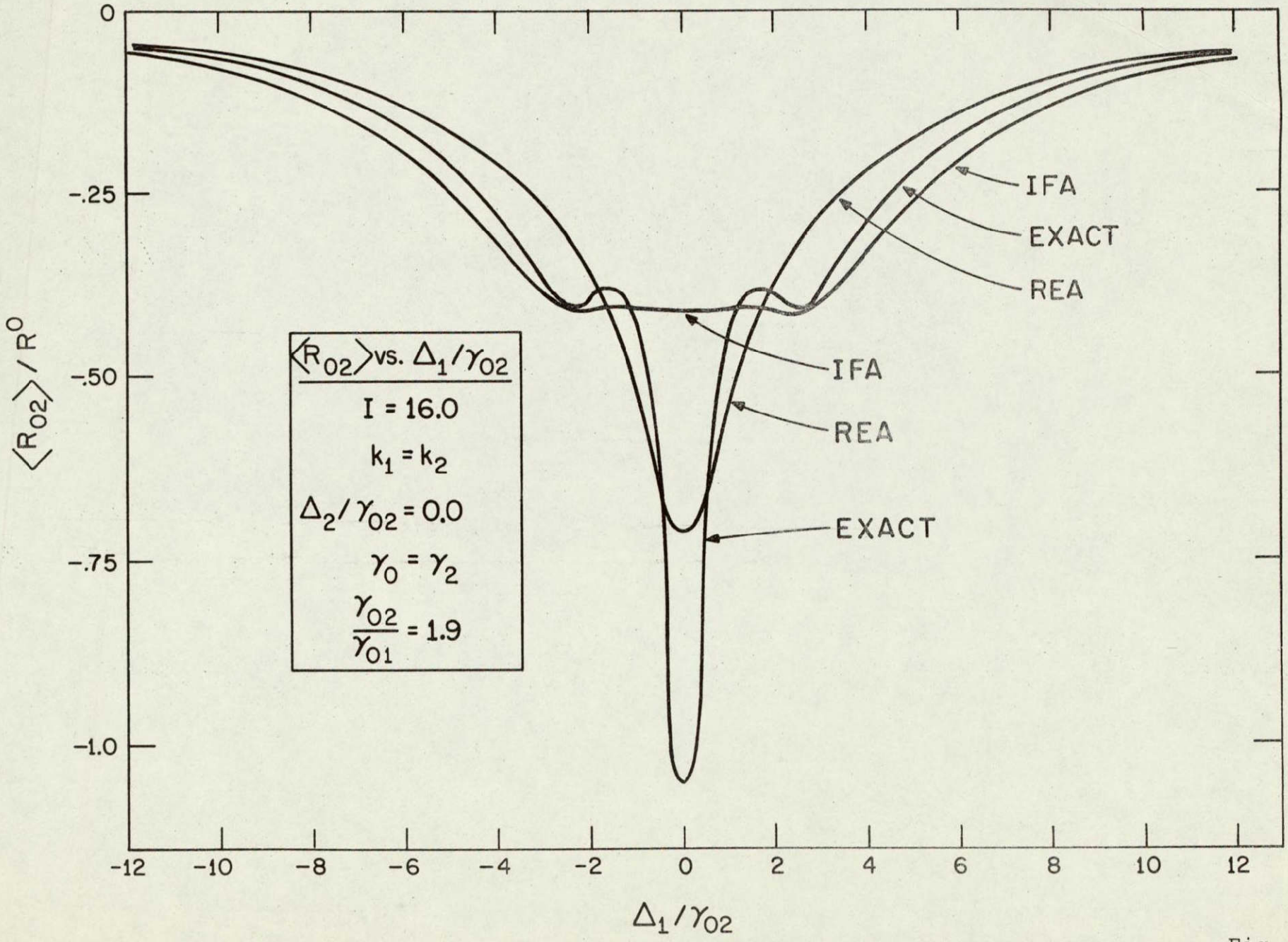
0
-.25
-.50
-.75
-1.0
$\langle R_{02} \rangle / R^0$
-12
-10
-8
-6
-4
-2
0
2
4
6
8
10
12
Δ_1 / γ_{02}
IFA
EXACT
REA
IFA
REA
EXACT
$\langle R_{02} \rangle$ vs. Δ_1 / γ_{02}
I = 16.0
$k_1 = k_2$
$\Delta_2 / \gamma_{02} = 0.0$
$\gamma_0 = \gamma_2$
$\frac{\gamma_{02}}{\gamma_{01}} = 1.9$

Fig. 9